Study of biaxial stress effect on electronic properties at the 4H-SiC-MOS interface

Wei Fu

February 2020

Study of biaxial stress effect on electronic properties at the 4H-SiC-MOS interface

Wei Fu

Doctoral Program in Applied Physics

Submitted to the Graduate School of

Pure and Applied Sciences

in Partial Fulfillment of the Requirements

for the Degree of Doctor of Philosophy in

Engineering

at the

University of Tsukuba

Abstract

Silicon carbide (SiC) has been considered as a promising power device material due to its excellent physical and electrical characteristics. These characteristics include wide bandgap, high breakdown field, high saturation carrier velocity, and high thermal conductivity. These material characteristics have made SiC metal-oxide-semiconductor field-effect transistors (MOSFETs) to be regarded as candidates for high-voltage, high-temperature, and high-speed power switches. However, due to the abnormally high interface state density in the SiO_2/SiC systems, the channel mobility of SiC-MOSFETs is low. So far, researchers have identified some of the reasons that lead to the low electron mobility, for example, Si dangling bonds, residual C clusters, and oxygen vacancy at the interface. For these defects, the post-oxidation annealing (POA) methods, such as a nitridation by NO or N_2O gases, annealing in H_2 or $POCl_3$ ambient, have been applied to improve the electron mobility of the inversion layer, but the field-effect mobility remains as low as 40-80 $cm^2 V^{-1} s^{-1}$. Recently, first-principles calculation studies have suggested that oxidation induced compressive strain results in an interface state formation due to the local change of conduction band energy. Furthermore, the interfacial stress on the SiO_2 oxide film side was evaluated by Li et al., and the strain-induced modulation of the bandgap was theoretically studied by Kenta et al. However, the understanding of the relationship between interfacial stress and electron mobility is still lacked to date.

This thesis focused on the study of the relationship between the biaxial stress induced by thermal oxidation and the electron mobility at the interface of SiO_2/4H-SiC MOS structure. The strain, resulting in the formation of stress, could be considered as one of the origins of the low inversion layer electron mobility since the strain-induced lattice distortion may affect the electron mobility in two possible ways: generating a deformation potential or forming interface defects.

First, using confocal Raman microscopy, we investigated the stress at the SiO_2/4H-SiC interface. The measurement data were collected while the SiO_2 film was sequentially etched on 4H-SiC. A shift of the folded transverse optical E_2 mode peak toward low wavenumbers was observed in a 50 nm thick SiO_2/4H-SiC, and this shift remained constant for samples with a SiO_2 thickness greater than 10 nm. This implies that stress was generated at the interface of SiO_2/4H-SiC and accumulated in the SiO_2 region during the thermal oxidation process. Based on the above interface stress evaluation method, we studied the effect of annealing in NO on stress generation, while the calculated stresses showed similar values. Therefore, we conclude the NO post-annealing does not drastically affect stress relaxation at the SiO_2/4H-SiC interface.

Next, to confirm how to interface stress affects the electron mobility, we evaluated the relationship between the biaxial stress and the electron transport properties at SiO_2/4H-SiC interfaces using a theoretical calculation. The low-field three-dimensional and two-dimensional electron mobility of 4H-SiC in the temperature range of 100-600 K is calculated based on the acoustic and intervalley optical phonon scattering models. Compared with acoustic scattering, intervalley optical scattering is the main factor that affects electron transport performance. When the 4H-SiC with strain $< 0.5\%$, the strain basically does not affect the phonon-limited electron mobility. For the 4H-SiC with strain $> 0.5\%$, the strain significantly reduces the electron mobility. Since the actual strain value at the thermal oxidized SiO_2/SiC interface is only around 0.1-0.15%, this may indicate that the lattice distortion induced an effective mass change in-plane is too small to affect electron transport properties at the SiO_2/SiC interface.

Finally, as mentioned before, the interface stress-induced lattice distortion may affect the electron mobility in 1)

generation of the deformation potential; 2) formation of the interface defects. Based on our calculation result, we have found that the high-temperature thermal oxidation induced interface stress has so little effect on the effective mass that does not affect the electron mobility. Therefore, we can consider that the interface stress-induced lattice distortion may mainly affect the electron mobility by the formation of interface defects. To suppress the generation of interface stress, it is necessary to develop a low-temperature oxidation method for fabrication of the MOS structures, the Nitric Acid Oxidation of SiC (NAOS) was employed to fabricate the SiC/SiO_2 structure. An atomic layer deposition (ALD) Al_2O_3 layer was deposited on the NAOS layer to form a double oxide layer to improve the electrical properties of the SiC-MOS structure further. In the case of the $<Al_2O_3/NAOS/Si>$ MOS structure, the critical finding is that an annealing treatment is essential for the NAOS layer to improve its quality to reduce the inter-diffusion in the MOS structure. In the case of the $<Al_2O_3/NAOS/SiC>$ MOS structure, the $NAOS/Al_2O_3$ combination layer offered a surface passivation effect on SiC, and the annealing temperature can control the passivation effect. Thus, we speculate that the $NAOS/Al_2O_3$ layer not only can reduce the defects which can be passivated by NO POA, and also can avoid the defects induced by interface stress.

Table of contents

Chapter 1 Introduction

Improving energy efficiency is one of the diverse solutions to social problems. Semiconductor power devices are critical equipment to improve energy efficiency, help to realize a recycling-oriented society, make full use of limited energy, and improve the effectiveness of the power supply system.

1.1 Application Background of Semiconductor Power devices

Modern society is increasingly relying on the convenience provided by electricity, transportation, and healthcare, which has driven tremendous advances in power generation, distribution, and power management technologies. The power semiconductor device, which used as switches or rectifiers in power electronic circuits, is a semiconductor element for controlling, converting, and supplying power. It is widely used for industrial equipment applications such as automobiles and railways, renewable energy applications, and consumer equipment applications such as air conditioners and refrigerators. In Figure 1.1.1, The application of power equipment is shown as a function of operating frequency. Currently, most of these applications are served by silicon devices.

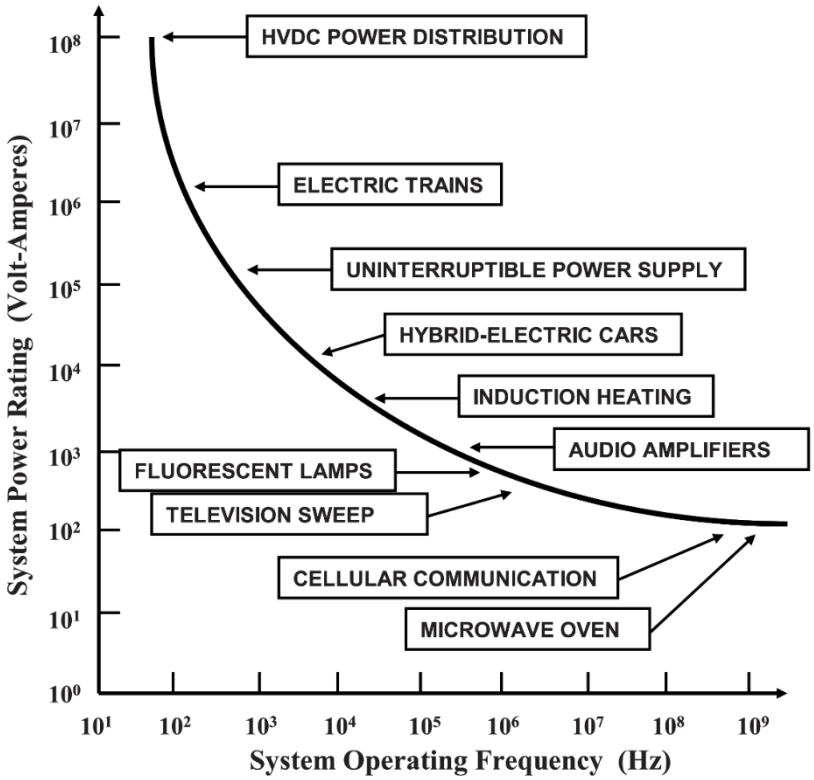

Figure 1.1.1 Application for power devices[1].

Semiconductor power devices are the heart of power electronics and are used to convert and control power. From an energy perspective, control power controls the relationship between input and output. Four primary methods of power conversion: (1) Converter (AC-DC); (2) Frequency conversion (AC-AC); (3) DC Regulator (DC-DC); (4) Inverter (DC-

AC) (Figure 1.1.2). For power devices that perform various power conversions in this way, the energy loss associated with power conversion be as small as possible, and conversion with 100% efficiency should be ideal. That is, ideally, the leakage current when the switch is off is zero, the voltage drops when the switch is on is zero, and the switching time is zero. This improvement in conversion efficiency is the biggest goal of technological and material development.

Power semiconductor devices can be divided into unipolar, bipolar, and composite devices according to their carrier conductivity. Among them, the thyristor is a semi-controlled device, which has the highest voltage and current capacity

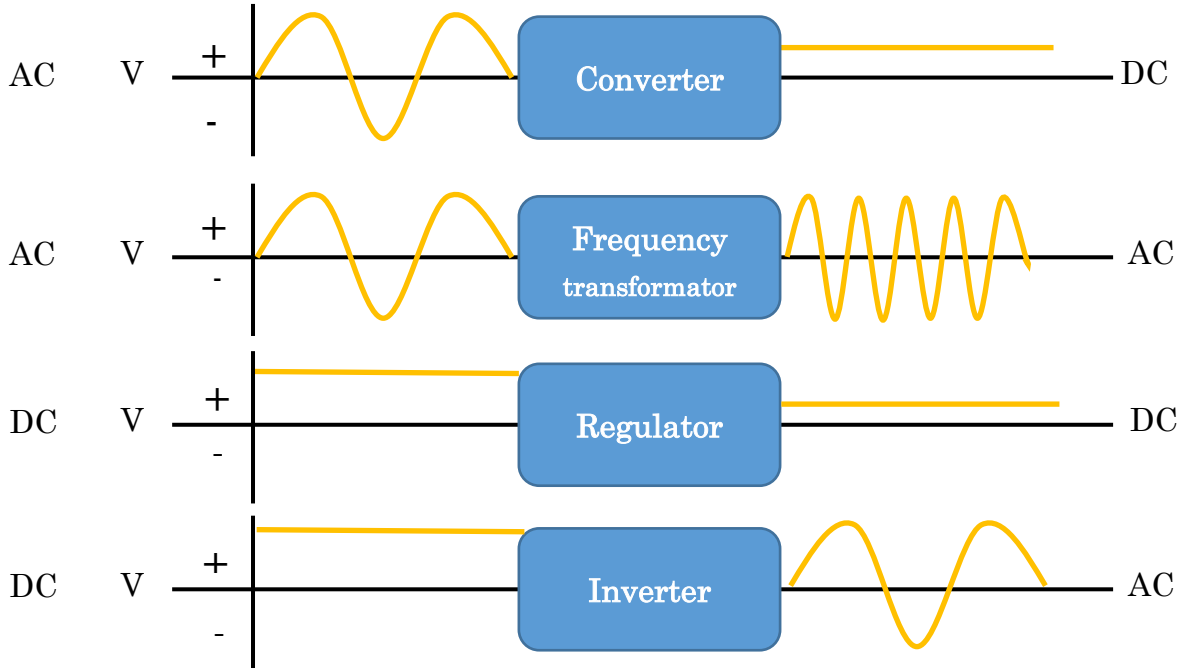

Figure 1.1.2 Classification of power converters

among all devices. The power diode is an uncontrollable device with simple structure and principle and reliable operation. It can also be divided into voltage-driven devices and current-driven devices, including GTO (gate turn-off thyristor). GTO is a current-driven device, IGBT (insulated gate bipolar transistors), and power MOSFET (metal-oxide-semiconductor field-effect transistor) are voltage-driven devices. Different power semiconductor devices have different characteristics, such as withstand voltage, current capacity, impedance capability, and size. In actual use, it is necessary to select appropriate accessories according to different fields and different needs. The classification and application fields of power semiconductor devices are shown in Table 1.1.

However, using currently available technologies, the efficiency of power conversion is usually 95-97%, which is not high enough, because, at each power conversion, about 3-5 % of the electrical energy lost due to heat. In ubiquitous AC-DC and DC-AC conversions, the efficiency is as low as about $(0.95)^2 \approx 0.9$. The field of power electronics is so large that, on average, 12 billion kilowatt-hours of electrical energy is converted, processed, or recovered by specific power electronic equipment every day, which is more than 80% of the power generation. Due to the low power conversion efficiency, the energy loss during power conversion is very high. Therefore, it is necessary to improve the efficiency of a wide range of energy systems such as power generation, transmission/transformation, and distribution. At present, Si is the most commonly used semiconductor material for power devices in society. Through the development of power MOSFETs and IGBTs, the performance of silicon power switching devices has been significantly improved. However, due to the limitation of the physical properties of silicon materials, silicon power devices cannot adequately meet market

demands. Therefore, due to the excellent physical properties of wide-bandgap semiconductor materials, attention has been focused on wide-bandgap semiconductor materials.

Table 1.1 Comparison of Power semiconductor devices[1, 2]

	Typical Device	Advantages	Shortage	Application
Bipolar devices	Diode	Simple structure and High reliability	The circuit is complex and cannot be applied to high frequencies	Industrial and power systems
	Thyristor	Withstand high voltage and current	Switching speed is lower than MOSFET, voltage and current are less than GTO	
	GTO	Large voltage and Current capacity	Only suitable for power electronic devices with power less than 10kW	Computer, Communication, Consumer electronics, Cartronics
Unipolar devices	MOSFET	Fast switching speed, High input impedance, Good thermal stability, Small driving power, Simple driving circuit, High operating flatness, No secondary breakdown problem	Low current capacity and low withstand voltage, Generally only suitable for electrical and electronic devices with power less than 10kW	
Composite devices	IGBT, IGCT	Fast switching speed and low loss, Withstand pulse current, Small input impedance, Low driving power	The driving circuit is complicated, Problem with a secondary breakdown	

1.2 Physical properties of Silicon Carbide (SiC)

1.2.1 Crystal structure and Electrical properties

Silicon carbide (SiC) is an IV-IV compound semiconductor with a bandgap of around 3.26 eV. The electronic structure of neutral Si and C atoms in their ground states are:

$$\text{Si}, 14e^-: 1s^2 2s^2 2p^6 3s^2 3p^2$$

$$\text{C}, 6e^-: 1s^2 2s^2 2p^2$$

Si and C atoms are both tetravalent elements and have four valence electrons in their outermost shells. By sharing the electron pairs in the sp^3-hybridized orbits, Si and C atoms are combined with covalently bonded tetrahedrons to form SiC crystals. There are precisely four C atoms next to each Si atom and vice versa. The Si-C bond energy is very high (4.6 eV), which gives SiC various excellent properties such as very high hardness and chemical inertness. From a crystallographic perspective, different stacking sequences of the double-atomic (Si and C) layers, will cause SiC to have different crystal structures. The structures of popular 3C-SiC, 4H-SiC, and 6H-SiC are shown schematically in Figure 1.2.1. Here, A, B, and C are sites that may be occupied by the hexagonal close-packed structure[3].

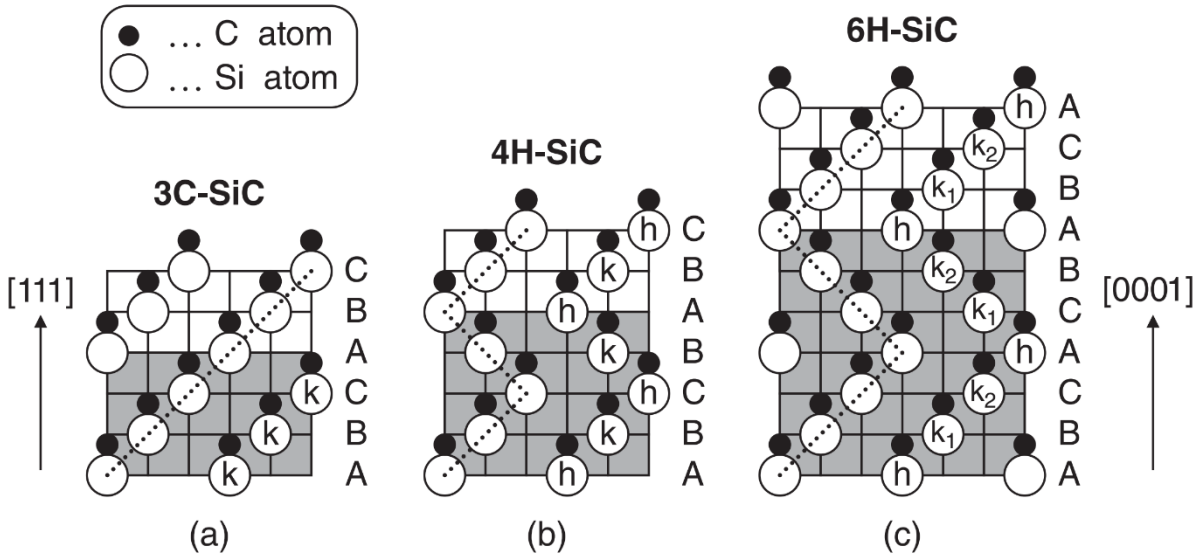

Figure 1.2.1 Schematic structure of general SiC polytype; (a) 3C-SiC, (b) 4H-SiC, and (c) 6H-SiC.[3]

Figure 1.2.2 shows the primitive cells and major translation vectors of cubic SiC and hexagonal SiC. Among the various crystal structures of SiC, single-crystal 4H-SiC has the highest electron mobility, and the mobility is nearly isotropic in directions parallel to and perpendicular to the crystallographic c-axis. Therefore, 4H-SiC is the first choice for manufacturing silicon carbide high-power devices, including prototype power metal-oxide-semiconductor field-effect transistors. Therefore, only 4H-SiC was selected as the research object in this study. The primitive cells and fundamental translation vectors of (a) cubic SiC and (b) hexagonal SiC is shown in Figure 1.2.2. The axial thermal expansion coefficient of hexagonal (4H) polytype of SiC perpendicular (α_{11}) and parallel (α_{33}) to the c-axis have been measured. The second-order polynomials express axial coefficients of the thermal expansion[4]:

$$\alpha_{11} = 3.21 \times 10^{-6} + 3.56 \times 10^{-9} T - 1.62 \times 10^{-12} T^2,$$

And

$$\alpha_{33} = 3.09 \times 10^{-6} + 2.63 \times 10^{-9}T - 1.08 \times 10^{-12}T^2(℃^{-1})$$

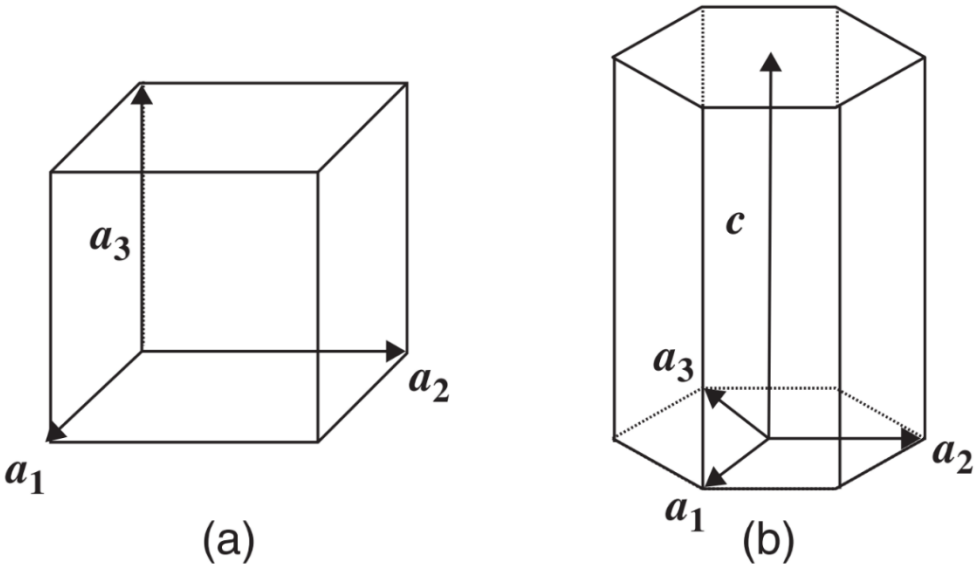

Figure 1.2.2 Primitive cells and fundamental translation vectors of (a) cubic SiC and (b) hexagonal SiC.[4]

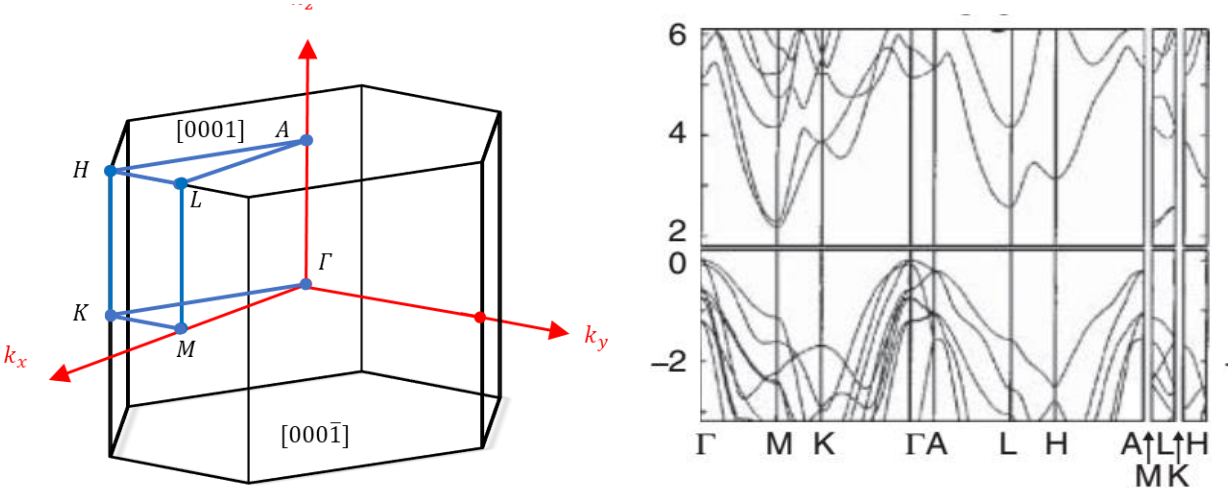

Figure 1.2.3 (a) First Brillouin zone of 4H-SiC and (b) electronic band structure [6]

Figure 1.2.3 shows the first Brillouin zone[5] and the electronic band structure of a 4H-SiC polytype [6]. 4H-SiC has an indirect energy band structure. The top of the valence band and the bottom of the conduction band are located at points Γ and M of the Brillouin zone, respectively. The number of conduction band minima in the first Brillouin zone is 3 for 4H-SiC.

1.2.2 Thermal properties in 4H-SiC for Raman selection rule

Figure 1.2.4 (lift) shows the phonon dispersion relationship for 4H-SiC[7, 8]. The main branches include TA (transverse acoustic), LA (longitudinal acoustic), TO (transverse optical), and LO (longitudinal optical) phonons. The leading phonon

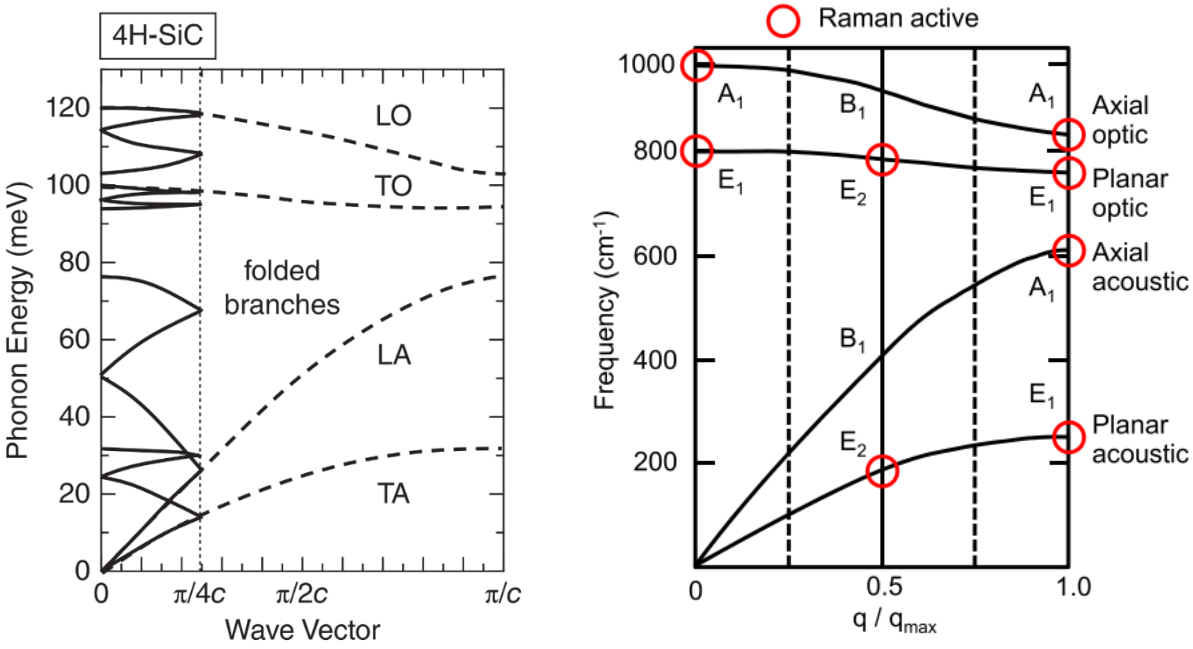

Figure 1.2.4 Schematic phonon dispersion relationship for 4H-SiC. The red open circles show the Raman active modes. The symmetries of the phonons are valid only for phonons propagating along the c axis.

energy (or wavenumber) can be directly observed by Raman scattering spectroscopy. We can see that near the wave vector is zero, the relationship between acoustic phonon energy and wave vector is basically linear, while optical phonons have no dispersion. The principal phonon energies (or wavenumber) can be directly observed by Raman scattering spectroscopy. The 4H-SiC polytype belongs to the C_{6v}^{c} space group. Each unit cell has eight atoms, which increases the unit cell size to four times that of the 3C polytype. A schematic diagram of the 4H polyphonic phonon dispersion curve propagating along the c-axis is shown in Figure 1.2.4 (right)[9-11]. In the long-wavelength range, the normal mode is $4(A_1+B_1+E_1+E_2)$. The B_1 mode is Raman invalid, A_1 and E_1 mode are acoustic (LA, TA). Therefore, $3A_1$, $3E_1$, and $4E_2$ modes can be observed. Note that the symmetry of phonons in Figure 1.2.4 (right) is valid for phonons at propagation angle $\theta = 0^{\circ}$. For $\theta = 0^{\circ}$, the long-range electric field in the crystal turns the A_1 model to A_1 (LO) mode and the E_1 mode to E_1 (TO) mode. For $\theta = 90^{\circ}$, E_1 mode is divided into E_1 (LO) mode, and E_1 (TO) mode and A_1 mode converts A_1 (TO) mode. For the intermediate angle $\theta \neq 90^{\circ}$, the LO and TO modes have a mixed symmetry of A_1 and E_1 modes. Nevertheless, the E_2 mode is non-polar; it has nothing to do with the propagation angle. When corresponding to the backscattering geometry with c-plane as the surface, the E_2 mode is the most obvious and most easily observed. It is a non-polar mode that helps reduce the factors that can affect the Raman peak position.

1.3 SiC MOSFETs

Owing to the high critical field strength and high electron mobility along the c-axis, the Baliga`s figure-of-merit (BFOM)

of SiC is significantly higher than other SiC polytypes. This is the main reason why SiC is used almost exclusively for power device applications. Table 1.1 summarizes the major physical properties of Si and 4H-SiC[12-15]. The bandgap of 4H-SiC at room temperature is about 3.26 eV. The large bandgap significantly reduces the leakage current of the SiC device and makes the SiC device have excellent high-temperature operating characteristics. SiC has stable chemical properties and is not corroded by any chemical etchant at room temperature. In addition, SiC has high thermal conductivity, high breakdown electric field, and high saturation drift speed: twice the electron saturation speed of Si makes SiC devices have low conduction loss and excellent microwave characteristics; three times the thermal conductivity of Si makes SiC devices helps to dissipate heat from the SiC device, and improves the power density and integration of the SiC integrated circuit: a critical breakdown electric field ten times that of Si, which dramatically enhances the withstand voltage, operating frequency and current density of the SiC device, to make high voltage power devices with 600V to several thousand volts can be fabricated with drift layers with higher impurity concentration and thinner film thickness than Si devices. Since most of the resistance components of high-voltage power devices are the resistance of this drift layer, SiC can realize high-voltage devices with extremely low on-resistance per unit area. Theoretically, with the same breakdown voltage, the drift layer resistance per area can be reduced to 1/300 compared to Si. These excellent characteristics of SiC make it favorably used in high temperature, high frequency, high power, and radiation-resistant semiconductor devices. In addition, it is noted that SiC is the only wide-bandgap semiconductor material that can directly grow an insulating layer on its surface by thermal oxidation. In other words, many mature manufacturing technologies used in Si power devices can be directly applied to SiC devices.

Table 1.1 Basic material properties of Si, SiC,

Properties	**Si**	**4H-SiC**
Bandgap(eV)	1.12	3.26
Electron mobility $(cm^{-2}/Vs,\ N_D = 10^{17}\mathrm{cm}^{-3})$	1200	1000
Thermal conductivity $(\mathrm{W}\cdot\mathrm{cm}^{-1}\cdot K^{-1})$	1.5	4.9
Breakdown field **(MV/cm,** $N_D = 10^{17}\mathrm{cm}^{-3}$**)**	0.3	2.7
Saturated electron velocity $(10^{17}$**cm/s)**	1	2.2
Thermal oxide	○	○
BFOM **(n-type, parallel to c-axial) normalized by that of Si**	1	626
BFOM **(p-type, parallel to c-axial) normalized by that of Si, taking account of incomplete ionization of acceptors**	1	25

Compared with other compound semiconductors, SiC materials have an inherent advantage, that is, a SiO_2 gate oxide film can be directly formed on the SiC surface through an oxidation treatment, so it has great potential in the manufacture of MOS devices. SiC power devices (Schottky barriers and pin diodes, MOSFETs, IGBTs, GTOs) and high-frequency devices (MESFETs, SITs, RF JFETs) have been actively studied for the last ten years. Applications of SiC devices include automotive high-temperature sensors, motor drive systems, aerospace electronics, high-voltage DC power transmission, radar, and mobile communications. Recently, significant progress has been made in the fabrication technology of SiC MOSFETs capable of high withstand voltage, low loss, and high-frequency operation required for motor drive systems, switching power module, and high-voltage DC transmission (Figure 1.3.1[16]).

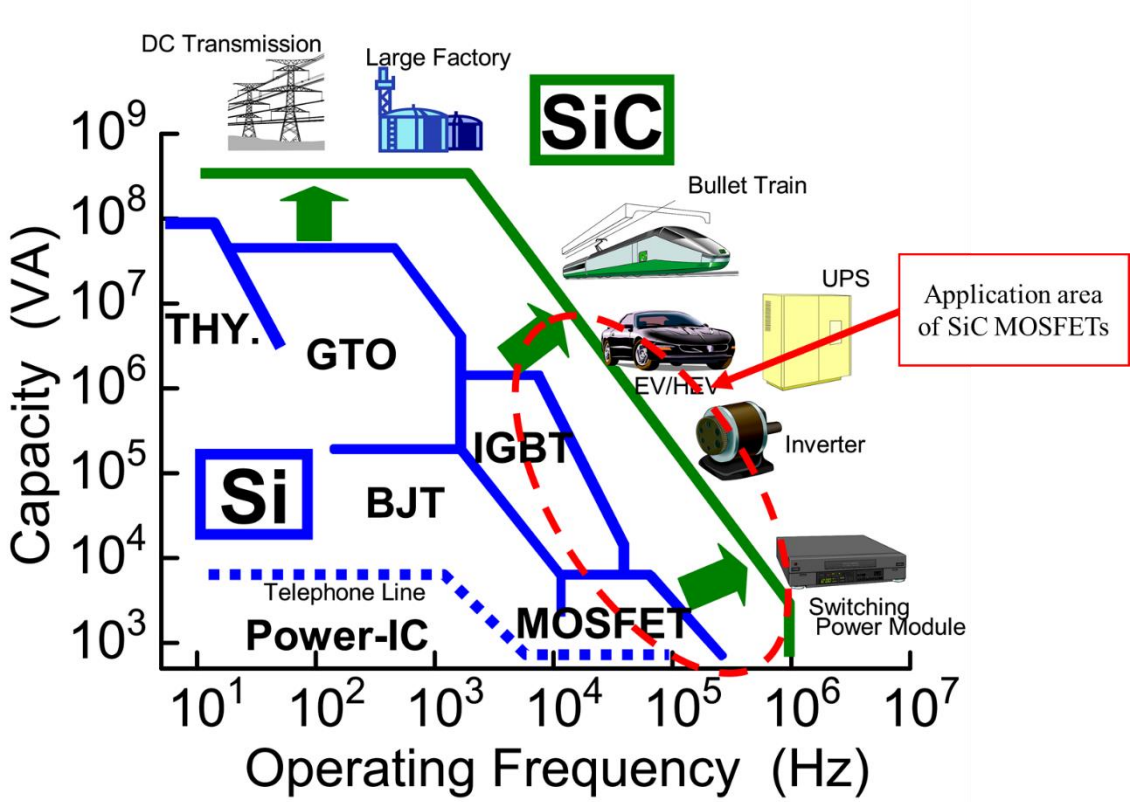

Figure 1.3.1 Current power devices application. [15]

1.3.1 Structure of the 4H-SiC MOSFETs

This MOSFET is a device having three terminals of a source, a drain, and a gate, as shown in Figure. 1.3.2 (a), and the semiconductor portion is made of SiC. As shown in Figure. 1.3.2 (b), by applying a voltage to the gate, a two-dimensional carrier layer called an inversion channel is formed between the source and the drain, thereby controlling the drain current between the source and the drain. When the charge carriers of the drain current are electrons, it is called an n-type MOSFET, and when they are holes, it is called a p-type MOSFET.

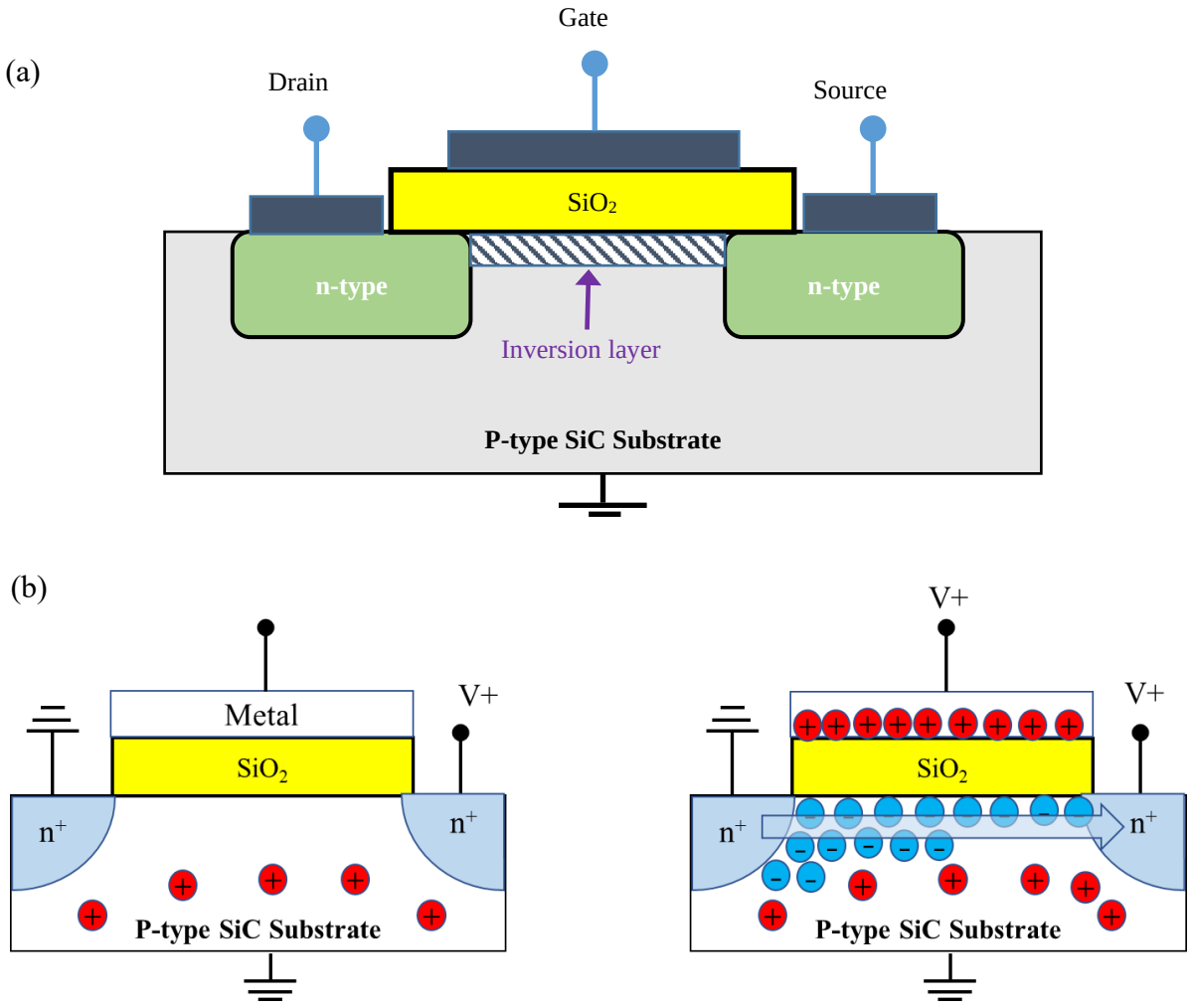

Figure. 1.3.2 (a) Schematic of SiC MOSFET, and (b) Schematic diagram of the working principle of p-type SiC-MOSFETs

The basic structure of a typical MOSFET is shown in Figure 1.3.3. (a) is a DiMOSFET widely used for Si power MOSFETs. In the case of SiC, since selective impurity doping is usually performed by ion intrusion, this structure, called a DiMOSFET, is advantageous in increasing the breakdown voltage. (b) is a UMOSFET (trench gate MOSFET). Although it is the structure that can reduce the on-resistance most, it is difficult to control the trench process. The breakdown voltage and on-resistance as indices representing the performance of the power MOSFET. First, regarding the breakdown voltage, the ideal element breakdown voltage is determined by the carrier density and thickness of the n-drift layer. The on-resistance is the sum of the resistances of the current path, as shown in Figure 1.3.3. (a). Ideally, if the other resistance components are negligibly small concerning the drift resistance, the on-resistance of the MOSFET becomes the theoretical limit value of SiC. However, since the MOS interface characteristics are sparse at present, the channel resistance is larger than the drift resistance. Therefore, how to improve the interface properties of the MOS and thereby reduce the channel resistance is the core topic of the development of SiC-MOSFETs.

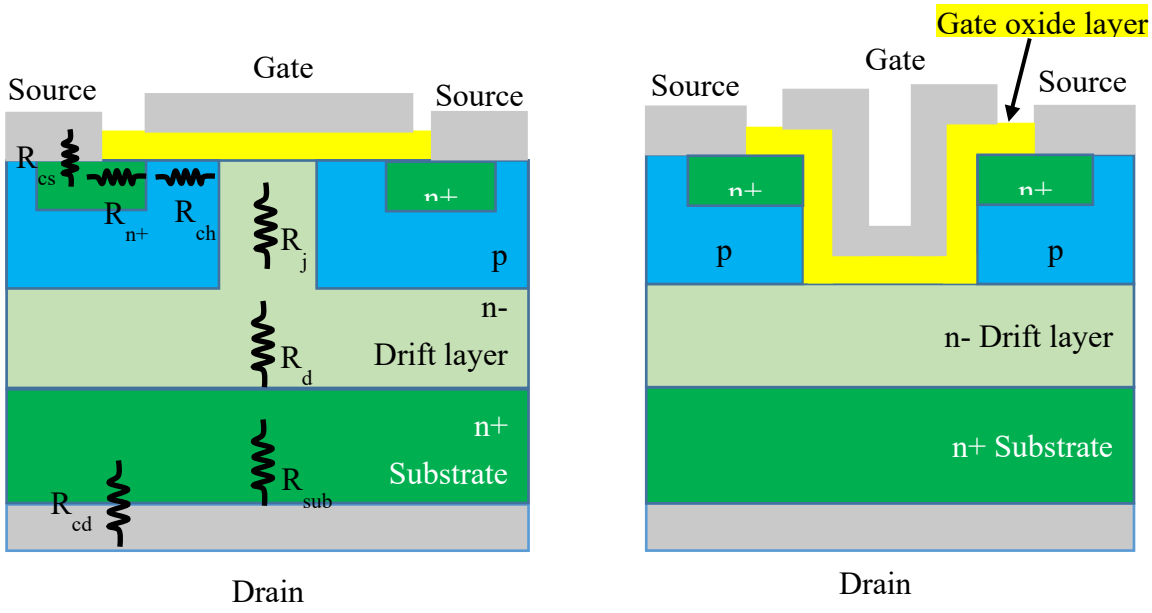

(a) DiMOSFET (b) UMOSFET

Figure 1.3.3 Basic structure of MOSFET

1.3.2 Interface properties of 4H-SiC MOS

As we know, in 4H-SiC MOSFETs, the electrons generated in the inversion layer are trapped by the high density of interface traps and near interface oxide charges[17]. Thus the poor quality of the SiO_2/SiC interface can severely limit the value of channel mobility[18, 19]. So far, researchers have identified some defects, e.g., silicon dangling bonds at SiC surface[20, 21], interstitial residual carbon clusters[22, 23], and oxygen vacancy in the oxide[24, 25], and near-interface

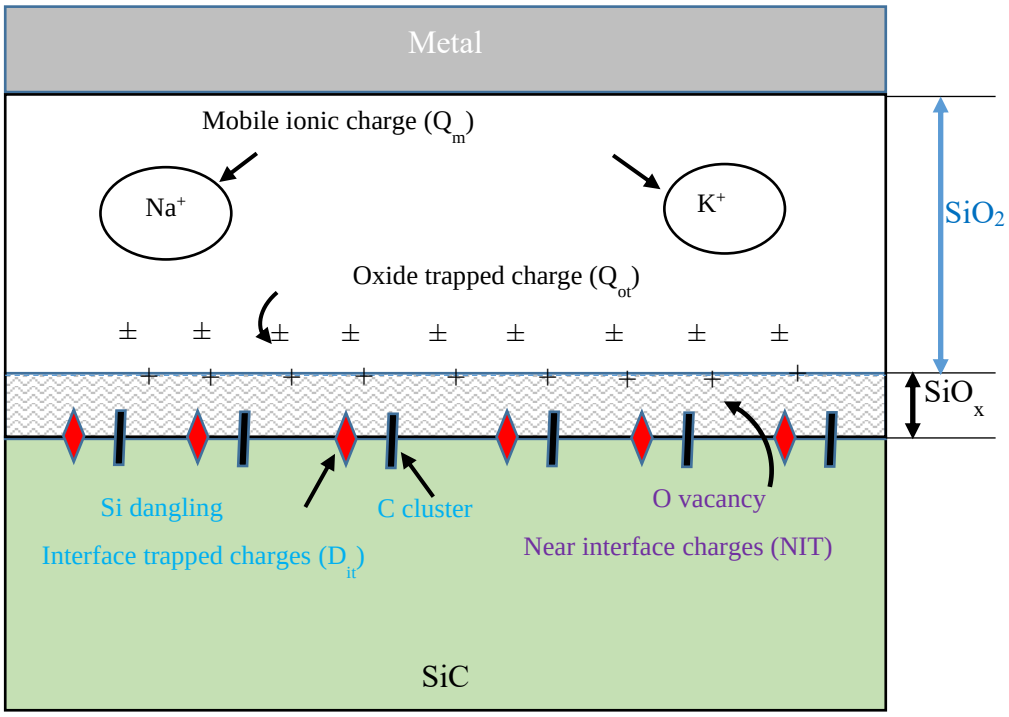

Figure 1.3.4 Schematic representation of the defects present in the SiC MOS interface

traps (NITs) near the SiC conduction band edges (E_C), as well as interface structure[26-28]. The different types of

charges[29] are schematically represented in Figure 1.3.4. In addition, most probably, a high strain of interface atomic layers is responsible for the creation of electrically active traps[30].

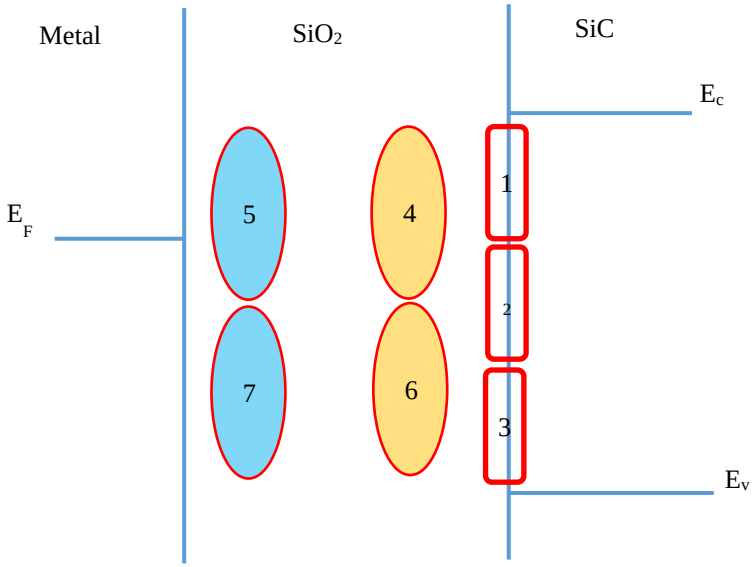

Figure 1.3.5 Interface states distribution.

The interface states due to these defects, such as 1) Interface state (fast states), 2) Deep interface state (slow states), 3) Interface state near E_v, hole trapped(minus shift of threshold voltage), 4) Near interface trap-NIT (electron trapped), 5) Electron trapped in SiO_2, 6) Near interface trap-NIT (hole trapped), 7) Hole trapped in SiO_2, decreased the electron transport properties at the SiC-MOSFETs interface. The interface states distribution due to these charges is schematically represented in Figure 1.3.5. For these interfacial defects, a lot of studies have been performed to determine the origin of the defects that cause low electron mobility and to find the elimination and passivation technical methods for these defects. Interfacial nitridation by NO (nitric oxide)[31] or N_2O (nitrous oxide)[32-34] gases with post-oxidation annealing have effectively reduced the SiO_2/SiC interface states density since nitrogen atoms can mold strong $Si \equiv N$ bonds, passivation of interface traps due to dangling is passivated. In addition, they can be used to clear up the unique carbon clusters and complex silicon-oxycarbon bonds in the SiC oxidation process[35]. This bond is believed to be the cause of the rapid traps at the SiO_2 / SiC interface[36]. Annealing in H_2[37, 38], which is very effective at passivating silicon-oxycarbon bonds, in addition, the increased hydrogen might reduce near-interfacial oxide traps, due to an enhanced -H passivation effect. Annealing at $POCl_3$ ambient has an effective reduction in the Si and/or C dangling bonds and carbon clusters[39]. Compared to the thermal oxidation samples[40], although these methods have improved the electron mobility of the inversion layer, the electron mobility remains as low as 40–90 $cm^2 \cdot V^{-1} \cdot s^{-1}$, as shown in Table 1.3.1.

Table 1.3.1 Summary of field-effect mobility $\boldsymbol{\mu}$ and interface state density $\boldsymbol{Dit}$ data in 4H-SiC MOSTEFs and MOS capacitors.

Process	Temperature (℃)	$\boldsymbol{\mu}$ $(\boldsymbol{cm^2V^{-1}S^{-1}})$	$\boldsymbol{D_{it}}$ $(\boldsymbol{cm^2eV^{-1}})$	
Dry oxidation	1175	4	9×10^{14}	[24]
NO	1250	20	$3\sim6 \times 10^{12}$	[29]
N_2O	1150	24-40	$4\sim8 \times 10^{11}$	[30]
H_2	1150	27	2.0×10^{12}	[35]
$POCl_3$	1000	90	2.8×10^{11}	[37]

So far. Interface defects of SiO_2/SiC have been studied for decades. Although researchers have identified some interface defects and have developed corresponding interface defect passivation methods for these identified defects. However, the carrier mobility in the inversion layer of SiC-MOSFETs is still far from the ideal value. Therefore, we have to re-examine what is the origin of the interface defects. Recently, some theoretical and experimental studies have found that high-temperature thermal oxidation induced strain results in the formation of an interface state[41-43]. It is believed as one of the reasons for the alteration of the carrier transport properties.

1.4 Thermal oxidation induced stress at the interface of SiO_2/SiC

1.4.1 Stress generation at the interface of SiO_2/SiC

Since the origin of interfacial stress in the SiO_2/4H-SiC system was considered as (1) the different thermal expansion between the SiC substrate and the SiO_2 oxide film, and (2) the atomic density mismatch between the substrate and oxide film during high-temperature oxidation. Since the molecule volume of SiO_2 is more significant than the molecule volume of SiC, on the other hand, the thermal expansion coefficient of SiO_2 is much smaller than SiC. The specific parameter values are shown in Table 1. During the cooling process of high-temperature dry thermal oxidation, SiC shrinks much more than SiO_2. As Figure 1.3.6 shown, the SiO_2 film on the SiC substrate should bend into a spherical bowl shape. This results in biaxial compression in the SiO_2 films on SiC substrate surface, while biaxial tension is generated in the surface of the SiC substrate.

Table 1.4.1 Values of the atomic density and expansion coefficient of SiO_2 and SiC

	SiO_2	**SiC**
Si density (10^{22} atom/cm^3)	2.2	4.8
Thermal expansion coefficient (10^{-6}/℃)	0.5	2.9

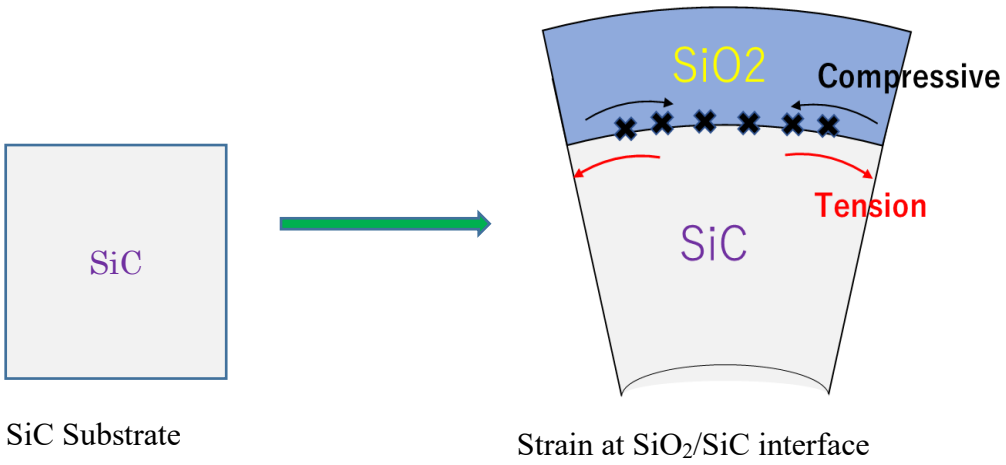

Figure 1.4.1 Interfacial stress generation of SiO_2/SiC during the dry thermal oxidation.

It is worth noting that the interface stress induced by the high-temperature oxidation can be neglected in the SiO_2/Si system since the viscoelastic phenomenon at the interface. However, in the SiO_2/SiC system, this interface stress induced by the strain at the interface may introduce the effect on the variation of the carrier transport properties at the inversion layer of the SiC-MOS.

1.4.2 Research status of stress at the SiO_2/4H-SiC interface

In 2013, Kenta et al.[44] have reported a new type of defect generation at a 4H-SiC/SiO_2 interface by oxidation induced compressive strain and shown that a substantial structural change occurred to release compressive strain and C-C defect structure. These C-C defects were formed by only oxidation without and excess C atoms. In 2014, a first-principles calculation suggested that strain at the interface of 4H-SiC/SiO_2 due to the high-temperature thermal oxidation can induce the bandgap change of SiC.[42] Furthermore, the near interface strain induced by thermal oxides grown on 4H-SiC has been studied by Hirai et al.[45] and Kita et al. have been identified that tensile lattice distortions at the interface of SiC/SiO_2 due to the difference of the Si density between SiC substrate and amorphous-SiO_2[46] For the Si/SiO_2 system. The interface strain-induced stress can be neglected because of the viscoelastic phenomenon. However, we have reason to believe that the interface stress of SiC/SiO_2 should be related to the electron mobility at the inversion layer of SiC-MOSFETs.

1.4.3 Effect of stress on the electron mobility

The interface stress-induced lattice distortion may affect the electron mobility in two possible ways: 1) Generation of deformation potential[47-50]; 2) Formation of the interface defects[41, 42]. Schematic diagram 1.4.2 shows the change in the electron transport properties under the affection of deformation potential, generated from the strained crystal structure caused by the stress generation. We can imagine that in a perfect crystal without strain, the electrons are only affected by the initial periodic potential and move smoothly in the crystal. However, in a deformed crystal, the electrons are not only affected by the initial periodic potential energy, but also by the deformation potential induced by the crystal distorted. Under the action of the double potential energy, the electron transport characteristics should be changed.

Figure 1.4.2 Schematic diagram of the electron transport under the deformation potential

In terms of the formation of interface defects, the currently identified defect formation mechanism is that the stress-induced deformation can cut off the chemical bonds, resulting in the generation of some dangling bonds, such as Si dangling bonds and C dangling bonds on the SiC surface. In addition, the occurrence of interface oxygen defects under stress makes the SiO_2 / SiC interface more complicated and uncertain. It should be noted that at present, there is no mature and reliable theoretical explanation for the mechanism of defects caused by interfacial stress, and further research is needed.

1.5 Motivation and objective of the research

Although in recent years, it has been recognized that in SiC-MOSFETS devices, interfacial stress caused by high-temperature thermal oxidation may have a tremendous impact on electron transport performance. However, so far, the understanding of the underlying physical mechanism of this effect is far from enough. Therefore, in order to be able to understand how the interfacial stress affects the electron transport characteristics, we have set our objectives as follows:

①. To develop a stress measurement system to directly evaluate the stress on the SiC surface in the SiO_2 / SiC system, and then to quantify the stress value. On we consider that only based on the quantified stress value can we accurately evaluate how stress affects the transport properties electron in the channel of SiC-MOS structure.

②. Because there is no perfect theoretical reference for the influence of interfacial stress on electron mobility, it is necessary to obtain the relationship between them through theoretical simulation.

③. Based on understanding the principle that interface stress affects electron mobility, our goal is to develop a fabrication method for SiC-MOS structures that outperforms current SiO_2/SiC interface performance.

1.6 Thesis organization

This work is divided into three main parts:

In chapter 2, we first want to discuss an interface stress measurement system that can directly test the surface deformation of SiC by using Raman spectroscopy and confocal microscopy. Then, how to quantify the interfacial stress based on the measured strain, and the effect of the NO POA treatment on the interfacial stress will be discussed.

In chapter 3, we will theoretically evaluate the relationship between the interface stress and the electron mobility through the calculation of the phonon-limited electron mobility based on the phonon scattering theory in the 3D and 2D models. Based on the actual stress values at the thermal oxidation interface obtained in the previous chapter, we will discuss the relationship between interface stress and the channel electron mobility in real thermal oxidation MOS devices.

In chapter 4, we will discuss a new fabrication of an oxide layer for SiC-MOS structure at low-temperature. It not only can be used to suppress the generation of interfacial stress due to alteration in oxidation temperature but also can eliminate the interface traps density.

Finally, in chapter 5, we will give the conclusions about the investigation of biaxial stress effect on electric properties at the 4H-SiC-MOS interfaces.

1.7 Reference

[1] B.J. Baliga, Fundamentals of power semiconductor devices, Springer Science & Business Media, 2010.

[2] J. Lutz, H. Schlangenotto, U. Scheuermann, R.J.P. De Doncker, characteristics, reliability, Semiconductor power devices, 2011.

[3] M.E. Levinshtein, S.L. Rumyantsev, M.S. Shur, Properties of Advanced Semiconductor Materials: GaN, AIN, InN, BN, SiC, SiGe, John Wiley & Sons, 2001.

[4] Z. Li, R.C. Bradt, Thermal-Expansion of the Hexagonal (H-4) Polytype of Sic, Journal of Applied Physics, 60 (1986) 612-614.

[5] V. Bougrov, M. Levinshtein, S.L. Rumyantsev, A.J.E.L.M. Zubrilov, Rumyantsev SL, Shur MS, John Wiley, I. Sons, New York, Properties of Advanced Semiconductor Materials GaN, AlN, InN, BN, SiC, SiGe, (2001) 1-30.

[6] C. Persson, U. Lindefelt, Relativistic band structure calculation of cubic and hexagonal SiC polytypes, Journal of Applied Physics, 82 (1997) 5496-5508.

[7] F. Bechstedt, P. Kackell, A. Zywietz, K. Karch, B. Adolph, K. Tenelsen, J. Furthmuller, Polytypism and properties of silicon carbide, Phys Status Solidi B, 202 (1997) 35-62.

[8] D.W. Feldman, J.H. Parker, W.J. Choyke, L. Patrick, Phonon Dispersion Curves by Raman Scattering in SiC, Polytypes3C,4H,6H,15R, and21R, Physical Review, 173 (1968) 787-793.

[9] D. Feldman, J.H. Parker Jr, W. Choyke, L.J.P.R. Patrick, Phonon dispersion curves by raman scattering in SiC, Polytypes 3 C, 4 H, 6 H, 1 5 R, and 2 1 R, 173 (1968) 787.

[10] P.J. Colwell, M.V. Klein, Raman Scattering from Electronic Excitations in N-Type Silicon Carbide, Physical Review B, 6 (1972) 498-&.

[11] S. Nakashima, H. Harima, Raman investigation of SiC polytypes, Phys Status Solidi A, 162 (1997) 39-64.

[12] G. Harris, H. Henry, A.J.I.o.E.E. Jackson, INSPEC, London, Properties of Silicon Carbide, edited by GL Harris, 1995.

[13] S. Adachi, Properties of semiconductor alloys: group-IV, III-V and II-VI semiconductors, John Wiley & Sons, 2009.

[14] R.C. Marshall, Silicon carbide--1973: proceedings, Univ of South Carolina Pr, 1974.

[15] G. Pensl, F. Ciobanu, T. Frank, M. Krieger, S. Reshanov, F. Schmid, M.J.I.j.o.h.s.e. Weidner, systems, SiC material properties, 15 (2005) 705-745.

[16] H. Yano, MOS interface defect reduction technology to improve the performance of SiC power devices.

[17] T. Kimoto, J.A. Cooper, Fundamentals of silicon carbide technology: growth, characterization, devices and applications, John Wiley & Sons, 2014.

[18] P. Friedrichs, E.P. Burte, R. Schörner, Interface properties of metal-oxide-semiconductor structures onn-type 6H and 4H-SiC, Journal of Applied Physics, 79 (1996) 7814-7819.

[19] S. Dimitrijev, H. Harrison, P. Tanner, K. Cheong, J. Han, Oxidation, MOS capacitors, and MOSFETs, in: SiC power materials, Springer, 2004, pp. 345-373.

[20] G.G. Jernigan, R.E. Stahlbush, N.S. Saks, Effect of oxidation and reoxidation on the oxide-substrate interface of 4H-and 6H-SiC, Applied Physics Letters, 77 (2000) 1437-1439.

[21] T. Ohnuma, H. Tsuchida, T. Jikimoto, A. Miyashita, M. Yoshikawa, Interface States in SiO2/4H-SiC (0001) Interfaces from First-Principles: Effects of Si-Si Bonds and of Nitrogen Atom Termination, in: Materials Science

Forum, Trans Tech Publ, 2005, pp. 573-576.
[22] V.V. Afanasev, M. Bassler, G. Pensl, M. Schulz, Intrinsic SiC/SiO2 Interface States, physica status solidi (a), 162 (1997) 321-337.
[23] P. Deak, J.M. Knaup, T. Hornos, C. Thill, A. Gali, T. Frauenheim, The mechanism of defect creation and passivation at the SiC/SiO2 interface, J Phys D Appl Phys, 40 (2007) 6242-6253.
[24] J. Dekker, K. Saarinen, H. Olafsson, E.O. Sveinbjornsson, Observation of interface defects in thermally oxidized SiC using positron annihilation, Applied Physics Letters, 82 (2003) 2020-2022.
[25] V. Afanas' ev, A.J.A.p.l. Stesmans, Hole traps in oxide layers thermally grown on SiC, 69 (1996) 2252-2254.
[26] Q.Z. Zhu, L.Q. Huang, W.B. Li, S.M. Li, D.J. Wang, Chemical structure study of SiO2/4H-SiC (0001) interface transition region by angle-dependent x-ray photoelectron spectroscopy, Applied Physics Letters, 99 (2011) 082102.
[27] J.-L. Cantin, H. Von Bardeleben, Y. Shishkin, Y. Ke, R. Devaty, W.J.P.r.l. Choyke, Identification of the Carbon Dangling Bond Center at the 4 H− S i C/S i O 2 Interface by an EPR Study in Oxidized Porous SiC, 92 (2004) 015502.
[28] E. Pippel, J. Woltersdorf, H.Ö. Ólafsson, E.Ö. Sveinbjörnsson, Interfaces between 4H-SiC and SiO2: Microstructure, nanochemistry, and near-interface traps, Journal of Applied Physics, 97 (2005) 034302.
[29] M. Krieger, S. Beljakowa, B. Zippelius, V.V. Afanas' ev, A.J. Bauer, Y. Nanen, T. Kimoto, G. Pensl, Detection and electrical characterization of defects at the SiO2/4H-SiC interface, in: Materials Science Forum, Trans Tech Publ, 2010, pp. 463-468.
[30] M. Cabello, V. Soler, G. Rius, J. Montserrat, J. Rebollo, P. Godignon, Advanced processing for mobility improvement in 4H-SiC MOSFETs: A review, Mat Sci Semicon Proc, 78 (2018) 22-31.
[31] H. Yoshioka, J. Senzaki, A. Shimozato, Y. Tanaka, H. Okumura, Effects of interface state density on 4H-SiC n-channel field-effect mobility, Applied Physics Letters, 104 (2014) 083516.
[32] T. Kimoto, Y. Kanzaki, M. Noborio, H. Kawano, H. Matsunami, Interface Properties of Metal–Oxide–Semiconductor Structures on 4H-SiC{0001} and (11¥bar20) Formed by N2O Oxidation, Japanese Journal of Applied Physics, 44 (2005) 1213-1218.
[33] P. Zhao, Rusli, Y. Liu, C.C. Tin, W.G. Zhu, J. Ahn, Investigation of 4H-SIC MOS capacitors annealed in diluted N2O at different temperatures, Microelectronic Engineering, 83 (2006) 61-64.
[34] G.Y. Chung, C.C. Tin, J.R. Williams, K. McDonald, M. Di Ventra, S.T. Pantelides, L.C. Feldman, R.A. Weller, Effect of nitric oxide annealing on the interface trap densities near the band edges in the 4H polytype of silicon carbide, Applied Physics Letters, 76 (2000) 1713-1715.
[35] P. Jamet, S. Dimitrijev, P. Tanner, Effects of nitridation in gate oxides grown on 4H-SiC, Journal of Applied Physics, 90 (2001) 5058-5063.
[36] V.V. Afanas'ev, A. Stesmans, F. Ciobanu, G. Pensl, K.Y. Cheong, S. Dimitrijev, Mechanisms responsible for improvement of 4H–SiC/SiO2 interface properties by nitridation, Applied Physics Letters, 82 (2003) 568-570.
[37] T. Teraji, S. Hara, H. Okushi, K.J.A.p.l. Kajimura, Ideal Ohmic contact to n-type 6H-SiC by reduction of Schottky barrier height, 71 (1997) 689-691.
[38] M. Okamoto, Y. Makifuchi, M. Iijima, Y. Sakai, N. Iwamuro, H. Kimura, K. Fukuda, H. Okumura, Coexistence of Small Threshold Voltage Instability and High Channel Mobility in 4H-SiC($000¥bar{1}$) Metal–Oxide–Semiconductor Field-Effect Transistors, Applied Physics Express, 5 (2012) 041302.

[39] D. Okamoto, H. Yano, K. Hirata, T. Hatayama, T. Fuyuki, Improved Inversion Channel Mobility in 4H-SiC MOSFETs on Si Face Utilizing Phosphorus-Doped Gate Oxide, Ieee Electron Device Letters, 31 (2010) 710-712.
[40] T. Hatakeyama, Y. Kiuchi, M. Sometani, S. Harada, D. Okamoto, H. Yano, Y. Yonezawa, H. Okumura, Characterization of traps at nitrided SiO2/SiC interfaces near the conduction band edge by using Hall effect measurements, Applied Physics Express, 10 (2017) 046601.
[41] C.J. Kirkham, T. Ono, First-Principles Study on Interlayer States at the 4H-SiC/SiO2Interface and the Effect of Oxygen-Related Defects, Journal of the Physical Society of Japan, 85 (2016) 024701.
[42] K. Shiraishi, K. Chokawa, H. Shirakawa, K. Endo, M. Araidai, K. Kamiya, H. Watanabe, First principles study of SiC/SiO 2 interfaces towards future power devices, in: 2014 IEEE International Electron Devices Meeting, IEEE, 2014, pp. 21.23. 21-21.23. 24.
[43] A.D. Hatmanto, K. Kita, Thermal-oxidation-induced local lattice distortion at surface of 4H-SiC(0001) characterized by in-plane X-ray diffractometry, Applied Physics Express, 11 (2018) 011201.
[44] K. Chokawa, S. Kato, K. Kamaiya, K. Shiraishi, A New-Type of Defect Generation at a 4H-SiC/SiO2 Interface by Oxidation Induced Compressive Strain, in: Materials Science Forum, Trans Tech Publ, 2013, pp. 469-472.
[45] H. Hirai, K.J.A.P.L. Kita, Difference of near-interface strain in SiO2 between thermal oxides grown on 4H-SiC by dry-O2 oxidation and H2O oxidation characterized by infrared spectroscopy, 110 (2017) 152104.
[46] A.D. Hatmanto, K.J.A.P.E. Kita, Thermal-oxidation-induced local lattice distortion at surface of 4H-SiC (0001) characterized by in-plane X-ray diffractometry, 11 (2017) 011201.
[47] Y. Sun, S.E. Thompson, T. Nishida, Strain effect in semiconductors: theory and device applications, Springer Science & Business Media, 2009.
[48] Q. Yan, P. Rinke, M. Scheffler, C.G. Van de Walle, Strain effects in group-III nitrides: Deformation potentials for AlN, GaN, and InN, Applied Physics Letters, 95 (2009).
[49] S.K. Jana, S. Ghosh, S.M. Dinara, T.D. Das, D. Biswas, Strain Effects on Band Structure of Wurtzite InGaN/GaN Quantum Well on Si Substrate, IOP Conference Series: Materials Science and Engineering, 73 (2015).
[50] K. Rim, R. Anderson, D. Boyd, F. Cardone, K. Chan, H. Chen, S. Christansen, J. Chu, K. Jenkins, T. Kanarsky, S. Koester, B.H. Lee, K. Lee, V. Mazzeo, A. Mocuta, D. Mocuta, P.M. Mooney, P. Oldiges, J. Ott, P. Ronsheim, R. Roy, A. Steegen, M. Yang, H. Zhu, M. Ieong, H.S.P. Wong, Strained Si CMOS (SS CMOS) technology: opportunities and challenges, Solid-State Electronics, 47 (2003) 1133-1139.

Chapter 2 Investigation of stress at SiO_2/4H-SiC interface induced by thermal oxidation by confocal Raman microscopy

2.1 Introduction

During the high-temperature thermal oxidation of SiC, the induced strain at the interface of SiO_2/SiC, resulting in the formation of stress. It is supposed as one of the reasons for the interface defect formation. On the other hand, as we know, the crystal distortion generates at the interface of a heterojunction, due to the different thermal expansion, and the atomic density mismatch between two materials. The crystal distortion will extinguish the original periodic potential of the crystal by the generation of a deformation potential, resulting in the change of the electron transport characteristics. Therefore, in order to systematically study the effect of interfacial stress on channel electron mobility of SiC-MOSFETs, first and foremost is to find a suitable method for evaluating interfacial stress of SiO_2/4H-SiC. Moreover, it has been claimed that the interfacial nitridation by nitric oxide (NO) gas in post-oxidation annealing (POA) is found to effectively passivated the defects at the SiO_2/SiC interface[1-5], and yield field-effect mobilities of 40-80cm^2/Vs in 4H-SiC MOSFETs[6, 7]. However, the relationship between stress and the defect in the process of NO POA treatment is unclear. In this work, we investigated the stress at the interface of SiO_2/4H-SiC samples, which were annealed by NO at different times, to understand the underlying physics of the effect of NO annealing on defect induced by stress, using a confocal Raman microscopy technique.

2.2 Confocal Raman microscopy measurement system

Several kinds of techniques, such as Fourier transform infrared spectroscopy (FTIR)[8, 9], and double-beam reflection[10-12], were used in measuring the stress distribution in SiO_2-side of the SiO_2/SiC interface. Nevertheless, it has been difficult to examine the residual stress located in the region that was close to the surface of the SiC substrate directly.

2.2.1 Raman Scattering Theory

Molecules are generally electrically neutral in the absence of an electric field. When an electric field is applied to them, the electron cloud is strained, and an induced dipole moment is generated. As shown in Figure 2.1, when light is radiated, the induced dipole moment vibrates according to the vibration of the photoelectric field, and scattered light having the same frequency as the irradiated light is generated. This is the Rayleigh scattered light that accounts for most of the scattered light. On the other hand, molecules have their natural vibration. The "frequency shift" occurs due to the interference between the vibration of the electric field of the light (frequency ω_0) and the natural vibration (frequency ω). That is, the scattered light includes the frequencies of the components $(\omega_0 - \omega)$ and $(\omega_0 + \omega)$ in addition to the same frequency as the vibration of the dipole moment. The light due to these two components is called Raman scattered light.

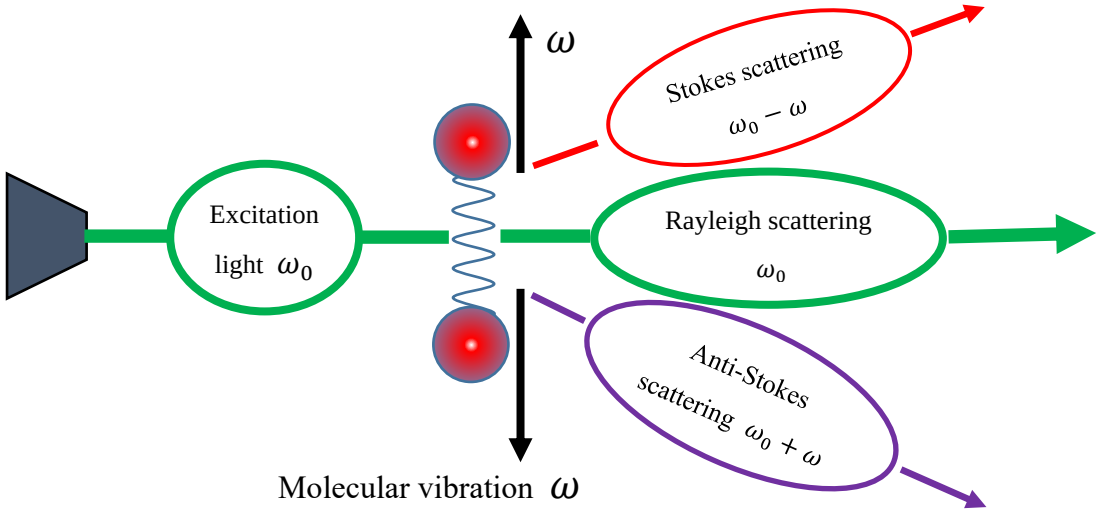

Figure 2.1 Images of Raman and Rayleigh scattering

In terms of the vibration energy, when light is scattered from a molecule, there are three possible results which show in Figure 2.2. First, as shown in the green transition process, the molecule can relax back to the ground state and emit a photon with the same energy as the incident photon. This process is called Rayleigh scattering and is a complete elastic process. Second, the red transition in the figure, the molecule, allows for relaxing to the actual phonon state and emit photons with less energy than the incident photons. This is called Stokes shift Raman scattering and is a non-complete elastic process. The third possible result is that in the purple process in the figure, the molecule is already in the excited phonon state, is excited to a higher virtual state, and then relaxes back to the ground state. The emitted photon has more energy than the incident photon. This is called an anti-Stokes shift Raman scattering and is a non-completely elastic process. Since most molecules are in the ground state at room temperature, it is unlikely that anti-Stocks will scatter photons.

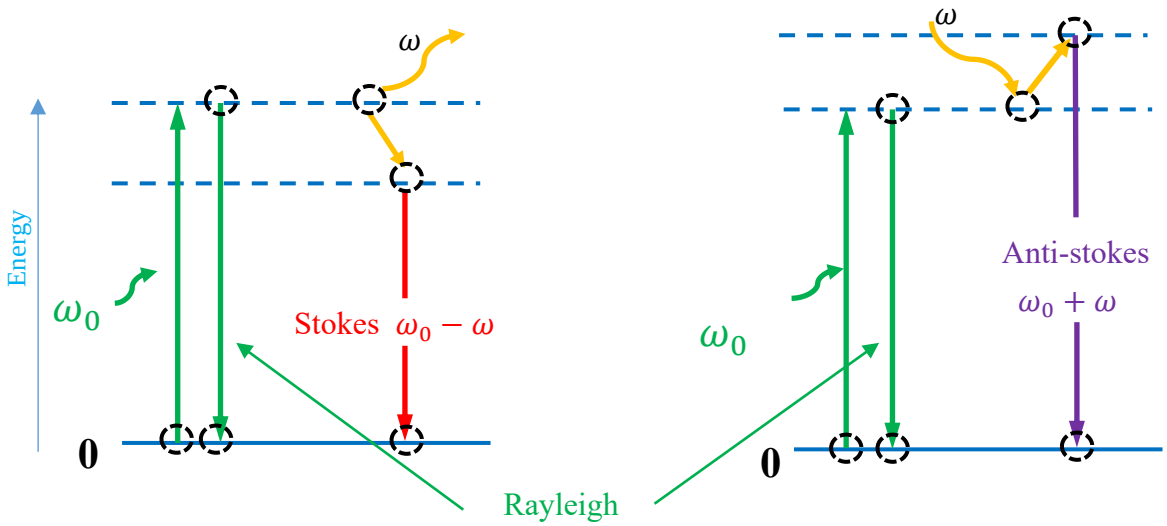

Figure 2.2 Vibration energy level

2.2.2 Frequency Dependence of Raman Scattering

As mentioned above, the dipole moment is induced during the interaction of the incident light with the light-material. P is the strength of the induced dipole moment, which can be written as

$$P = \alpha \bar{E}, \quad (2.1)$$

here α is the molecular polarizability, which is a material property that depends on the molecular structure and properties of the bond. $\bar{E}$ is the external electric field, which can be given by

$$\bar{E} = E_0 \cos(2\pi\omega_0 t), \quad (2.2)$$

where ω_0 is the frequency of the incident light. From Eqs. (2.1) and (2.2), the time-dependent induced dipole moment can be expressed as

$$P = \alpha E_0 \cos(2\pi\omega_0 t), \quad (2.3)$$

Since the ability of a local electron cloud to perturb a molecular structure depends on the relative positions of individual atoms, polarizability is a function of the instantaneous positions of the constituent atoms. For any molecular bond, a single atom is confined to a specific vibration mode, in which vibration energy levels are quantified like the energy of electrons. The vibration energy of a specific model is given by

$$E_{vib} = \left(j + \frac{1}{2}\right) h\omega_{vib}, \quad (2.4)$$

where j is the vibrational quantum number (j = 0, 1, 2…), ω_{vib} is the frequency of the vibrational mode, and h is the Planck constant. According to a specific vibration mode, the physical displacement dQ of an atom near its equilibrium position can be expressed as

$$dQ = Q_0 \cos(2\pi\omega_{vib} t), \quad (2.5)$$

where Q_0 is the maximum displacement about the equilibrium position. Generally, for a typical diatomic molecule, the maximum displacement is about 10% of its bond length. In other words, the displacement is very small, so the polarizability can be approximated by Taylor series expansion, that is,

$$\alpha = \alpha_0 + \frac{\partial \alpha}{\partial Q} dQ, \quad (2.6)$$

where α_0 is the polarizability of the molecular mode at an equilibrium position. Based on the Eqs. (2.3), (2.5), and (2.6), the time-dependent induced dipole moment can be represented as

$$P = \alpha_0 E_0 \cos(2\pi\omega_0 t) + \frac{\partial\alpha}{\partial Q} Q_0 \cos(2\pi\omega_{vib} t)\, E_0 \cos(2\pi\omega_0 t), \quad (2.7)$$

Using a trigonometric identity, the Eq. (2.7) can be recast as

$$P = \alpha_0 E_0 \cos(2\pi\omega_0 t) + \left(\frac{\partial\alpha}{\partial Q}\frac{Q_0 E_0}{2}\right)\{\cos[2\pi(\omega_0 - \omega_{vib})t\} + \cos[2\pi(\omega_0 + \omega_{vib})\}, \quad (2.8)$$

The above equations show that the induced dipole moments occurred at three different frequencies, namely ω_0, $(\omega_0 - \omega_{vib})$ and $(\omega_0 + \omega_{vib})$, corresponding to Rayleigh scattering light, stikes scattering light and anti-stokes scattering light, respectively, as shown in Figure 2.3. Usually, most Raman measurements are made only when considering Stocks Shifted light.

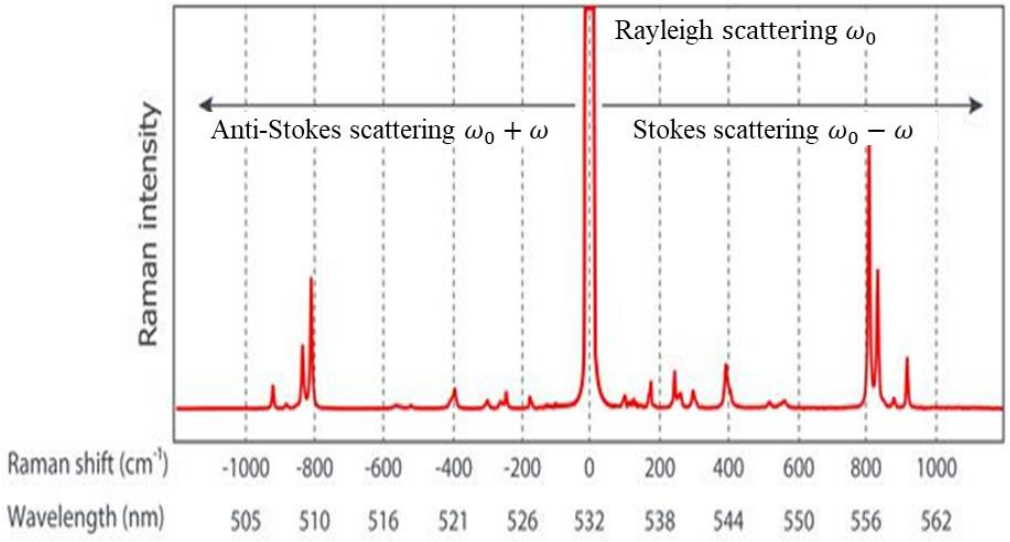

Figure 2.3 Scattering spectrum include: Rayleigh scattering, anti-Stokes scattering and Stokes scattering (Raman scattering).

2.2.3 Raman peak shift and stress

As mentioned in the previous section, the position of a substance's Raman peak corresponds to its natural minute vibration frequency, and the crystal structure of the material determines this frequency, that is, the bond length of the atoms that make up the substance. When the bond length changes, the frequency of the material will also change corresponding to the change in bond length. Using Hooke`s law (Equation 2.9), it is easy to understand the approximate, which relates the bond strength to the vibrational frequency.

$$\omega = \frac{1}{2\pi c}\sqrt{\frac{K}{m}}, \quad (2.9)$$

where c is the velocity of light, K is the force constant of the bond between A and B, and m is the reduced mass of atoms A and B of massed M_A and M_B;

$$m = \frac{M_A M_B}{M_A + M_B}, \quad (2.10)$$

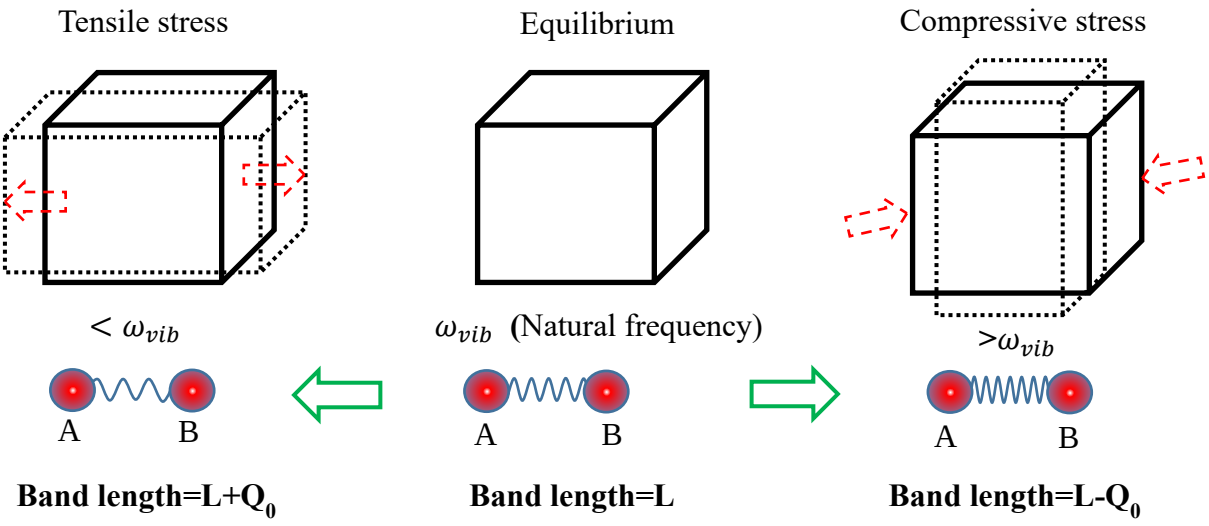

Figure 2.4 Relationship between stress and frequency vibration

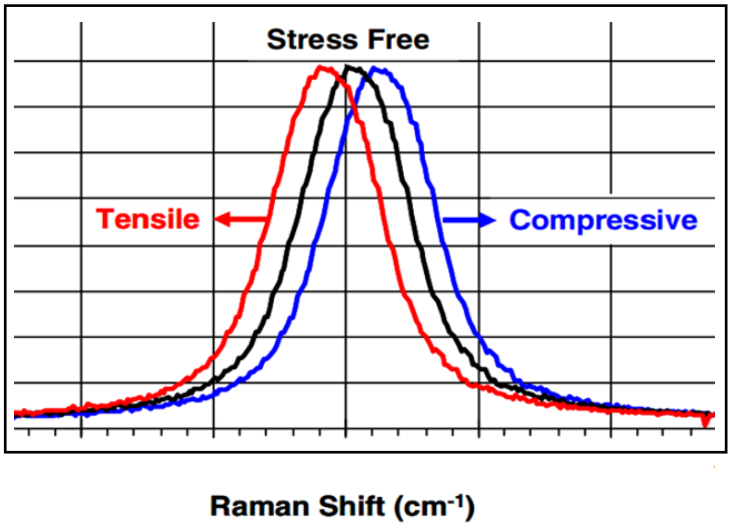

Figure 2.5 Raman peak shifts due to tensile and compression stress

Thus, Raman spectroscopy is a widely used characterization technique that analyzes the spectrum of inelastic scattering light with a frequency shift. Under the applied compressive or tensile stress, a crystal structure becomes distorted. As a result, the bond strength changed due to the alteration of the band length. Raman peaks corresponding to a particular crystal structure and molecular vibration of the substance will shift under tensile and compressive, as shown in Figure 2.4. Since the peak wavenumber is proportional to stress, as shown in Figure 2.5, the amount of strain can be accurately measured by measuring the precise wavenumber shift. Thus, this method has been popularly adopted for estimating the residual stress in semiconductors[13-16].

2.2.4 Penetration depth in 4H-SiC and Confocal microscopy system

The stresses in the SiC wafer and device have also been precisely evaluated using Raman spectroscopy by many groups[17, 18]. However, Raman spectroscopy is rarely used to evaluate the surface or interface properties of 4H-SiC. The reason is that the absorption coefficient of 4H-SiC in the visible light region is relatively low, resulting in the penetration depth of Raman is tremendous. In the backscattering geometry, the material absorbs the scattered photons on the way back. The effective penetration depth δ is approximately represented by $\delta = 1/(2\alpha)$, where α is the absorption coefficient. As shown in Figure 2.6, a typical value δ = 2 mm for laser with a wavelength of 532nm (corresponding to 2.5 eV) was obtained[19], which means that the resolution in the direction perpendicular to the SiO_2/SiC interface is shallow. This is resulting in that most of the detected Raman signals collected from the SiC bulk rather than the interface of SiO_2/SiC.

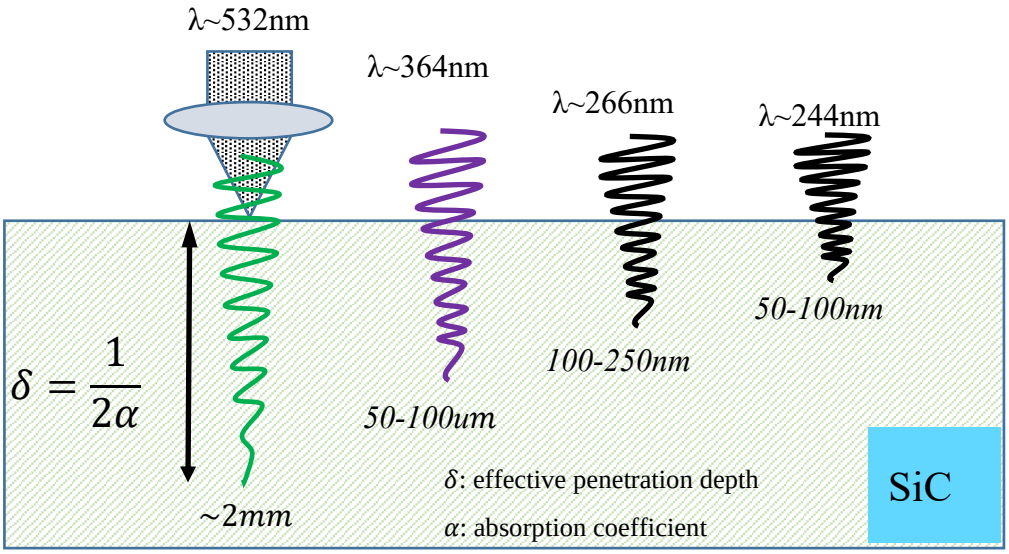

Figure 2.6 Penetration depth of incident light with different wavelengths in 4H-SiC

As we know, all confocal imaging techniques, for example, confocal Raman microscopy, are based on a point-to-point image formation. A detailed overview of these methods can be found in [20]. Confocal microscopy techniques can increase depth resolution by adding a spatial pinhole in front of the detector to eliminate the scattered light out of the focal plane[13]. As can be seen in Figure 2.7, those that are not from the focal plane cannot pass through the pinhole. With this simple geometric representation, image resolution can be greatly enhanced.

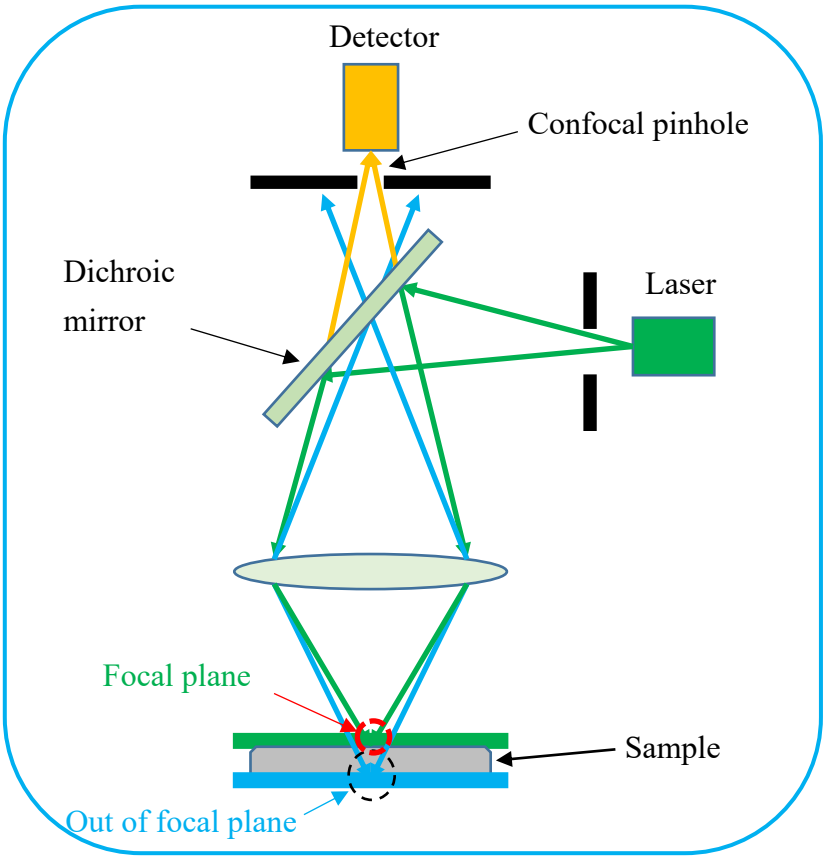

Figure 2.7 Principal setup of a confocal microscope

In addition, based on Eqs. (2.11) and (2.12), as shown in Figure 2.8, the spatial extension of the focus spot on the sample is determined by the wavelength λ and the pinhole size, here the constants A and B decrease as the diameter of the pinhole. In the confocal microscope system, the focal waist diameter corresponds to the resolution of the system in the x and y direction (d_{xy}), and the thickness of the confocal slice corresponds to the resolution of the system in the z-direction (d_z). We can see that when the wavelength of the incident light and the number of apertures (NA) remain as constants. Thus, we can improve the resolution of the system by reducing the pinhole value. However, it should be noted here that a smaller pinhole value means that more reflected light is eliminated, and as a result, the intensity of the signal collected by the detector becomes weaker. Therefore, in this system, it is essential to find the balance of high optical resolution and

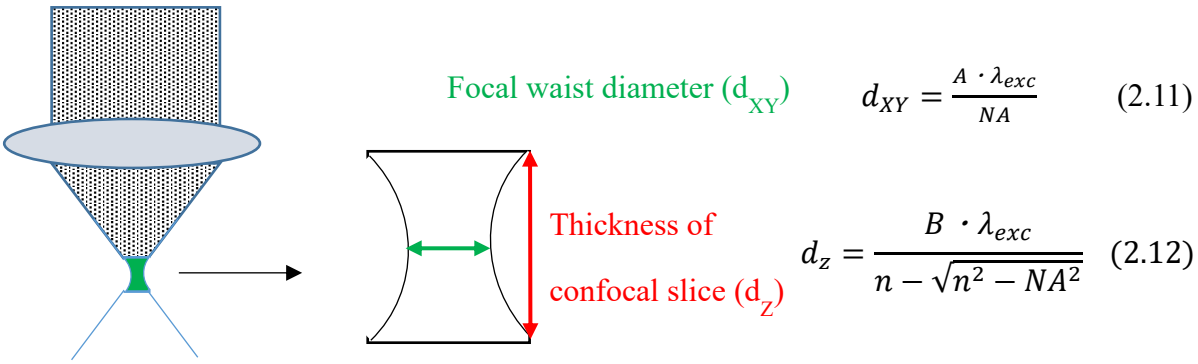

Figure 2.8 Optical resolution of confocal Raman microscope system.

vigorous signal intensity.

By introducing the confocal microscopy system into Raman measurement, it is possible to investigate the stress distribution at the SiO_2/4H-SiC interface directly. In this chapter, we first discuss the method of measuring biaxial stress distribution at the SiO_2/4H-SiC interface by confocal Raman microscopy technique. Then, we carried out the measurement to the different NO POA treated samples and calculated the stress at the SiO_2/4H-SiC interface based on the measured value. Using these results, we investigated the relationship between the passivation of NO POA treatment and the defect due to the stress at the SiO_2/4H-SiC interface.

2.3 Experimental

We performed confocal Raman microscopy measurement by using a Raman microscopy system equipped with laser scanning confocal microscopy and combined with a spectrometer. It is capable of measuring a microscopic scale with a

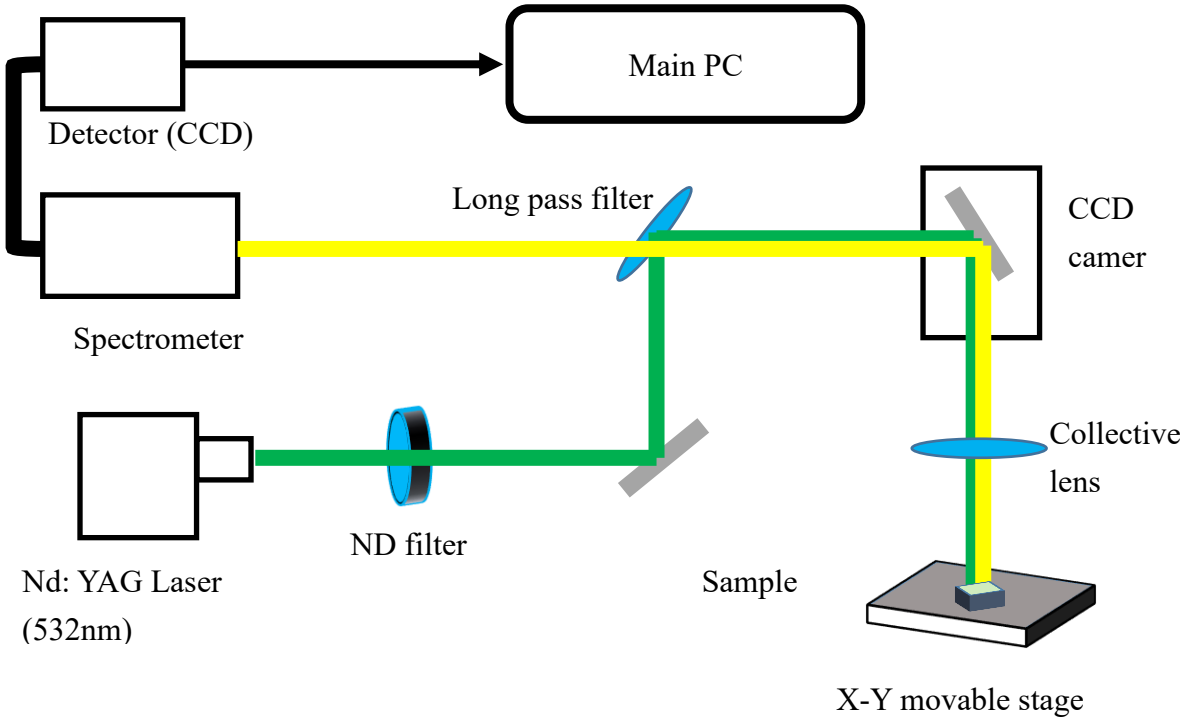

Figure 2.9 Basic setup for confocal Raman microscopy

spatial resolution. The 532 nm laser with 10 mW power was used as the incident light. To approach the best spatial resolution, a 100× objective lens with a numerical aperture (NA) of 0.95 was used in the measurements. As a comparison, an objective lens with NA=0.6 was used. The diameter of the confocal pinhole is 100 um. The detector is a cooled-type charge-coupled device (CCD; Andor Inc.), which is utilized to gather the optical phonon frequencies in the backscattering geometry. The calibration of the confocal Raman system was done by measuring a silicon wafer (with a characteristic peak of 520 cm^{-1}).

The SiO_2/ SiC samples were fabricated by a dry oxidation process of oxidizing 4H-SiC (0001: Si-face) at 1200 ℃, 50 nm thick SiO_2 films were grown on 4H-SiC. Then, a post-annealing in nitric oxide ambient was carried out at 1250 ℃ for 0, 10, 60, 120 min. As a comparison, SiO_2/ Si samples were fabricated by a dry oxidation process in O_2 atmosphere in Si (001) substrate treatment at 800℃ and 900℃ respectively, without any POA After that, the thickness of the SiO_2 films were altered by chemical etching with an HF aqueous solution, and the thickness of the remaining SiO_2 film was

determined by the ellipsometry to be 50, 40, 30, 20,10 and 0 nm. The Confocal Raman spectroscopy measurement data were collected while the SiO_2 film was sequentially etched on 4H-SiC. The Raman shift was gathered from six different points at every thickness of the SiO_2 layer in each sample to eliminate the measurement error. The calibrations were performed at every thickness alteration. It should be noted that the calibration process is fundamental in this measurement system.

The Lorentzian function was used in fitting the Raman spectrum curve to determine the Raman peak position. As mentioned before, the 4H-SiC polytype is a type of the C_{6v}^4 the space group. In the long-wavelength limit, the normal vibrational modes are $4(A_1+B_1+E_1+E_2)$. Among them, Raman active E_2 modes are planar modes[14, 15]. Since the origin

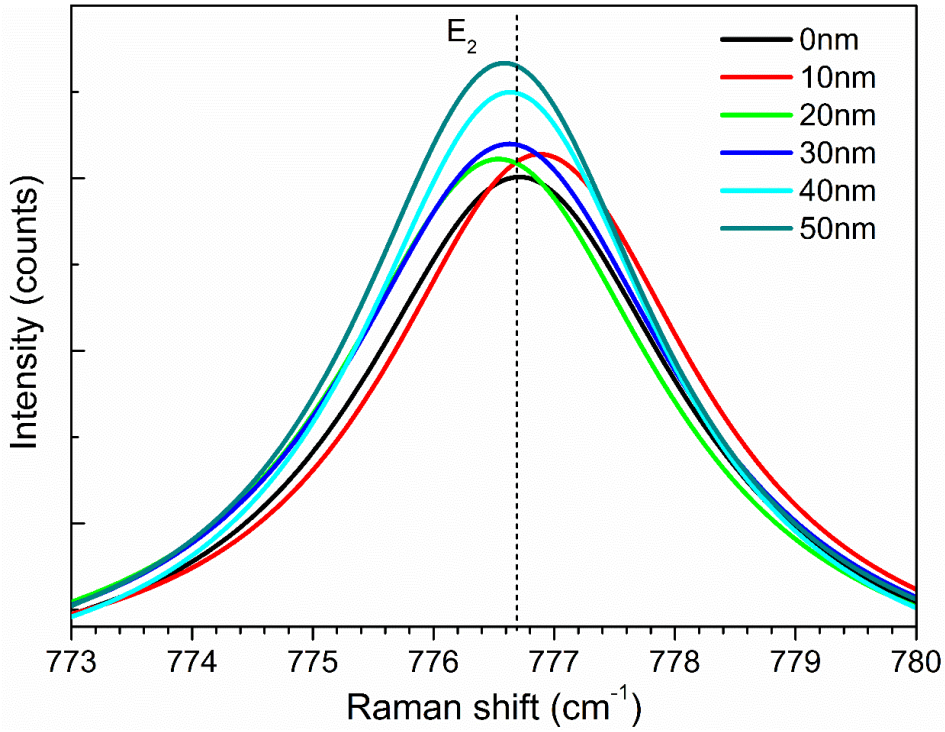

Figure 2.10 (a) Raman spectra near the FTO E_2 mode, correspond to the residual SiO_2 layers of different thicknesses on the SiC substrate. Raman spectra were gathered using an NA = 0.95 objective.

of interfacial stress in the SiO_2/4H-SiC system was considered as (1) the different thermal expansion between the SiC substrate and the SiO_2 oxide film, and (2) the lattice mismatch between the 4H-SiC and SiO_2 film, this system is regarded as one with biaxial stress in the films[21]. According to the above reasons, only the peak mode of FTO E_2 (around 776 cm^{-1}) was carefully analyzed in our measurement, due to its nonpolar origin. Furthermore, the FTO E_2 is widely used to quantify the biaxial stress in wurtzite semiconductors[22, 23].

2.4 Results and discussion

2.4.1 Confocal Raman microscopy techniques on SiO_2 residual thickness

2.4.1.1 Stress at SiO_2/4H-SiC interface

The confocal Raman measurements were firstly carried out using NA 0.95 objective lens on the samples, which were annealed for 60 min in NO atmosphere. Figure 1(a) displays the Raman spectra near the FTO E_2 mode, correspond to the residual SiO_2 layers with different thicknesses on the SiC substrate. We defined the sample without SiO_2 (i.e., the SiO_2 layer on the SiC substrate was removed entirely) as a relaxed reference sample. The shift of Raman peak position was observed on the samples with different thickness of SiO_2 layers. Note that to eliminate the measurement error, the Raman measurements were carried out on six different locations at every thickness of SiO_2 layers, as shown in Figure 2.10 (a). The dependence of Raman peak shift on SiO_2 in the function of the remaining thickness is summarized in Figure 2.10 (b). The stress generation, which was reflected by Raman peak shift, was observed in the samples with SiO_2 thickness above 10 nm. Moreover, we found a clear trend that for thinner SiO_2 thickness, the peak shift becomes more pronounced. This agrees with the stress distribution, as previously reported[11, 24]. However, the stress in remaining SiO_2 with a thickness

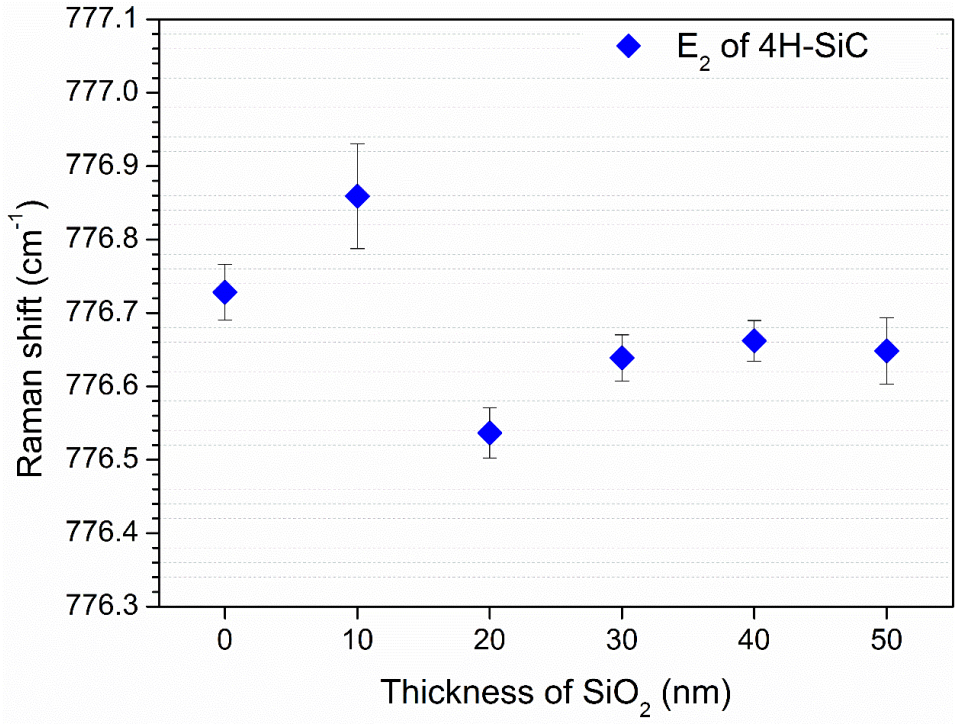

Figure 2.10 (b) Measured Raman peak shift as a function of residual SiO_2 thickness on SiC substrate

of around 10 nm exhibited abnormal behavior, and we will discuss it later in detail.

After verifying the existence of the stress in the SiO_2/SiC system, we need to confirm that the measured stress is distributed near the interface. Therefore, two types of objective lenses with NA = 0.95 and NA = 0.6 were utilized. Since the spatial resolution of the confocal microscope system can be distinguished between NA = 0.95 and NA = 0.6. Based on the equation (2.12), the spatial resolution (i.e., the diameter of the focused laser beam) d is calculated for λexc = 532 nm. We obtain $d_{NA0.95} \approx 0.42$ um and $d_{NA0.60} \approx 1.46$ um (d: nominal focus position). Then, taking into account the Snell`s

law and the reflection index of 2.65 for SiC at 532 nm[25], and use a theoretical depth compression factor D/d of 3.735[26] (D: actual focus position), the actual spatial resolution of 1.56 and 5.4 um are achieved for NA 0.95 and NA 0,60 objective lenses, respectively.

Table 2.1 Values of the nominal and actual spatial resolution.

Objective lens	Nominal Spatial Resolution d(um)	Actual Spatial Resolution D(um)
NA 0.95	0.42	1.56
NA 0.6	1.46	5.4

Purporting that the Raman signal gathers from the bulk of SiC can be detected by the NA 0.6 lens, while the NA 0.95 lens can detect the Raman signal near the surface of SiC. The dependence of the Raman peak shift on SiO_2 residual thickness is shown in Figure 2.11. Compared with the results detected by using the NA 0.95 lens, the same Raman peak shift trend was not observed by using NA 0.6 objective, indicating that the stress distribution only occurs close to the interface of SiO_2/4H-SiC.

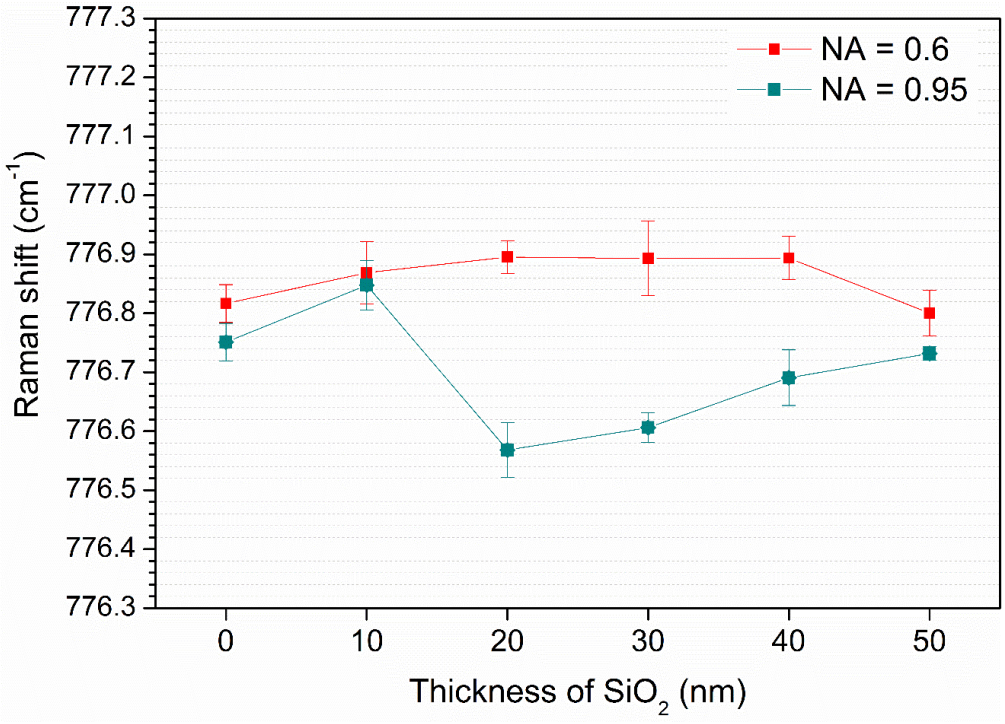

Figure 2.11 Raman peak positions measured from 120 min NO POA treated samples using objectives with NA = 0.6 and NA = 0.95.

2.4.1.2 Stress in SiO_2/Si interface

We measured the strain for the samples with different thickness of the SiO_2 layer based on the Raman peak shift. We need to clarify whether or not the chemical thinning of SiO_2 films induces optical alteration that could affect this kind of peak shift. We carried out the same measurement for the SiO_2/Si sample. The SiO_2 layer of Si-MOS samples has the same initial thickness as it on the SiC-MOS samples, and we etched the samples by using the same steps as before. The

differences of the Si atom density and the thermal expansion between Si and SiO_2 are similar to those between SiC and SiO_2[10]. Nevertheless, due to the lower temperature for fabricating SiO_2/Si compared to the SiO_2/SiC system, the thermal strain induced by temperature variation at SiO_2/Si interface (grown at 800 ℃) should be smaller than that of SiC. For SiO_2/Si samples grown at 900℃, since the viscoelastic phenomenon of the thermal oxide film was introduced[27], resulting in stress relaxation, the strain at 900 ℃ should be even smaller than that of 800 ℃. As a result, the Raman peak shift should be difficult to be observed by using our measurement system. As shown in Fig 2.12, the same Raman peak shift trend was not observed at the SiO_2/Si interface. Based on these results, we could conclude that the chemical thinning of SiO_2 films does not induce any modification on the stress.

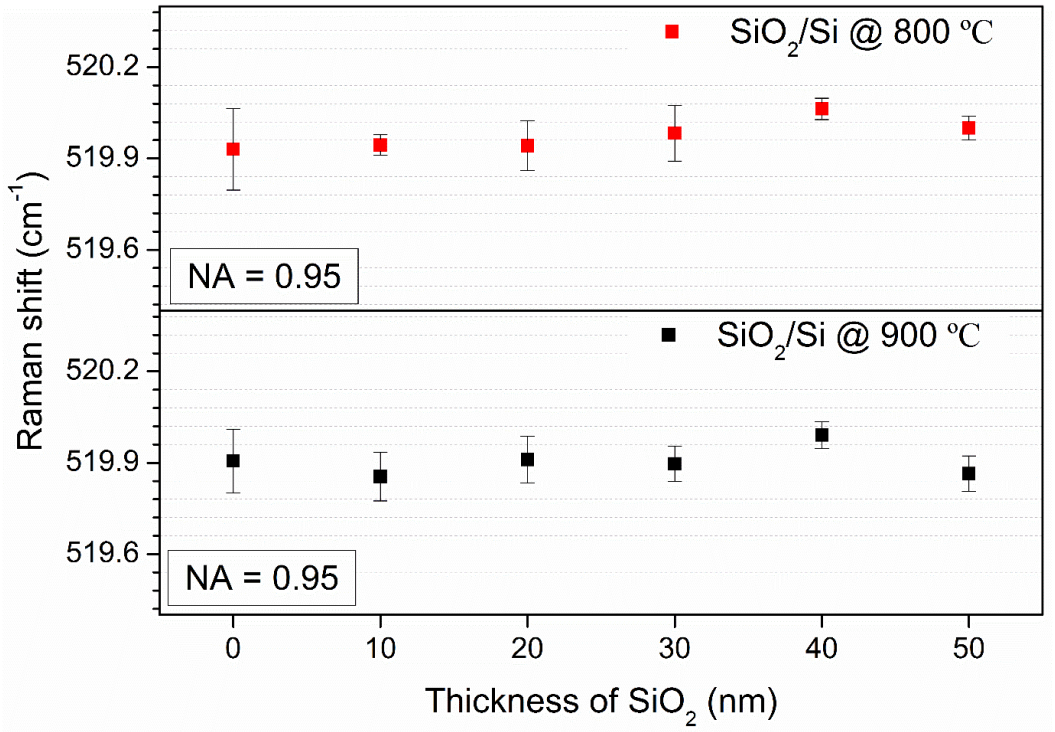

Figure. 2.12. Raman peak shift dependent on residual SiO_2 thickness in the Si/SiO_2 system. The Raman peak shifts in samples oxidized at 800 °C and 900 °C were measured using an NA = 0.95 objective.

2.4.2 Confocal Raman microscopy techniques on NO POA samples

We performed the confocal Raman microscopy measurement on the post-oxidation annealed samples, which processed by interfacial nitridation in NO gas at 1250℃ for 0, 10, 60, and 120 min. The relationship between the Raman peak shift and the thickness of the remaining SiO_2 layer for the four types of samples is summarized in Fig. 2.13. We observed the same peak shift trend in all samples in the analysis area near the interface. The trend of the stress distribution was considered after the SiO_2 layer was grown on SiC substrate at high-temperature. On the one hand, compared to SiC, the molecular volume of SiO2 is much more abundant; on the other hand, the thermal expansion coefficient of SiC is much larger than that of SiO2. Thus, during the cooling procedure of high-temperature thermal oxidation, SiC shrinks much more than SiO_2. Therefore, the SiO_2 film on the SiC substrate bends into a spherical bowl shape. This results in the generation of biaxial tension are in the surface of the SiC substrate, while biaxial compression in the SiO_2 films on the SiC substrate surface. Thus, the Raman peak shifting to a lower or higher frequency than this the Raman peak of SiC samples without SiO_2 layers, taken as stress-relaxed reference, may be proportional to compressive and tensile stress.

In our measurement, the generation of tension stresses located on the SiC side of the SiO2/SiC interface ware observed

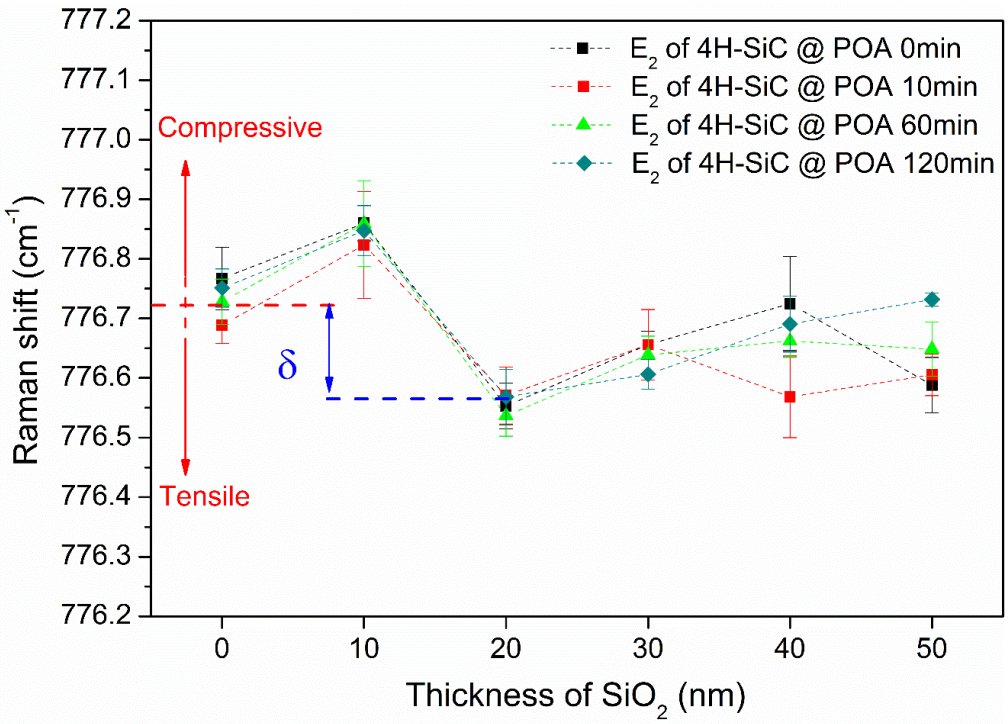

Figure 2.13. Relationship between the Raman peak shift and the thickness of the remaining SiO_2 layer for the four types of samples, treated using NO POA for 0, 10, 60, and 120 min.

in samples with the remaining SiO_2 thickness of above 10 nm, which is in good agreement with the physical phenomena described before. Attractively, only the stress observed in the residual SiO_2 layer of thickness around 10 nm exhibits the abnormal behavior, with a Raman peak shifting to the higher frequency than one of the stress-free references, which is opposite to the stress-induced shift for SiO_2 layer thicker than above 20 nm. It can be considered that due to the compressive stress generated at the SiO_2/SiC interface, a silicon suboxide component is generated, and the Si-O bonds are weakened. As a result, oxygen becomes insufficient in relaxing the compressive stress in the oxide close to the interface[8], at the same time, tensile stress relaxes at the surface of the SiC substrate.

2.4.3 Interface stress calculation.

Based on the above analysis, we can calculate the stress at the SiO_2/SiC interface using the measured Raman peak shift. In our experiment, the confocal Raman microscopy measurements were carried out in the straightforward backscattering geometry, perpendicular to the interface of SiO_2/4H-SiC. The polarization of the incident light was perpendicular to the c axis of samples. Fig. 2.14 shows the Raman measurement configuration used in our experiment. For the calculation, the Raman peak shift obtained in the samples with 20 nm SiO_2 was selected as δ_ω. The typical Raman spectrum for 20 nm SiO_2 on SiC, compared with the spectrum for stress-relaxed SiC substrate, is shown in Fig. 2.15. The measured strain for FTO E_2 peak shift δω can be transformed into biaxial stress σ_B based on the following expression[28]:

$$K_B\left(\frac{cm^{-1}}{Pa}\right) = \frac{\delta_\omega}{\sigma_B} = -2\alpha(S11 + S12) - 2bS13, \text{ (2.13)}$$

Equation (2.13) can be represented as a solution for the biaxial-stress:

$$\sigma_B = \frac{\delta_\omega}{\{-2\alpha(S11+S12)-2bS13\}}, \text{ (2.14)}$$

where {Sij} are compliance constants, given in Refs[29-31]. As: S11 = 2.03 GPa^{-1}, S12 = -0,421 GPa^{-1}, and S13 = -0,189 GPa^{-1}; σ is the positive biaxial tensile stress, δ is the changing of the frequency shift of FTO E_2 peak, The deformation potentials a = b = -800/cm was deduced. The stress σ at the interface of SiO_2/SiC for the four types of samples

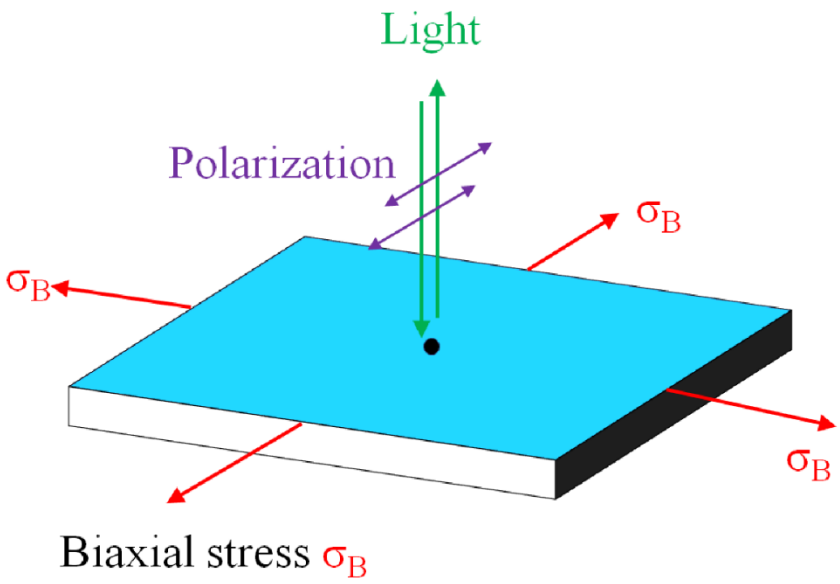

Figure 2.14. Raman measurement configuration for gaining the biaxial stress on the SiC substrate surface.

was calculated by using Eq. (2.14) based on the measured peak shift δ. As a comparison, we use the relationship between Raman displacement and interface stress obtained from experimental values [32] to verify our calculations. According to this, the following equation is derived:

$$\delta_\omega(cm^{-1}) = -1.96 \times \sigma(\text{GPa}), \text{ (2.15)}$$

The calculated stress values σ_B in this work, σ_1 obtained based on equation (2.15) and σ_2 got from the literature[24] are shown in Table 2.2. The calculated interfacial stress values in our experiment are close to the values calculated by using Eq. (2.15). They are, however, differ greatly from the reported stress values in Ref 24 measured in the SiO_2 layer. This difference may come from the alteration of the stress value at the SiC surface and in the SiO_2 layer. Since the stress describes the strength of the interaction forces applied by neighboring particles of a continuous media apply on to each other, due to there is a complex and interesting structure layer close the interface, The stress value directly measured with the SiC surface should not be completely equal to the stress measured in the SiO_2 film, its value can vary a lot between the two materials. Furthermore, the interface stresses were calculated on the four kinds of NO treated samples. The

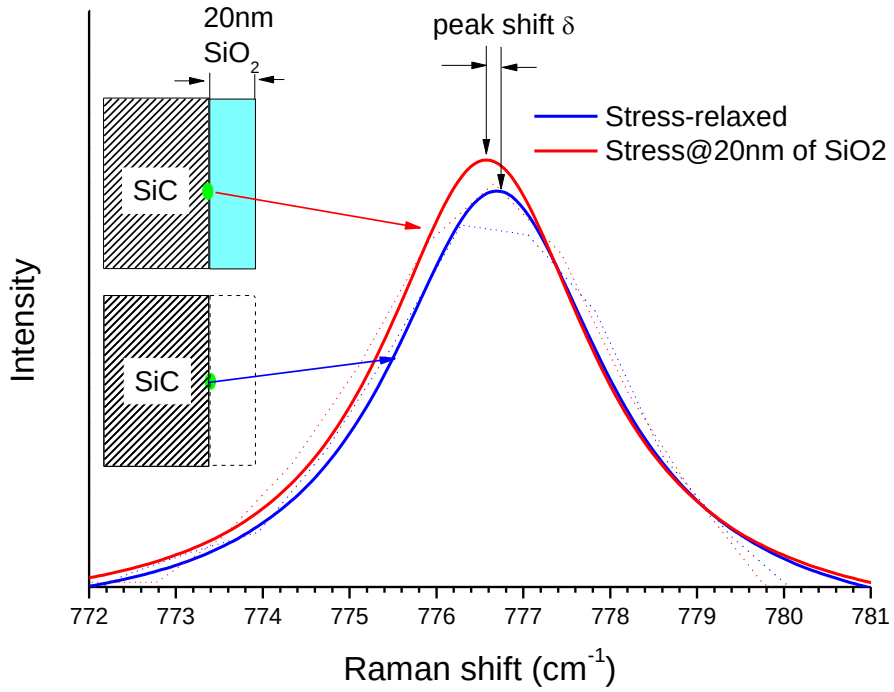

Figure 2.15 Typical Raman spectrum from a stress-relaxed SiC substrate compared with that of SiC substrate with residual SiO_2 thickness of 20 nm.

interfacial stress values corresponding to the NO annealing time are summarized in Figure 2,16. Since the calculated stresses have similar values for different annealing time, we cannot find clear evidence that NO post-annealing has an effect on the relaxation of stress at the SiO_2/SiC interface. It implies that NO post-annealing is not effective in the passivation of the defects due to the strain generation at the interface of SiO_2/4H-SiC.

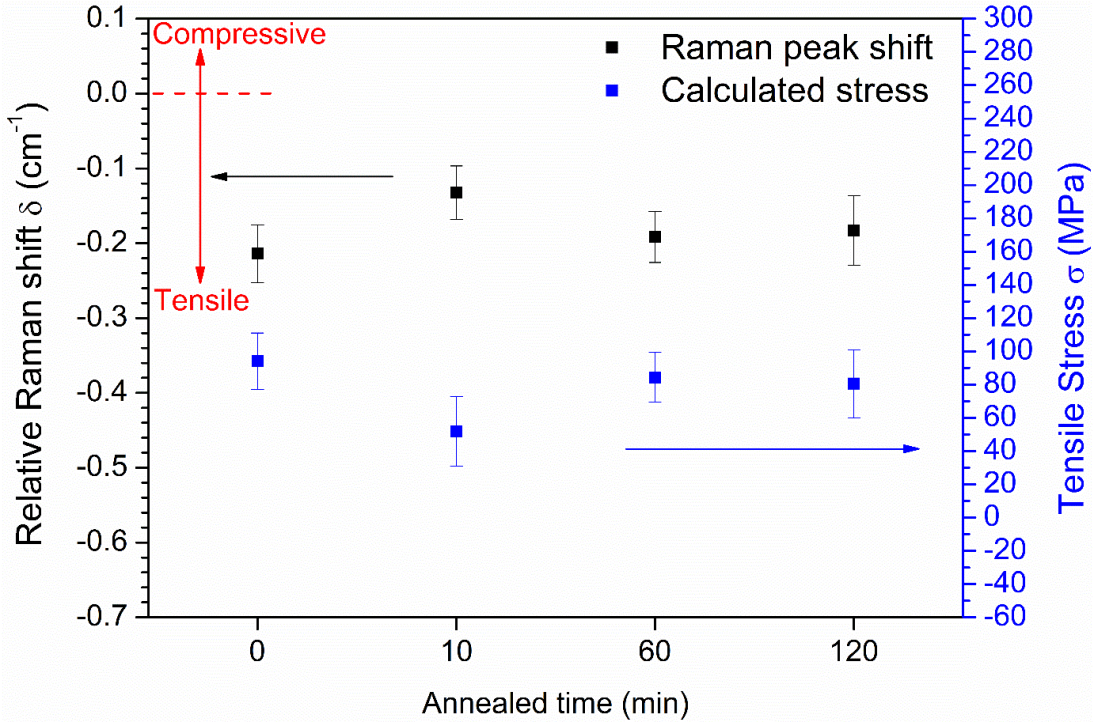

Figure 2.16 Interfacial stress values corresponding to the NO annealing time.

Table 2.2. Calculated stress values in this work σ_B; the stress values were calculated using Eq. (2.15) in Ref. 32 σ_B and the stress σ_2 obtained from Ref. 24.

Stress σ (MPa)	POA-0 min	POA-10 min	POA-60 min	POA-120 min
σ_B (in this work)	94.12	51.89	84.30	80.54
σ_1 (based on Eq. 2.15)	109.16	60.15	97.72	93.36
σ_2 (in Ref 24)	250-350	-	-	-

2.5. Summary

In this work, we investigated the stress distribution at the interface of SiO_2/4H-SiC using confocal Raman microscopy technique. The residual strain was found in the HF etched samples with a SiO_2 layer of at least 10 nm. There is a clear trend toward a more substantial peak shift for smaller SiO_2 thickness. The stress σ based on the peak shift δ was also calculated. Using these results, we evaluated the relationship between the calculated stress σ and POA time in NO gas. Since the computed stress for different annealing time has similar values, we cannot find clear evidence that NO post-annealing has an effect on the relaxation of stress at the SiO_2/4H-SiC interface. It implies that the NO post-annealing system does not efficiently passivate the defect induced by the strain generated at the interface of SiO_2/4H-SiC.

Fundamental study on carrier scattering mechanism plays an important role in the understanding of the relationship between the defect in the SiC-side and the carrier transport characteristics in the inversion layer of SiC-MOSFETs. The stress at the SiO_2/4H-SiC interface was precisely analyzed in this work. Moreover, it has been shown that the carrier transport properties change caused by the mass shift or/and scattering rate variation induced by stress[33]. Therefore, in future works, we will do the calculation of carrier mobility under stress by introducing the strain Hamiltonian into Fermi golden rule and Boltzmann transport equation based on the deformation potential theory and phonon scattering mechanism[34], to find out how the stress at the interface effect on the electron mobility in the inversion layer of SiC-MOSFETs.

2.6. Next step work

Although NO annealing is currently the most effective method for reducing interface defects, it has no significant effect on the release of interfacial stress. It is known that the interface stress-induced lattice distortion may affect the electron mobility in two possible ways: 1) generation of the deformation potential; 2) formation of interface defects. In order to confirm how to interface stress affects the electron mobility, in the next step, we will evaluate the relationship between the interfacial strain and the electromobility using the theoretical calculation.

2.7 Reference

[1] A. Poggi, F. Moscatelli, S. Solmi, A. Armigliato, L. Belsito, R. Nipoti, Effect of nitrogen implantation at the SiO2/SiC interface on the electron mobility and free carrier density in 4H-SiC metal oxide semiconductor field effect transistor channel, Journal of Applied Physics, 107 (2010) 044506.

[2] L. Hui-Feng, S. Dimitrijev, H.B. Harrison, Improved reliability of NO-nitrided SiO2 grown on p-type 4H-SiC, IEEE Electron Device Letters, 19 (1998) 279-281.

[3] G.Y. Chung, C.C. Tin, J.R. Williams, K. McDonald, M. Di Ventra, S.T. Pantelides, L.C. Feldman, R.A. Weller, Effect of nitric oxide annealing on the interface trap densities near the band edges in the 4H polytype of silicon carbide, Applied Physics Letters, 76 (2000) 1713-1715.

[4] P. Deak, J. Knaup, C. Thill, T. Frauenheim, T. Hornos, A. Gali, The mechanism of defect creation and passivation at the SiC/SiO2 interface (vol 40, pg 6242, 2007), J Phys D Appl Phys, 41 (2008) 049801.

[5] G.Y. Chung, J.R. Williams, K. McDonald, L.C. Feldman, 4H-SiC oxynitridation for generation of insulating layers, J Phys-Condens Mat, 16 (2004) S1857-S1871.

[6] G.Y. Chung, C.C. Tin, J.R. Williams, K. McDonald, R.K. Chanana, R.A. Weller, S.T. Pantelides, L.C. Feldman, O.W. Holland, M.K. Das, J.W. Palmour, Improved inversion channel mobility for 4H-SiC MOSFETs following high temperature anneals in nitric oxide, Ieee Electron Device Letters, 22 (2001) 176-178.

[7] Y. Wang, K. Tang, T. Khan, M.K. Balasubramanian, H. Naik, W. Wang, T.P. Chow, The effect of gate oxide processes on the performance of 4H-SiC MOSFETs and gate-controlled diodes, Ieee Transactions on Electron Devices, 55 (2008) 2046-2053.

[8] H. Seki, M. Yoshikawa, T. Kobayashi, T. Kimoto, Y. Ozaki, Characterization of Thermal Oxides on 4H-SiC Epitaxial Substrates Using Fourier-Transform Infrared Spectroscopy, Applied Spectroscopy, 71 (2017) 911-918.

[9] T.C. Yang, K.C. Saraswat, Effect of physical stress on the degradation of thin SiO/sub 2/ films under electrical stress, IEEE Transactions on Electron Devices, 47 (2000) 746-755.

[10] K. Tu, J. Mayer, L. Feldman, Electronic Thin Film Science for Electrical Engineers and Material Scientists, 1992, in, New York: Macmillan Publishing Company.

[11] E. Kobeda, E.A. Irene, Intrinsic Sio2 Film Stress Measurements on Thermally Oxidized Si, J Vac Sci Technol B, 5 (1987) 15-19.

[12] E. Kobeda, In situ stress measurements during thermal oxidation of silicon, Journal of Vacuum Science & Technology B: Microelectronics and Nanometer Structures, 7 (1989) 163-166.

[13] T. Dieing, O. Hollricher, J. Toporski, Confocal raman microscopy, Springer, 2011.

[14] R. Sugie, T. Uchida, Determination of stress components in 4H-SiC power devices via Raman spectroscopy, Journal of Applied Physics, 122 (2017) 195703.

[15] S. Nakashima, H. Harima, Raman investigation of SiC polytypes, Phys Status Solidi A, 162 (1997) 39-64.

[16] T. Dn, W. L, T. Cc, F. Zc, Assessing Biaxial Stress and Strain in 3C-SiC/Si (001) by Raman Scattering Spectroscopy, Journal of Material Science & Engineering, 06 (2017) 324.

[17] H. Sakakima, S. Takamoto, Y. Murakami, A. Hatano, A. Goryu, K. Hirohata, S. Izumi, Development of a method to evaluate the stress distribution in 4H-SiC power devices, Japanese Journal of Applied Physics, 57 (2018) 106602.

[18] S. Rohmfeld, M. Hundhausen, L. Ley, C.A. Zorman, M. Mehregany, Quantitative evaluation of biaxial strain in epitaxial 3C-SiC layers on Si(100) substrates by Raman spectroscopy, Journal of Applied Physics, 91 (2002) 1113-1117.

[19] H. Harima, Raman scattering characterization on SiC, Microelectronic Engineering, 83 (2006) 126-129.

[20] J. Pawley, J.J.H.o.b.c.m. Pawley, 2nd edn. Plenum Press, New York, Appendix 2: light paths of current commercial confocal light microscopes for biology, (1995) 581-598.

[21] D.N. Talwar, L. Wan, C.-C. Tin, Z.C.J.J.M.S.E. Feng, Assessing biaxial stress and strain in 3C-SiC/Si (001) by Raman scattering spectroscopy, 6 (2017) 324.

[22] H.J. Trodahl, F. Martin, P. Muralt, N. Setter, Raman spectroscopy of sputtered AlN films: E-2(high) biaxial strain dependence, Applied Physics Letters, 89 (2006) 061905.

[23] M. Azize, T. Palacios, Effect of substrate-induced strain in the transport properties of AlGaN/GaN heterostructures, Journal of Applied Physics, 108 (2010) 023707.

[24] X.Y. Li, A. Ermakov, V. Amarasinghe, E. Garfunkel, T. Gustafsson, L.C. Feldman, Oxidation induced stress in SiO2/SiC structures, Applied Physics Letters, 110 (2017) 141604.

[25] P.T. Shaffer, Refractive index, dispersion, and birefringence of silicon carbide polytypes, Appl Opt, 10 (1971) 1034-1036.

[26] W.L. Chen, Y.Y. Lee, C.Y. Chang, H.M. Huang, T.C. Lu, Y.M. Chang, Depth-resolved confocal micro-Raman spectroscopy for characterizing GaN-based light emitting diode structures, Rev Sci Instrum, 84 (2013) 113108.

[27] B. Mrstik, A. Revesz, M. Ancona, H.J.J.o.t.E.S. Hughes, Structural and Strain-Related Effects during Growth of SiO2 Films on Silicon, Journal of The Electrochemical Society, 134 (1987) 2020-2027.

[28] F. Demangeot, J. Frandon, P. Baules, F. Natali, F. Semond, J. Massies, Phonon deformation potentials in hexagonal GaN, Physical Review B, 69 (2004) 155215.

[29] G. Arlt, G.R. Schodder, Some Elastic Constants of Silicon Carbide, J Acoust Soc Am, 37 (1965) 384-&.

[30] S. Karmann, R. Helbig, R.A. Stein, Piezoelectric properties and elastic constants of 4H and 6H SiC at temperatures 4–320 K, Journal of Applied Physics, 66 (1989) 3922-3924.

[31] K.B. Tolpygo, Optical, Elastic and Piezoelectric Properties of Ionic and Valence Crystals with the Zns Type Lattice, Sov Phys-Sol State, 2 (1961) 2367-2376.

[32] N. Sugiyama, M. Yamada, Y. Urakami, M. Kobayashi, T. Masuda, K. Nishikawa, F. Hirose, S. Onda, Correlation of Stress in Silicon Carbide Crystal and Frequency Shift in Micro-Raman Spectroscopy, MRS Proceedings, 1693 (2014).

[33] Y. Sun, S.E. Thompson, T. Nishida, Strain effect in semiconductors: theory and device applications, Springer Science & Business Media, 2009.

[34] Y. Peter, M. Cardona, Fundamentals of semiconductors: physics and materials properties, Springer Science & Business Media, 2010.

Chapter 3 The effect of biaxial stress on the carrier-transport properties at SiO_2/4H-SiC interfaces

3.1 Introduction

Because strain may be the cause of significant changes in the electrical properties of semiconductors, strains in semiconductors have been one of the topics of research for decades.[1]. In electrical equipment, in order to achieve individual engineering goals, strained semiconductors may inadvertently appear, or strains may be introduced[2]. In silicon-MOSFETs, strain engineering has been commonly utilized to improve electron transport properties in highly scaled devices[3-5]. However, so far, in SiC-MOSFETs, strain engineering has not been able to improve the electronic transmission performance effectively. Recently, first-principles calculation studies have advised that the compressive strain induced by high-temperature thermal oxidation leads to the formation of an interface state, due to the local alteration in conduction band energy[6, 7]. Furthermore, the interfacial stress on the SiO_2 oxide film side was evaluated by Li et al.[8] In our previous study, we measured and calculated the stress on the SiC side of the SiO_2/4H-SiC interface caused by thermal oxidation.[9]. However, the physics underlying the interface stress as a factor affecting the electron mobility is still unknown. Therefore, to understand the relationship between the strain at the SiC surface and the carrier transport properties in the inversion layer of SiC-MOSFETs, we need to perform a fundamental study of the carrier scattering mechanism.

It is known that strain-induced stress of the lattice usually causes a modification of the effective mass and/or variations of the scattering rate, which affects the carrier transport.[10] However, the relationship between the biaxial stress at the SiO_2/4H-SiC interface and the electron mobility is still unclear. Moreover, owing to the potential disturbances induced by the lattice vibration, the stress-induced electron transport is mainly limited by phonon scattering.[11] Thus, in this work, we studied the phonon-limited electron mobility limited by the acoustic and optical phonon scattering using the standard scattering model. Additionally, we described the calculation process mainly and analyzed the calculation results in detail. Moreover, we also explain the relationship between the actual interfacial stress and our calculation results.

It is worth noting that the properties of the semiconductor surface are sufficiently different from the features of the semiconductor bulk. However, a study of semiconductor surface properties depends on an understanding of the bulk properties of the semiconductor. Therefore, the research and understanding of bulk properties had to precede the study of surface properties. Thus, in this work, we first studied the phonon-limited three-dimensional electron mobility limited by the acoustic and optical phonon scattering using the standard bulk scattering model. Then, the two-dimensional electron mobility calculation corresponding to the channel mobility was carried out to a more accurate evaluation of the relationship between the biaxial stress and the carrier-transport properties at SiO_2/4H-SiC interfaces.

3.2 Theoretical background

Usually, the state transitions are analyzed using the Schrodinger equation, which forms the basis of quantum mechanics. To the practical understanding of how carriers move in the crystalline materials, the transition probability is calculated from the approximate solution by perturbation theory based on an explicit mathematical method. As we knew, in a perfective crystal, the description of the behavior of an electron in the periodic material must be via the Schrodinger

equation

$$H_0\psi(\vec{r}) = E\psi(\vec{r}),$$

$$H_0 = \frac{-\hbar^2}{2m_0}\nabla^2 + U(\vec{r}), \qquad (3.1)$$

Where $U(\vec{r})$ is the background potential seen by the electron. Due to the crystalline nature of the material, the potential $U(\vec{r}) = U(\vec{r} + \vec{R})$ has the same periodicity, R, as the lattice. However, in the strained crystal case, strain in the crystal is created by deformation and is defined as relative lattice displacement, which changed the background potential as a perturbed element. Thus, the strain can be just considered as an extra coupling term H_1, which is directly added to the unperturbed Hamiltonian, therefore, the Schrodinger equation can be represented as

$$(H_0 + H_1)\psi(\vec{r}) = E\psi(\vec{r}) \qquad (3.2)$$

Then, based on the deformation potential theory, which developed to characterize the band energy shift with strain caused by phonons, it can be used to model lattice scattering[12]. The electron encounters a perturbation caused when a lattice vibration moves an atom, which may be present. When an electron encounters such a perturbation, it will scatter an electron wave packet centered at *k* to *k`*. Frequent scattering tends to the introduction of the interference effects due to the carrier`s wave nature. Scattering plays a dominant role in transport, and we must know *S (k, k`)*, the transition rate from $k$ to $k`$. Fermi`s golden rule is a method to calculate the transition rate from $k$ to *k`* due to a perturbation[13]. Here we present the expression for the transition probability $S(k,\ k`)$ in terms of H_1, the perturbing potential.

$$S(k_0, k_0`) = \frac{2\pi}{\hbar}\left|\langle k`|H_1|k\rangle\right|^2\delta\left[E(k`) - E(k) \mp \hbar\omega\right] \qquad (3.3)$$

The energy exchange between the electrons and the lattice occurs via phonons, and the delta distribution ensures energy conservation. Here, $\hbar\omega$ is the energy of the absorbed or emitted phonons.

To characterize the transport characteristics of the electron gas, we need to know the distribution function of the electron gas. We know that at equilibrium, the distribution function is simply the Fermi-Dirac function. However, in the presence of external forces, we need to employ the Boltzmann transport equation to describe the distribution function, not in a state of equilibrium. The comparison can be written as[14]

$$\frac{df}{dt} + \frac{P}{m}\cdot\nabla f + F\cdot\frac{\partial f}{\partial P} = \left(\frac{\partial f}{\partial t}\right)_{coll} \qquad (3.4)$$

Where *F* is the force field acting on the particles in the fluid, *m* is the mass of the particles, *P* is the momentum of the particles, and the "coll" is the collision term, which means that the force acting between the particles in collisions. Theoretically, based on the transition probability $S(k,\ k`)$, which appears in the collision term of the Boltzmann transport equation, we can characterize the carrier transport properties by solving the Boltzmann transport equation in the relaxation time approximation. In the following sections, we apply the above method to evaluate how electron mobility in 4H-SiC

crystals is affected by stress.

3.2.1 Phonon scattering mechanism for 3D carriers

When stress is applied to a substance, the distance between atoms changes, thereby causing the bonding force changes, at this time, the frequency of the lattice vibration changed. In general, we use quantum mechanical descriptions of vibrations to resolve the interaction of electrons with perturbation potentials generated by lattice vibrations. In this description, vibrations are thought to excite phonons similar to the picture of an electromagnetic wave. These phonons are regarded as particles and their interaction with the electrons following the principles of conservation of energy and

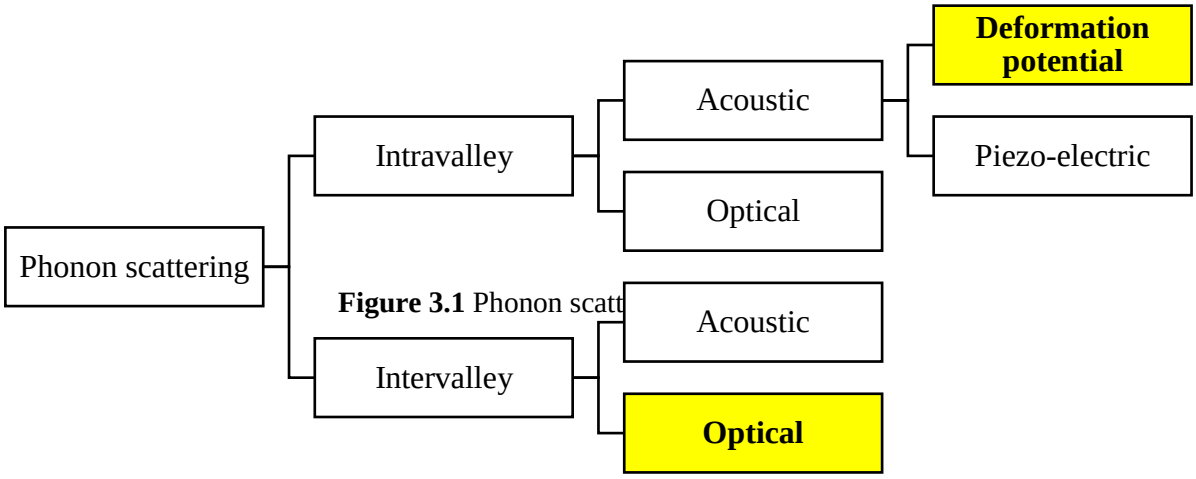

Figure 3.1 Phonon scatt

momentum. The band structure of a solid material depends on the location of each atom in the lattice, and the generation of strain causes the alteration of the atom location, which will cause the change of the phonon energy. To understand how changes in band structure coupled with changes in carrier scattering caused by strain affect carrier transport. The critical transport factor, scattering, is discussed by basing the phonon scattering model. Here we summarized various phonon scattering modes in Figure 3.1. The intravalley acoustic deformation potential scattering model is widely used to evaluate the phonon-limited electron mobility[15-18], it plays a major role in phonon-limited electron mobility at low temperatures and low field. In addition, since 4H-SiC is an indirect band-gap semiconductor, the intervalley optical is a much more critical role than the intervalley optical and intervalley acoustic model, it is the key factor for the low-dimensional phonon-limited electron mobility in low field. Furthermore, we neglected the piezoelectric scattering, which is more influential in crystals with less symmetry. Thus, in our calculation, the intervalley acoustic deformation potential and intervalley optical scattering model are relevant for the phonon-limited electron mobility.

3.2.1.1 Deformation potential acoustic phonon scattering (intravalley processes)

In phonon scattering, electrons change state by sharing their momentum and energy with phonons. During the exchange procedure, the total energy and momentum of the electrons and phonons remain unchanged. When the energy of the phonon is low, the electron usually remains in the same valley even after the lattice scatters them. This lattice scattering of the final and initial positions of electrons in the same valley in E-k space is called intravalley scattering, as shown in Figure 3.2 (a).

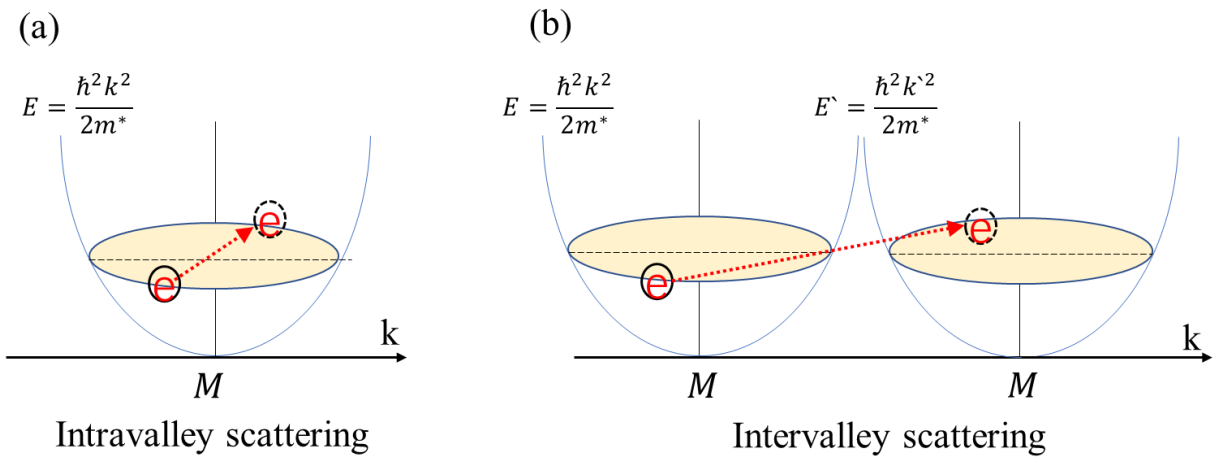

Figure 3.2 Schematic of the intravalley and intervalley scattering model

Using the Fermi golden rule, since the total electrons interact with acoustic phonon by the deformation potential coupling, the scattering probability for intravalley processes (ac) can be given as follows:

$$S_{ac}(k,k`) = \frac{2\pi D_A^2 k_B T}{V\hbar\rho c_L^2}\delta[\epsilon(k`) - \epsilon(k)] \qquad (3.5)$$

where D_A is the deformation-potential tensor, c_L is the longitudinal velocity, ρ is the mass density of the crystal, and V is the volume of the crystal.

3.2.1.2 Deformation potential optical phonon scattering (intervalley processes)

For the indirect bandgap semiconductor 4H-SiC, its conduction band minimum locates at a point either inside the Brillouin zone or at the edge, and there are multiple equivalent conduction band valleys as shown in Figure 3.2 (b). In these cases, electrons may be scattered by the phonons from one valley to another valley, having the same minimum energy level. And it has been found to play an essential role in phonon-limited electron mobility[11]. The intravalley deformation-potential optical-phonon scattering is usually neglected in comparison with intervalley deformation-potential scattering[19-21]. The scattering probability for intervalley processes caused by optical phonons (op) is

$$S_{op}(k,k`) = \frac{Z_f \pi D_{if}^2}{V\hbar\omega_{if}}\left(n_{if}^{op} + \frac{1}{2} \mp \frac{1}{2}\right)\delta\left[\varepsilon_f(k`) - \varepsilon_i(k) \mp \hbar\omega_{if}\right] \qquad (3.6)$$

where D_{if} is the intervalley deformation potential (coupling constants), $\hbar\omega_{if}$ is the intervalley phonon energy. Although the intervalley scattering may also occur from a low-valley to a high nonequivalent valley, this kind of scattering is negligible in our calculation, since it is mostly unimportant for low fields.

3.2.2 Boltzmann transport equation in relaxation-time approximation for 3D carriers

In 4H-SiC, the band minima are located at the M points, which form three full ellipsoids[22, 23]. In the case of the ellipsoidal energy band, as shown in Figure 3.3 (a), both the effective mass and the relaxation time are anisotropic in principle. However, it is known that the anisotropy is small for the 4H-SiC crystal[24]. Thus, in our calculation, we employ the isotropic relaxation time τ dependent on the energy into the scattering term in the Boltzmann transport equation. Therefore, we can relate the relaxation time to the scattering probability S (k, k`), which calculated by using the Fermi golden rule. The relaxation time is given as follows

$$\frac{1}{\tau} = \int \frac{1-f_0`}{1-f_0} S(k,k`)\left(1-\frac{\tau` v` F}{\tau v F}\right)dk` \qquad (3.7)$$

here, f_0 is the Fermi-Dirac distribution. υ is drift electron velocity, and F is electric field strength.

Usually, this is a reasonably complex integral. However, in some simple cases, it becomes quite simplified. The acoustic phonon scattering can be regarded as isotropic parabolic bands and elastic scattering. The relation becomes quite simple since no energy lost in the scattering process. Eqs. (3.7) can be represented as

$$\frac{1}{\tau} = \int S(k,k`)(1-\cos\theta)\frac{d^3k`}{(2\pi)^3} \qquad (3.8)$$

where θ is the angle between k and $k`$, the factor $(2\pi)^3$ in the denominator comes from the definition of the density of states in a k-space volume $d^3k`$.From Eqs. (3.5), (3.8) the relaxation time is rewritten as

$$\frac{1}{\tau} = \frac{D_A^2 k_B T m_d^{*\,3/2} (2\varepsilon)^{1/2}}{\pi\hbar^4 \rho c_L^2} \qquad (3.9)$$

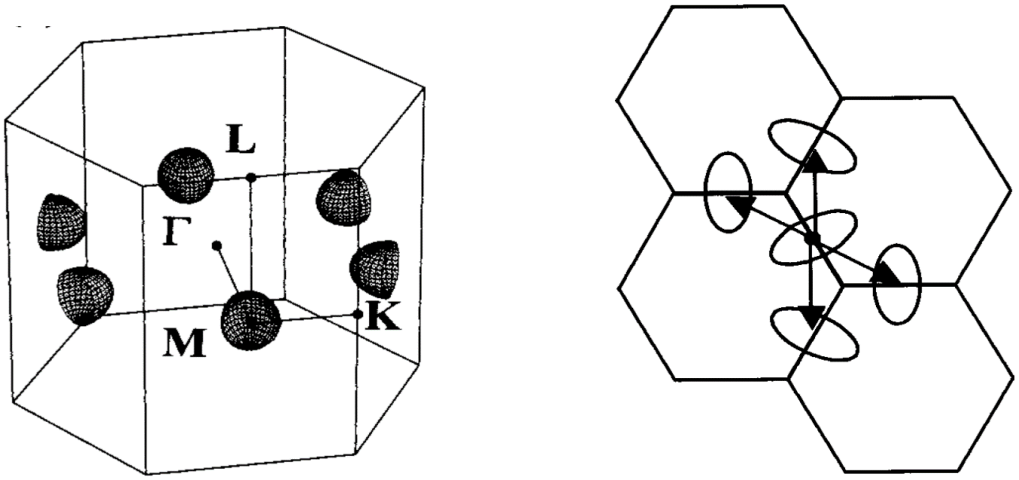

Figure 3.3 (a) Constant energy surface [22] and (b) Top view of the Brillouin zone showing electron transition by intervalley scattering for 4H-SiC [27]

In the case of intervalley optical phonon scattering, since it is an inelastic scattering process, there is no simple way to relate the τ to the S(k,k`), and the problem only can be solved numerically. However, an estimated value of τ can be obtained by utilizing the inverse of S(k), that is, the integral of S(k,k`) overall final states. From Eqs. (3.6) and (3.7) the relaxation time is represented by[25, 26]

$$\frac{1}{\tau} = \frac{Z_f D_{if}{}^2 {m_d}^{*\,3/2} \left(2\,(\varepsilon \pm \hbar\omega_{if})\right)^{1/2}}{2\pi\hbar^3 \rho \omega_{if}} \left(n_\omega + \frac{1}{2} \mp \frac{1}{2}\right), \qquad (3.10)$$

where $n_\omega = {1}\Big/{exp^{\left(\hbar\omega/k_B T\right)} - 1}$ is the number of density of electron, ${m_d}^* = (m_1^* m_2^* m_3^*)^{1/3}$ is the density-of-states mass, ε is electron energy, and Z_f is the number of final valleys available for scattering, in our calculation, as shown in Figure 3.3 (b), Z_f = 4 for 4H-SiC crystal[27].

In a realistic system, the relaxation time τ depends on the energy of the electrons. Therefore, in solving problems such as electron mobility, it is important to explain a proper averaging process for τ used in a macroscopic amount. In our calculation, we assume that the system follows a thermal equilibrium non-degenerate statistics and parabolic energy bands. Based on the basic definition of electron mobility[28]:

$$\mu = \frac{\sigma}{n \cdot e}, \qquad (3.11)$$

Where σ is the electrical conductivity, and n is the number of density of electron,

$$J = \sigma \cdot E = \frac{ne^2 E}{m^*} < \tau >, \qquad (3.12)$$

Based on the Boltzmann transport theory,

$$< J >= \int v \cdot e \cdot g \, d^3k/_{(2\pi)^3} = e^2 \int \frac{\hbar^2 k^2}{3(m^*)^2} \cdot \tau \cdot E \cdot \frac{f}{k_B T} d^3k/_{(2\pi)^3}, \quad (3.13)$$

here, $< J >$ is the average current density, f is the electron distribution, and the factor of 3 comes from the average of x, y, z directions. From Eqs. (3.11) and (3.13), for spherical coordinates, the electron mobility can be represented by

$$\mu = \frac{e}{m^*} < \tau > \; = \frac{e}{m^*} \cdot \frac{2}{3k_B T} \frac{\int \varepsilon^{3/2} \cdot \tau \cdot exp - (\frac{\varepsilon - u_F}{k_B T}) \, d\varepsilon}{\int \varepsilon^{1/2} \cdot exp - (\frac{\varepsilon - u_F}{k_B T}) \, d\varepsilon}, \quad (3.14)$$

The averaging relaxation time ⟨τ⟩ is given as[29]

$$\langle \tau \rangle = \frac{2}{3k_B T} \frac{\int \varepsilon^{3/2} \cdot \tau \cdot exp - (\frac{\varepsilon}{k_B T}) \, \mathrm{d}\varepsilon}{\int \varepsilon^{1/2} \cdot exp - (\frac{\varepsilon}{k_B T}) \, \mathrm{d}\varepsilon}, \quad (3.15)$$

3.3 Electron mobility Calculated in the 3D model

3.3.1 Electron mobility was calculated in the relaxed 4H-SiC

To investigate the effect of stress on the mobility of electrons, we first evaluated the electron mobility based on the phonon scattering mechanism in a perfect 4H-SiC crystal. In our calculation, electron mobility is calculated using

$$\mu = \frac{e \cdot \langle \tau(m^*_{dos}) \rangle}{m^*_c}, \quad (3.16)$$

where $m_d{}^* = (m^*_{M\Gamma} m^*_{MK} m^*_{ML})^{1/3}$ is the density-of-state effective mass. Volm et al. have reported mass values[23], which were $m^*_{M\Gamma} = 0.58m_0$, $m^*_{MK} = 0.31m_0$, $m^*_{ML} = 0.33m_0$. As mentioned before, τ is the relaxation time for an electron with kinetic energy due to phonon scattering, so that the effect of relaxation time on electron mobility is demonstrated by the density of states mass. On the other hand, in 4H-SiC, the constant-energy surface in a *k*-space is an ellipsoid. By averaging over all ellipsoids, we can obtain the conductivity mass as $m^*_c = 3(\frac{1}{m^*_{M\Gamma}} + \frac{1}{m^*_{MK}} + \frac{1}{m^*_{ML}})^{-1}$, which is widely used as the effective mass in the electron mobility calculation of indirect bandgap semiconductors. Thus, the effective mass in Eq. (3.16) is separated into the density-of-state mass and conductivity mass. It can be seen from Eq. (3.16) that, in 4H-SiC crystals, the relaxation time (scattering probability) and the effective conductivity mass are the two main factors affecting electron mobility. Based on the Eqs. (3.9), (3.15) and (3.16), the acoustic phonon limited electron mobility was given as

$$\mu_{Ac} = \frac{e}{m^*_c} \frac{2}{3k_B T} \frac{\sqrt{2}\pi\hbar^4 \rho c_L^2}{\mathrm{D}_A^2 k_B T (m^*_d)^{3/2}} \frac{\int \varepsilon \cdot exp - (\frac{\varepsilon}{k_B T}) \, d\varepsilon}{\int \varepsilon^{1/2} \cdot exp - (\frac{\varepsilon}{k_B T}) \, d\varepsilon}, \quad (3.17)$$

then, from Eqs. (3.10), (3.15) and (3.16), the optical phonon limited electron mobility in the intervalley processes was

given as

$$\mu_{Op} = \frac{2e}{3k_BTm_c^*}\frac{2\pi\hbar^3\rho\omega_{if}}{Z_f{D_{if}}^2 m_d^{*\frac{3}{2}}\left(2\left(\varepsilon\pm\hbar\omega_{if}\right)\right)^{1/2}}\left(\frac{1}{exp\left(\frac{\hbar\omega_{if}}{k_BT}\right)_{-1}}+\frac{1}{2}\mp\frac{1}{2}\right)^{-1}\cdot\frac{\int\varepsilon^{3/2}\cdot exp-(\frac{\varepsilon}{k_BT})\,d\varepsilon}{\int\varepsilon^{1/2}\cdot exp-(\frac{\varepsilon}{k_BT})\,d\varepsilon}, \quad (3.18)$$

The beast agreement between our calculation and A Pérez-Tomás[30] has been obtained with deformation acoustic potential $D_A = 15\text{eV}$ for 4H-SiC and the optical intervalley deformation potential $D_{if} = 7\times10^8$ eV/cm [18] has been used in my calculations. The parameters used in the calculation are shown in Table 3.1. However, it needs to be noted that detailed phonon-limited mobility studies have not been carried out entirely in 4H-SiC until now. thus, the electron-phonon coupling constants in this polytype have not been firmly established.

Table 3.1 Parameters used in the calculation.

Parameters	Unit	Value
Mass of electron m_0	kg	9.11×10^{-31}
Effective electron mass m_1^* (m_{ML}^*)	m_0	0.33
Effective electron mass m_2^* $(m_{M\Gamma}^*)$	m_0	0.58
Effective electron mass m_3^* (m_{MK}^*)	m_0	0.31
Acoustic deformation potential D_A	eV	15.0 [b]
Optical intervalley deformation potential	10^8 eV cm^{-1}	7.0 [b]
Phonon wavevector	$10^{14}\,rad\,s^{-1}$	1.823
Sound velocity	Kms^{-1}	13.73 [a]
Density (ρ)	g cm^{-3}	3.2 [a]
Optic phonon energy at small q values of the phonon wavevector $\hbar\omega_{p=0}$ (E)	meV	120 [b]
Boltzmann constant (k)	J·K^{-1}	1.38×10^{-23}
Planck constant h	Js	6.626×10^{-34}
Reduced Planck constant (Dirac constant) $\hbar$	Js	1.05457×10^{-34}
Elementary charge (e)	C	1.6×10^{-19}

a) Harris et al.[31]

b) Mickevičius et al. [18]

The electron mobilities of relaxed SiC was calculated. The mobility as a function of temperature, based on acoustic phonon scattering models is shown in Figure 3.4 (a), the intervalley optical phonon scattering limited electron mobility is shown in Figure 3.4 (b). Matthiessen's Rule was used to combine the influences from acoustic and optical phonon scattering on phonon-limited electron mobility, and the total phonon-limited electron mobility is shown in Figure 3.4 (c).

$$\frac{1}{\mu_{tot}} = \frac{1}{\mu_{acoustic}} + \frac{1}{\mu_{optial}}, \quad (3.19)$$

We can observe that compared with acoustic phonon, the intervalley optical scattering plays a significant factor in the phonon scattering process in the temperature range of 100-600K.

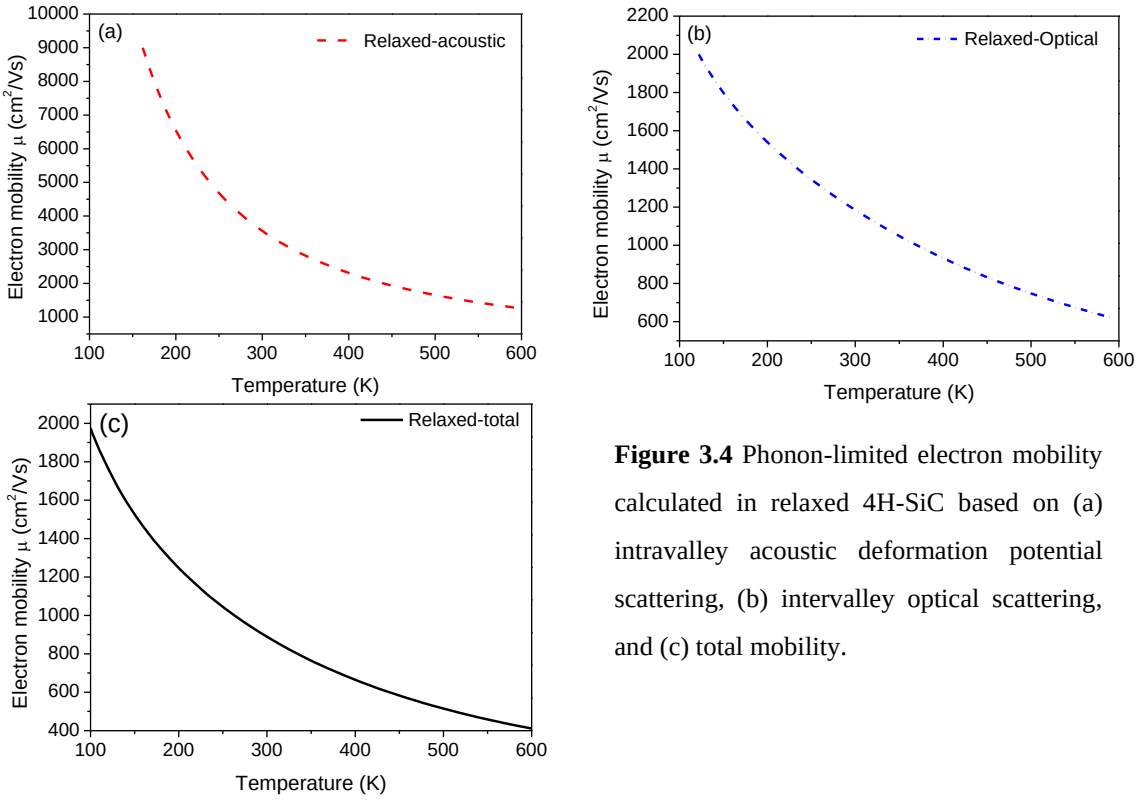

Figure 3.4 Phonon-limited electron mobility calculated in relaxed 4H-SiC based on (a) intravalley acoustic deformation potential scattering, (b) intervalley optical scattering, and (c) total mobility.

3.3.2 Electron mobility was calculated in the strained 4H-SiC

The electron mobility was calculated in the strained 4H-SiC using a strain value as $\Delta a/a$=0.15, 0.3, 0.5, and 1.0% (Δa: the change in the lattice vector). Figure 5 shows the Brillouin zone in the hexagonal plane for both relaxed case (Left) and strained case (Right). The conduction band minimum for 4H-SiC is located at point M of the Brillouin zone. Although the biaxial stress is applied, the crystal symmetry does not change in the x-y plane when the surface is located at c plane. Consequently, the biaxial strain does not affect lifting the band degeneracy, since the states are all on the x-y plane. Thus, in our calculations, only the effective mass in the direction of $\boldsymbol{M \rightarrow \Gamma}$ and $\boldsymbol{M \rightarrow K}$ in $\boldsymbol{k}$ space were taken into account into the electron mobility calculation.

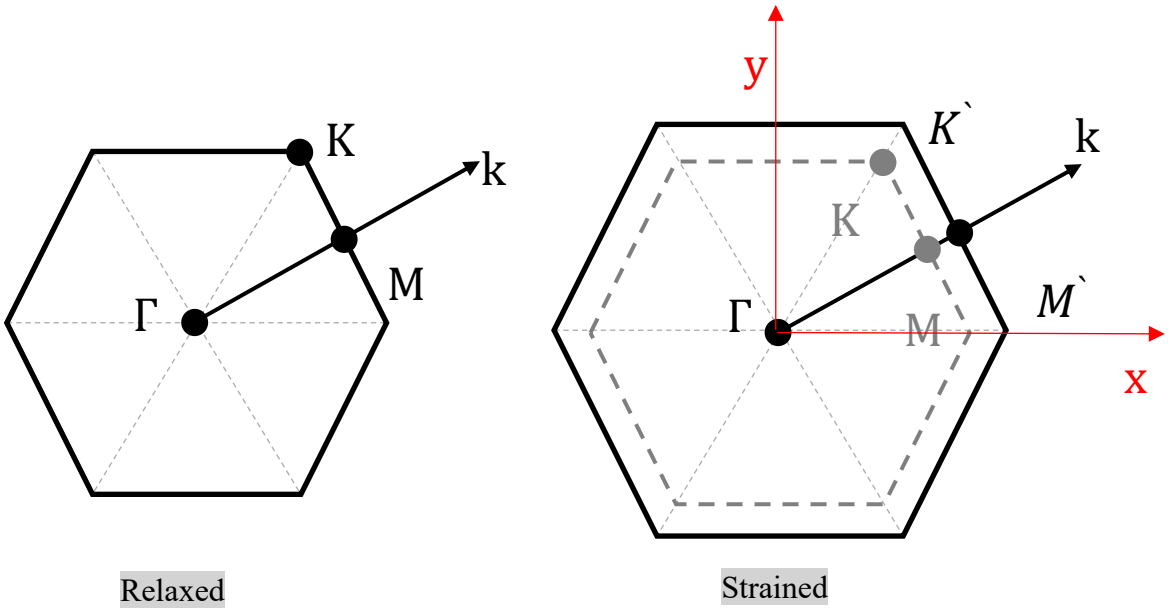

Figure 3.5 First Brillouin zone and changes in biaxial stress. (Left) The equilibrium hexagonal first Brillouin zone and the special k-points Γ, M, and K. (Right) The first Brillouin zone after applying the biaxial stress of the in-plane.

For strained SiC, we extracted the three components (***M→Γ***, ***M→K***, and ***M→Γ***) of effective mass values under strain from the ref. [32] and calculated the m_{dos} and $m_{conduction}$ of in-plane, which is summarized in Table 3.2.

Table 3.2 Summarized the three components of the effective mass (***M→Γ***, ***M→K***, and ***M→Γ***) under 0.15, 0.3, 0.5, and 1.0% strain.

Strain (%)	**$m_{MΓ}$**	**m_{MK}**	**m_{ML}**	**m_{dos}**	**m_{con} in plane**
0.000	0.540	0.280	0.305	0.358	0.369
0.150	0.548	0.275	0.307	0.359	0.367
0.300	0.556	0.273	0.309	0.361	0.366
0.500	0.564	0.270	0.312	0.362	0.365
1.000	0.628	0.267	0.319	0.377	0.374

Based on the strain-induced effective mass change, we calculated the phonon-limited electron mobility, then compared the electron transport properties under strain and relaxed conditions based on acoustic phonon scattering and intervalley optical phonon scattering models, respectively. The electron mobilities of relaxed and strained SiC as a function of temperature, based on acoustic phonon scattering models, are shown in Figure 3.6 (a). The intervalley optical phonon scattering limited electron mobility is shown in Figure 3.6 (b), and the total mobility is shown in Figure 3.6 (C). In strained 4H-SiC, compared with acoustic phonon, the intervalley optical scattering plays a significant factor in the phonon scattering process in the temperature range of 100-600K. In addition, we can clearly observe that when the strain more

than 0.5%, the strain significantly reduced the electron mobility. On the other hand, when the strain is less than 0.5%, the strain basically does not affect the electron mobility.

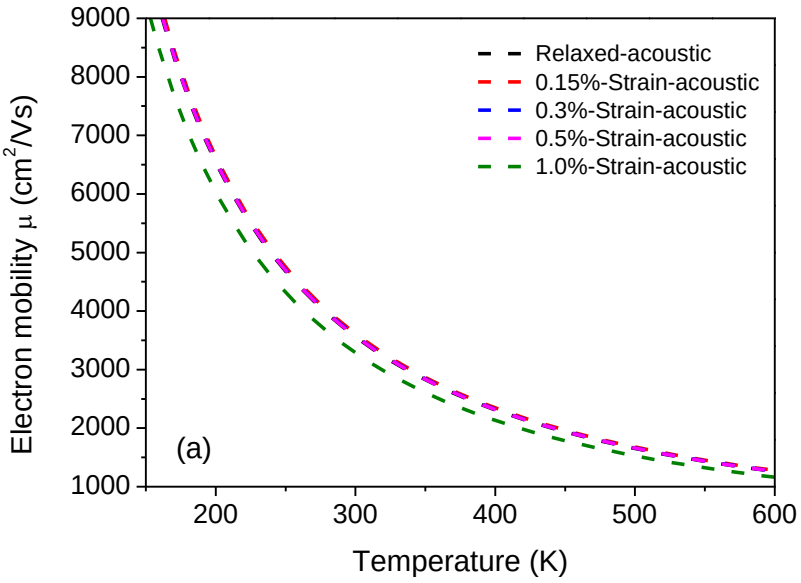

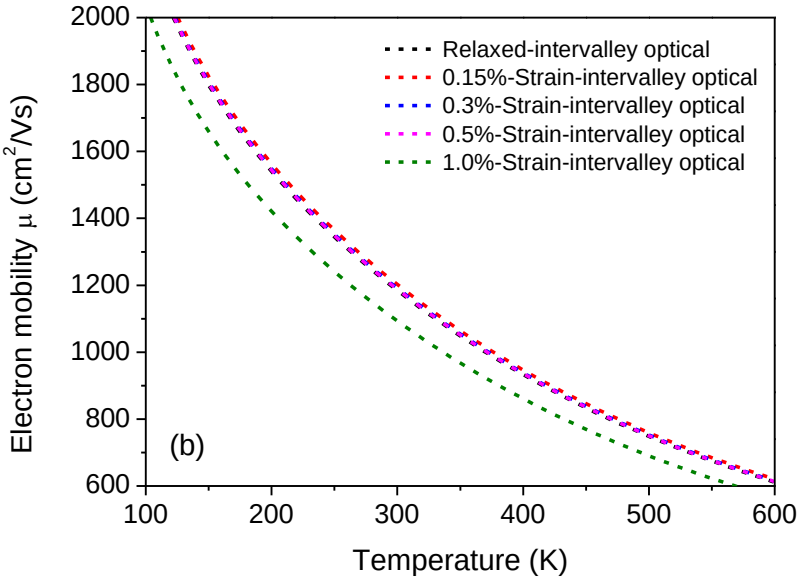

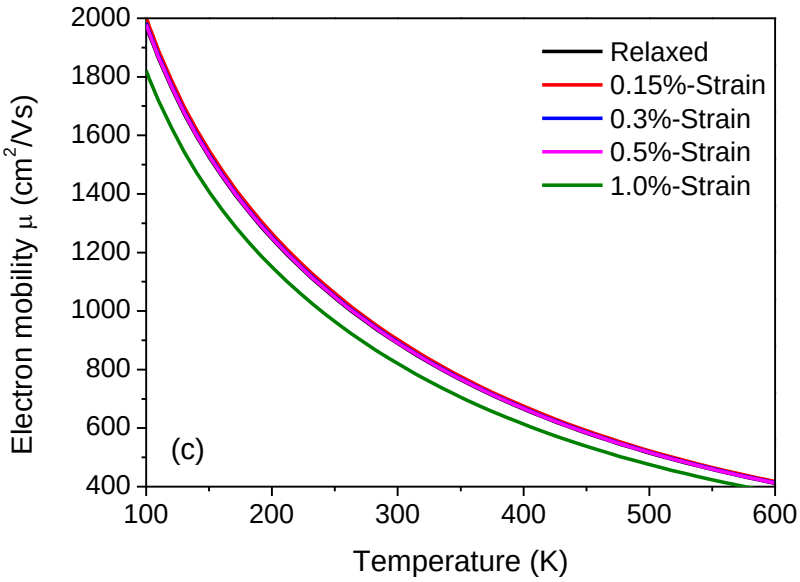

Figure 3.6 Phonon-limited electron mobility calculated in strained 4H-SiC based on (a) intravalley acoustic deformation potential scattering, (b) intervalley optical scattering, and (c) total mobility.

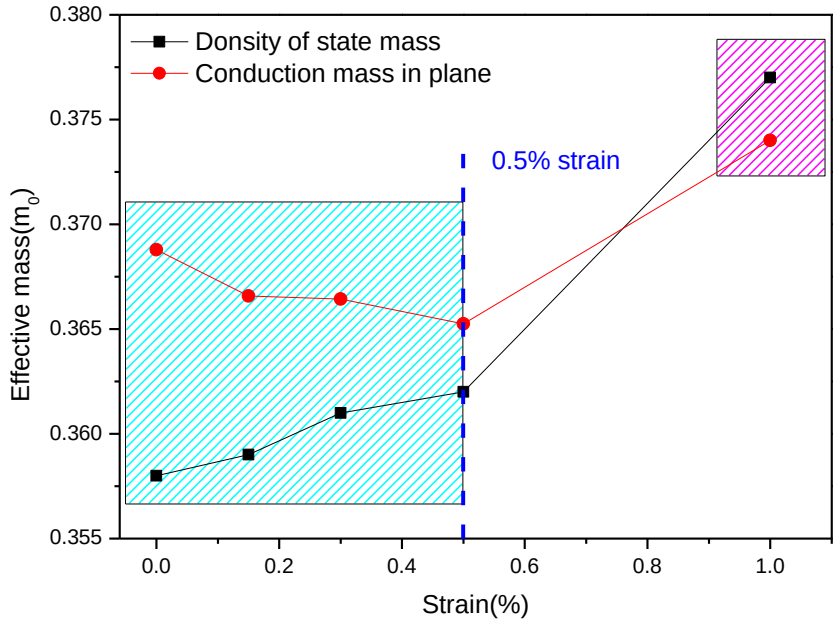

Figure 3.7 Change of the density of state mass and conduction mass of in-plane due to the alteration of the strain values

Figure 3.7 shows the change of the density of state mass and conduction mass of in-plane due to the alteration of the strain values. As mentioned before, in Eq. (14), the two main factors that affect the electron mobility in 4H-SiC crystals

are relaxation time (scattering probability) and the effective conductivity mass. We found that when the strain < 0.5%, the density of state mass and conduction mass of in-plane did not change so much, indicating that the strain-induced effective mass change is too small to affect electron mobility. On the other hand, when the strain > 0.5%, due to the decrease in the scattering probability and increase in the conduction effective mass, the electron mobility is significantly reduced.

3.4 Electron mobility Calculated in the 2D model

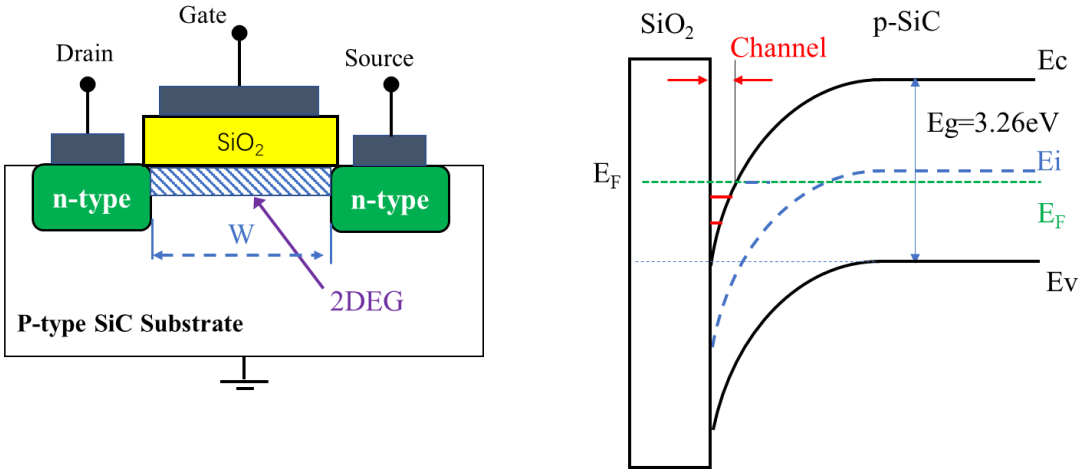

Figure 3.8 Schematic of the SiC-MOSFET characteristic structure and the band is bending profile of the p-SiC substrate at the SiO_2/SiC interface. Forming a 2D channel by bending the energy band to create an inversion layer.

So far, the discussion is based on the phonon scattering model which expresses how electrons are transported within the SiC crystal under biaxial stress in the 3D model. As we know, carriers are free to move in 3D in bulk of the semiconductor. Still, in modern semiconductor devices such as SiC-MOSFETs, the operation of MOSFETs is based on controlling electronic behavior through a tunable external electric field to generate an inversion layer near the SiC/SiO_2 interface, as shown in Figure 3.8. Carriers are usually confined in quantum wells, where they move only in 2D space. Specifically, the carriers in the SiC-MOSFET channel are confined in a potential well near the SiC surface. The scattering rates for these 2D carriers are different than for 3D carriers. To more accurately evaluate the relationship between interfacial stress and electron mobility in the inversion of SiC-MOS, we need to use the electron transport model of a 2D structure at the SiC surface. Electron mobility calculated in the 2D model is a central part of this thesis, and we will, therefore, go more thoroughly into the theoretical foundations of this topic.

3.4.1 Particles in a two-dimensional quantum well

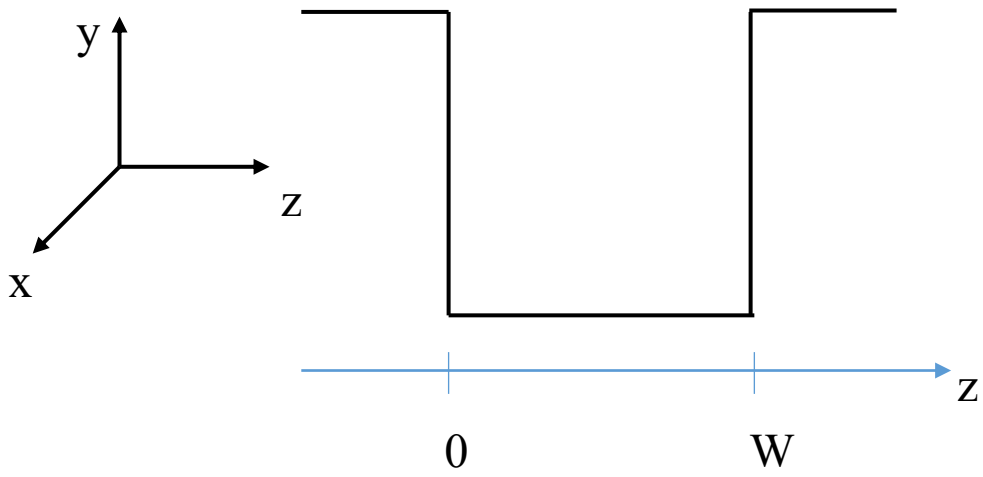

Figure 3.9 Illustration of a quantum well

In a quantum well, if the constraint direction is defined as the z-direction, the motion of the carriers is quantized in the z-direction and is expressed as a series of discrete energy levels. Therefore, when describing the state of the carrier in the z-direction, k_z is no longer critical. However, wave vectors k_x and k_y are still respectable quantum numbers. In a two-dimensional potential well, the particle is restricted by a potential well of size W only in the z-direction, and it can move freely in the x and y planes, as shown in Figure 3.9. At this time, Schrodinger's method needs to be rewritten as

$$[-\frac{\hbar^2}{2m}\nabla^2 + \mathrm{V(z)}]\psi(x,y,z) = E\psi(x,y,z), \text{ (3.20)}$$

When the envelope function is used to describe the variation of the electron distribution probability in a 2D system, the wavefunction should be represented as

$$\psi(x,y,z) = \psi(x,y)\psi(z), \text{ (3.21)}$$

Where $\psi(x,y)$ is the wavefunction of motion in (x, y) plane, and its complex expression is

$$\psi(x,y) = Aexp(ik_x x + ik_y y), \text{ (3.22)}$$

here k_x and k_y are the wavevectors in x and y directions.
Substituting the Eqs. (3.21) and (3.22) into (3.20), we can obtain

$$\frac{\hbar^2}{2m}(k_x^2 + k_y^2)\psi(x,y) = E(x,y)\psi(x,y), \text{ (3.23)}$$

And

$$[-\frac{\hbar^2}{2m}\frac{\partial^2}{\partial z^2} + \mathrm{V(z)}]\psi(z) = E(z)\psi(z), \quad (3.24)$$

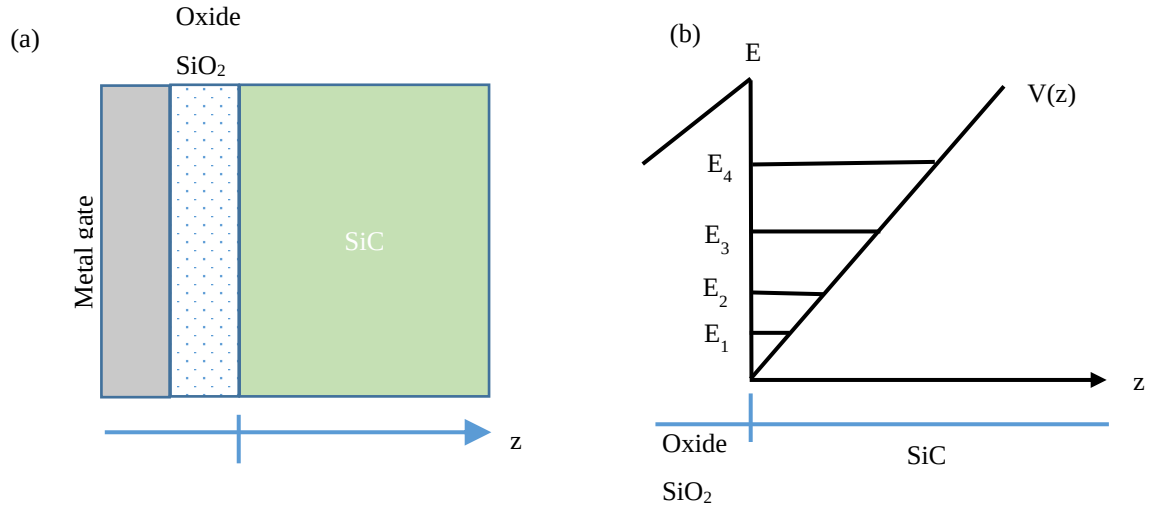

Figure 3.10 (a) Illustration of a metal-oxide-Silicon carbide (MOS) structure sed to confine electrons near the SiO_2/SiC interface. (b) Subbands in the inversion layer at SiO_2/SiC interface

In the case of electrical confinement, the band bending profile of the MOS structure determines V, which is the core of the system. It is related to the charge density distribution through Poisson`s equation, which solving based on the following assumptions: 1) the Boltzmann distribution and 2) the effective state density of the conduction and valence bands. Here we will not repeat the detailed process of solving Poisson`s equation since Taur et al. have already studied this process very clearly.[33] In the inversion layer of the MOSFETs, as shown in Figure 3.10, electrons are usually degenerate, so the Boltzmann distribution should be replaced by the Fermi-Dirac distribution function. In addition, since the electronic state is quantified, the classical model is not sufficient for the charge in the inversion layer. Generally, to simplify the calculation, the problem of the charge distribution of MOS channels can usually be solved by a qualitative quantum mechanical solution based on the channel's electronic structure based on a triangular potential well approximation. It is worthy noted that for low carrier density, the potential well is triangular; however, for the higher densities, the potential is highly nonlinear. Thus, the default condition for our calculation is low carrier density. in the triangular potential well approximation, the electric field in the channel is considered to be a constant in the transverse direction. Based on the triangular potential well approximation, the relationship between the band bending profile V and the electric field may be given by

$$\mathrm{V(z)} = \begin{cases} eFz & z > 0 \\ \infty & z \leq 0, \end{cases} \quad (3.25)$$

where *F* is the effective field along the z-direction. Substituting Equation (3.25) into Equation (3.24), we can obtain

$$\begin{cases} \frac{\hbar^2}{2m}\frac{\partial^2}{\partial z^2}\psi(z) + (E(z) - eFz)\psi(z) = 0 & z > 0 \\ \psi(z) = 0 & z \le 0, \end{cases} \quad (3.26)$$

Appling the envelope function theory to low dimensional semiconductor systems, while using the formal characteristics of the solution to the Airy equation, we can obtain the solution to Equation (3.26), which is expressed as follows

$$\psi_n(z) = C \times A\left[\left(\frac{\hbar^2}{2m}\right)^{1/3}\left(z - \frac{E_n}{eF}\right)\right], n = 0, 1, 2, 3, \ldots, \quad (3.27)$$

where C is the normalization constant. Using the above boundary condition in the triangular potential well approximation, therefore the energy $E(z)$ is quantized as[34]

$$E(z) = E(n) = \frac{\hbar^2 {k_z}^2}{2m} = \frac{\hbar^2\pi^2}{2mW^2}n^2, n = 1,2,3, \ldots \quad (3.28)$$

and $k_z = \frac{n\pi}{w}$, where W is the width of the quantum well. After finding the energy levels in the z-direction, the total energy (the subband energy) of partials in the quantum well can be presented as

$$E = E(n) + \mathrm{E(x,y)} = \frac{\hbar^2\pi^2}{2mW^2}n^2 + \frac{\hbar^2}{2m}\left(k_x^2 + k_y^2\right), \mathrm{n} = 1,2,3, \ldots \quad (3.29)$$

As can be seen from the above formula, although its energy is quantized in the z-direction, it is continuous in the x and y directions, so the total energy is still continuous. Figure 3.11 is a simple picture of the carrier energy versus parallel momentum relation with z-directed momentum as a parameter ($k_{\|}$ is the wave vector in (x, y) plane).

The calculation of the scattering probability in the 2D model is basically the same as the calculation of the 3D electrons,

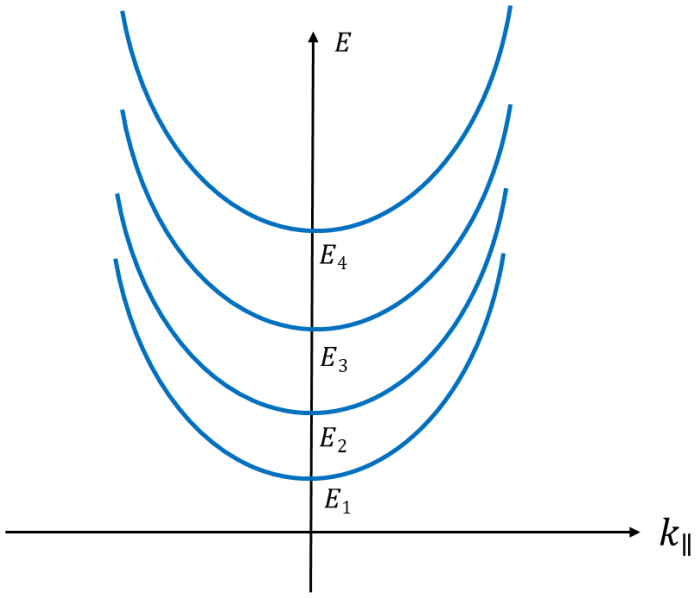

Figure 3.11 Carrier energy versus parallel momentum relate to z-directed momentum as a parameter.

but an appropriate wave function must be used for the restricted carriers. Although we should also consider the possibility of 2D phonons as well as 2D electrons, for many quantum wells, the elastic constant of the wells is similar to those of the surrounding medium. So, 3D phonon behavior can be assumed. In addition, although the method of calculating the scattering probability in the 2D model is different from that in the 3D model, we still want the total scattering rate to be proportional to the density of states. The density of states for a carrier is the number of states allowed in a unit energy interval. It is a significant physical quantity. In three dimensions, the density of states and energy have a parabolic relationship. In virtuously two-dimensional motion, the relationship between the density of states and energy can be derived similarly. Suppose the electron is in a square with side length W, its isoenergy curve in k space should be a circle, and the state density allowed in k space is $W^2/4\pi^2$. The relationship between energy E and wave vector k can be expressed as

$$E = \frac{\hbar^2 k^2}{2m} = \frac{\hbar^2}{2m}\left(k_x^2 + k_y^2\right), \quad (3.30)$$

After taking the electron spin into account, the number of states in this circle is

$$N = 2\pi k^2 \left(\frac{W}{2\pi}\right)^2 = 2\pi(2mE/\hbar^2)\left(\frac{W}{2\pi}\right)^2, \quad (3.31)$$

For electron gas per unit area, $W = 1$

$$N = (m/\pi\hbar^2)E, \quad (3.32)$$

Therefore, for 2D electron gas, the density of states can be rewritten as

$$g_{2D}(E) = N/E = m/\pi\hbar^2 \quad , (3.33)$$

From Eq. (3.33), we can see that instead of the relation of $g_c(E) \propto E^{1/2}$ in 3D, $g_{2D}(E)$ is a constant that is independent of energy. In quasi-two-dimensional motion, E(z) can only be a series of piecewise energy values. A state where the total energy is less than the lowest $E(z)=E_1$ is not allowed to exist. The density of states with energy greater than E_1 is determined by two-dimensional motion. According to Equation 3.30, we can express each allowed energy in the z-direction as

$$E(n) = \frac{\hbar^2 {k_z}^2}{2m}, \quad k_z = \frac{n\pi}{W},$$

$$E(n) = \frac{n^2\hbar^2\pi^2}{2mW^2}, n = 1,2,3, \ldots, \quad (3.34)$$

and its corresponding the density of states (Figure 3.12) is given by

$g_{2Dn}(\mathrm{E}) = \frac{\mathrm{n}m_{2D}}{\pi\hbar^2}, n = 1,2,3, \ldots$ (3.35)

where $m_{2D} = \sqrt{m_x m_y}$ is the density of states effective mass in the 2D model. Figure 3.12 shows the relationship between energy level and its corresponding density of states. Under parabolic approximation, the contribution to the 2D carrier density from each subband E_n is given by

$N_n = \int_{E_n}^{\infty} g_{2Dn}(\mathrm{E}) f_D(E) dE = \frac{m_{2D}k_BT}{\pi\hbar^2} \ln[1 + e^{(\frac{E_F - E_n}{k_BT})}]$, (3.36)

where $f_D(E)$ is the Fermi-Dirac distribution function. Then the 2D carrier density is given by

$N = \frac{m_{2D}k_BT}{\pi\hbar^2} \sum_{n=1}^{\infty} \ln[1 + e^{(\frac{E_F - E_n}{k_BT})}]$, (3.37)

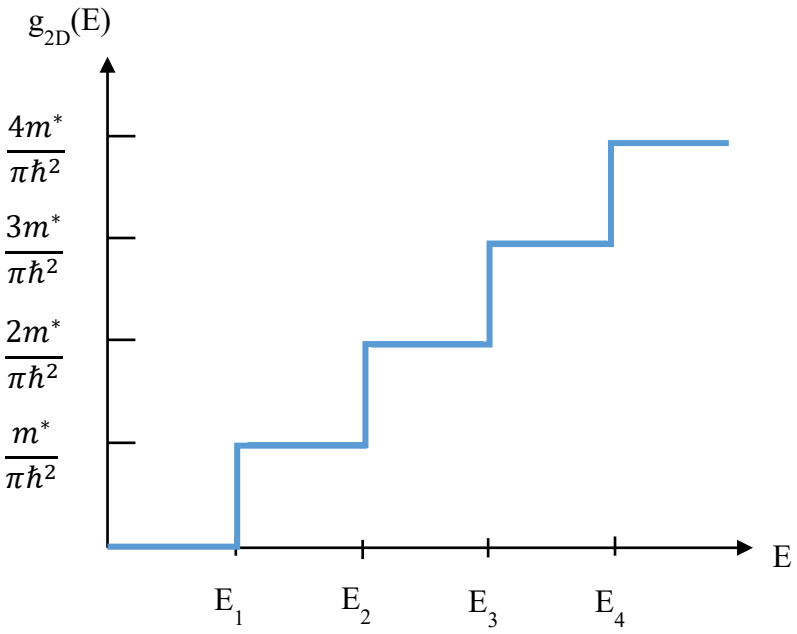

Figure 3.12 Relationship between the subband energy levels and density of states.

3.4.2 Phonon-limited electron transport properties for 2D carriers

The phonon scattering rate in 2D is completely similar to the corresponding result of the 3D carrier, except for two points: (1) the application of momentum conservation only on the plane; (2) the appearance of the form factor, $I_{fi}(z)$, which is due to the imprecise conservation of momentum in the z-direction

$S(k_0, k_0^{`}) = \frac{2\pi}{\hbar} |I_{fi}(z)|^2 |\langle k^{`}|H_1|k\rangle|^2 \delta[E(k^{`}) - E(k) \mp \hbar\omega]$, (3.38)

The scattering rate for the intravalley acoustic scattering of 2D carriers is

$$\frac{1}{\tau_{fi}} = \frac{\pi D_A^2 k_B T}{\hbar c_L} \frac{1}{W_{fi}} g_{2Df}(\mathrm{E}), \quad (3.39)$$

Using equation (3.39) compared to Eq. (3.9), the corresponding result for 3D carriers. We can find that only two differences are replacement of the 3D density of states by 2D of states and the appearance of the $1/W_{fi}$ factor. The general result for both intra- and inter-subband scattering in an infinite square well is

$$\frac{1}{W_{fi}} = \frac{1+2\delta_{ij}}{2W} = \begin{cases} \frac{3}{2W}, & i = f \\ \frac{1}{W}, & i \neq f \end{cases}, \quad (3.40)$$

Based on the equation (3.39) and (3.40), the intravalley acoustic scattering from subband "i" to "i" can be rewritten as

$$\frac{1}{\tau_{ii}} = \frac{\pi D_A^2 k_B T}{\hbar c_L} \frac{3}{2W} g_{2Di}(\mathrm{E}), \quad (3.41)$$

where $g_{2Di}(\mathrm{E})$ is the 2D density of states for the subband, "i". and for intervalley acoustic scattering from subband, "i" to "f" can be rewritten as

$$\frac{1}{\tau_{fi}} = \frac{\pi D_A^2 k_B T}{\hbar c_L} \frac{1}{W} g_{2Df}(\mathrm{E}), \quad (3.42)$$

where $g_{2Df}(\mathrm{E})$ is the 2D density of states for the subband, "f".

The scattering rate for the intervalley optical scattering of 2D carriers is

$$\frac{1}{\tau} = \left(\frac{\pi Z_f {D_{if}}^2}{2\rho\omega_{if}} \frac{1}{W_{fi}}\right) \left(n_\omega + \frac{1}{2} \mp \frac{1}{2}\right) g_{2Df}\left(\mathrm{E} \pm \hbar\omega_{if} - \Delta E_{fi}\right), \quad (3.43)$$

where ΔE_{fi} is the energy difference between subband, "i" and subband, "j". Again, compared with equation (3.10), the only difference is the replacement of the 3D density of states by the 2D density of states and the appearance of the effective interaction length, W_{fi}. The term ΔE_{fi} is the difference between the bands in the final and initial valleys ($\Delta E_{fi} = 0$ for equivalent intervalley scattering).

With the relaxation time τ, the mobility μ is calculated from the equation given below[35]:

$$\mu = -\frac{e}{m^*}\cdot\frac{\int_0^\infty(\varepsilon-\varepsilon_0)\tau\frac{\partial f_0}{\partial\varepsilon}d\varepsilon}{\int_0^\infty f_0\,d\varepsilon} = -\frac{e}{m^*}\frac{2}{2k_BT}\frac{\int_0^\infty(\varepsilon-\varepsilon_0)\cdot\tau\frac{e^{\frac{\varepsilon-E_F}{k_BT}}}{(e^{\frac{\varepsilon-E_F}{k_BT}}+1)^2}d\varepsilon}{\int_0^\infty\frac{1}{e^{\frac{\varepsilon-E_F}{k_BT}}+1}d\varepsilon}, \quad (3.44)$$

where e is the electron charge, ε_0 is the first subband energy, and f_0 is the Fermi-Dirac function. In the 3D model, since the average needs to be performed in the x, y, and z directions, factor 3 appears in the denominator. In the 2D model, factor 2 appears in the denominator because it only needs to be averaged in the x and y directions

Table 3.4 Comparison of electron transports characteristics in 2D and 3D models

	3D	**2D**
Intravalley acoustic	$\frac{1}{\tau(p)} = \frac{\pi D_A^2 k_B T_L}{\hbar c_L}\cdot g_c(\varepsilon)$	$\frac{1}{\tau(fi)} = \frac{\pi D_A^2 k_B T_L}{\hbar c_L}\cdot\frac{1}{W_{fi}}\cdot g_c(\varepsilon)$
Intervalley optical	$\frac{1}{\tau(p)} = \frac{\pi D_{if}^2 Z_f}{2\rho\omega_{if}}\cdot\left(N_i+\frac{1}{2}\mp\frac{1}{2}\right)g_{cf}(\varepsilon\pm\hbar\omega_{if})$	$\frac{1}{\tau(p)} = (\frac{\pi D_{if}^2 Z_f}{2\rho\omega_{if}}\cdot\frac{1}{W_{if}})\left(N_i+\frac{1}{2}\mp\frac{1}{2}\right)g_{2Df}(\varepsilon\pm\hbar\omega_{if}-\Delta E_{fi})$
Density of states	$g_c(\varepsilon_n) = \frac{(2m^*)^{3/2}}{2\pi^2\hbar^3}E^{1/2}(p)$	$g_{2D}(\varepsilon_n) = \frac{nm^*}{\pi\hbar^2}$ (n=1,2,3…n_{max})
Effective interaction length	/	$\frac{1}{W_{fi}} = \frac{\{2+\delta_{fi}\}}{2W}$ (W: width of the quantum well)
Averaging relaxation time $\langle\tau\rangle$	$\langle\tau\rangle = -\frac{2}{3k_BT}\frac{\int_0^\infty\varepsilon^{\frac{3}{2}}\cdot\tau(\varepsilon)\cdot exp-(\frac{\varepsilon}{k_BT})\,\mathrm{d}\varepsilon}{\int_0^\infty\varepsilon^{\frac{1}{2}}\cdot exp-(\frac{\varepsilon}{k_BT})\,\mathrm{d}\varepsilon}$	$\langle\tau\rangle = \frac{\int_0^\infty(\varepsilon-\varepsilon_0)\cdot\tau\frac{\partial f_0}{\partial\varepsilon}\mathrm{d}\varepsilon}{\int_0^\infty f_0\,\mathrm{d}\varepsilon}$,[36]
Electron mobility	$\mu = \frac{e}{m^*}\langle\tau\rangle = \frac{-e}{m^*}\frac{2}{3k_BT}\frac{\int_0^\infty\varepsilon^{3/2}\cdot\tau\cdot exp-(\frac{\varepsilon}{k_BT})\,\mathrm{d}\varepsilon}{\int_0^\infty\varepsilon^{1/2}\cdot exp-(\frac{\varepsilon}{k_BT})\,\mathrm{d}\varepsilon}$	$\mu = \frac{e}{m^*}\langle\tau\rangle = \frac{-e}{m^*}\frac{\int_0^\infty(\varepsilon-\varepsilon_0)\cdot\tau\frac{\partial f_0}{\partial\varepsilon}d\varepsilon}{\int_0^\infty f_0\,d\varepsilon}$ (inter-subband)

3.4.3 Phonon-limited electron calculation for 2D carriers

3.4.3.1 Acoustic phonon-limited electron mobility in the 2D model

For small values of k, acoustic phonons have low energies. Energy momentum conservation requires that the phonons in scattering electrons have small phonon wavevector. For acoustic phonons $\omega/q = v_s$, v_s is sound velocity, since $v_s \sim 10^5$ cm/sec and typically the electron velocity, $v(k) \sim 10^6 - 10^7$ cm/sec. The acoustic phonon close to the zone center have maximum wavevectors, and energy change created by these phonons is $\Delta E_{max} = \hbar\omega_{max} \sim \hbar q_{max}\cdot v_s \sim 10^{-4}\ eV$. The energy change is almost negligible, and phonon scattering is often considered an elastic process since

ΔE_{max} is so much smaller than the electron energy. It is only at very low temperatures that the inelastic nature of acoustic phonon scattering needs to be considered. Based on the Eq. (3.29), the lowest subband energy: $E(1) = \frac{\hbar^2\pi^2}{2mW^2}$, and the next lowest subband energy: $E(2) = \frac{2\hbar^2\pi^2}{mW^2}$. The energy difference between the lowest energy level and the next lowest energy level is $\Delta E = \frac{3\hbar^2\pi^2}{2mW^2} \sim 100$ meV, which is much bigger than acoustic phonon energy. Thus, there is no inter-subband scattering occurred, as shown in Figure 3.13. It is worth noting that in the inversion layer, typically, the inversion electrons are degenerate. Thus, the Fermi-Dirac distribution function should be used instead of the Boltzmann distribution, which used in 3D model calculation. Based on the Eqs. (3.41) and (3.44), the acoustic phonon-limited electron mobility in the 2D model can be given as

$$\mu_{ac2D} = -\frac{e}{m^*}\cdot\frac{\int_0^\infty(\varepsilon)(\frac{\pi D_A^2 k_B T}{\hbar c_L}\frac{3}{2W}g_{2Df})^{-1}\frac{\partial f_0}{\partial\varepsilon}d\varepsilon}{\int_0^\infty f_0\,d\varepsilon} = -\frac{e}{m^*}\cdot\frac{2}{2k_BT}\cdot(\frac{\pi D_A^2 k_B T}{\hbar c_L}\frac{3}{2W}g_{2Df})^{-1}\cdot\frac{\int_0^\infty(\varepsilon)\frac{e^{\frac{\varepsilon-E_F}{k_BT}}}{(e^{\frac{\varepsilon-E_F}{k_BT}}+1)^2}d\varepsilon}{\int_0^\infty\frac{1}{e^{\frac{\varepsilon-E_F}{k_BT}}+1}d\varepsilon}, \quad (3.45)$$

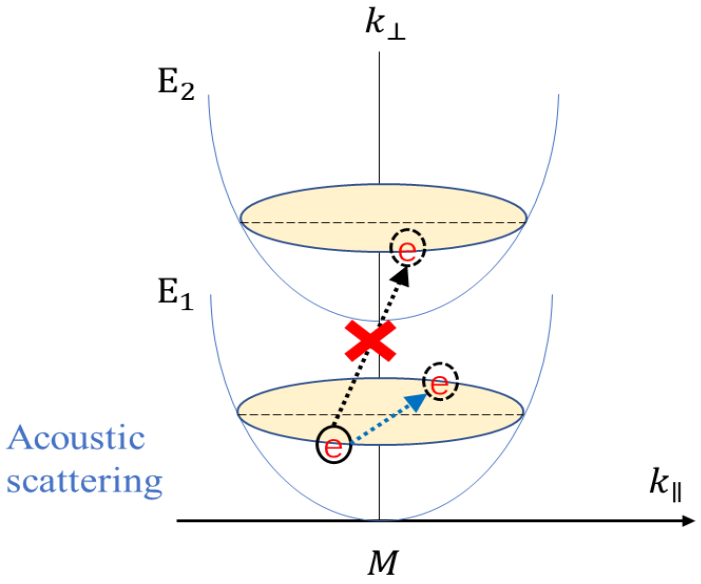

Figure 3.13 Acoustic phonon scattering in the 2D model.

3.4.3.2 Optical phonon-limited electron mobility in the 2D model

As mentioned before, in 4H-SiC, there are three equivalent conduction band valleys, and electrons can scatter between those valleys by absorption or emission of phonons. The phonon dispersion is sometimes called the "zeroth-order process"[37]. The optical phonons have considerable energies at small q values of the phonon wavevector. Until now, the value of phonon energy has been confirmed between 85.4~120 meV[18, 38, 39]. We have previously calculated that the difference between the lowest band energy and the second-lowest band energy of the inversion layer is about 100 meV in the 2D model. In other words, absorbing or emitting an optical phonon can cause subband-to-subband scattering.

Therefore, for the intervalley scattering problem in the 2D model, we must not only consider the intervalley scattering between the equivalued energy levels, as shown in Figure 3.14 scattering process (1) but also the scattering in the inter-subbands, such as in Figure 3.13 scattering process (2).

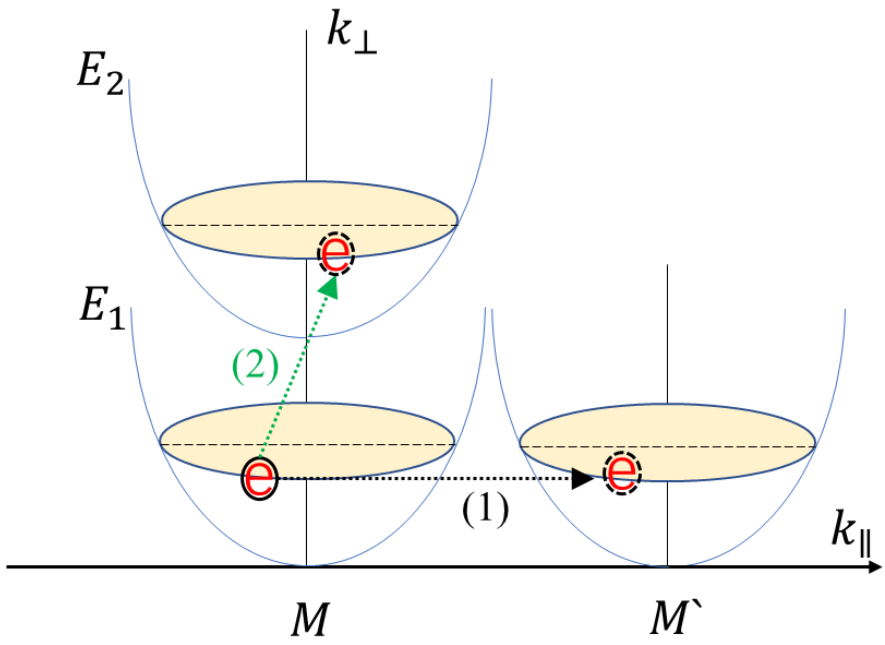

Figure 3.14 Optical phonon intervalley scattering in the 2D model, (1) scattering in the equivalent energy band, and (2) scattering in the inter-subband

First, we discuss the optical phonon scattering between equivalent energy bands. The 2D scattering mechanism, in this case, is basically the same as that in 3D. Therefore, we can apply the 3D calculation model, and only need to make the following modifications.1, Instead of the 3D density of states using 2D DOS; 2, the relaxation time-averaging process only needs to be performed in x and y directions. Based on the Eqs. (3.43) and (3.44), phonon -limited electron mobility μ_{op2D1} of the optical phonon scattered in the equivalent energy band in the 2D model can be given as

$$\mu_{op2D1} = -\frac{e}{m^*}\cdot\frac{\int_0^\infty(\varepsilon)\left(\left(\frac{\pi Z_f {D_{if}}^2}{2\rho\omega_{if}}\frac{1}{W_{fi}}\right)\left(n_\omega+\frac{1}{2}\mp\frac{1}{2}\right)g_{2Df}\left(\mathrm{E}\pm\hbar\omega_{if}-\Delta E_{fi}\right)\right)^{-1}\frac{\partial f_0}{\partial\varepsilon}\,d\varepsilon}{\int_0^\infty f_0\,d\varepsilon}$$

$$= -\frac{e}{m^*}\cdot\frac{2}{2k_BT}\cdot\left(\left(\frac{\pi Z_f {D_{if}}^2}{2\rho\omega_{if}}\frac{1}{W_{fi}}\right)\left(n_\omega+\frac{1}{2}\mp\frac{1}{2}\right)g_{2Df}\left(\mathrm{E}\pm\hbar\omega_{if}-\Delta E_{fi}\right)\right)^{-1}\cdot\frac{\int_0^\infty(\varepsilon)\cdot\frac{e^{\frac{\varepsilon-E_F}{k_BT}}}{(e^{\frac{\varepsilon-E_F}{k_BT}}+1)^2}d\varepsilon}{\int_0^\infty\frac{1}{e^{\frac{\varepsilon-E_F}{k_BT}}+1}d\varepsilon}\quad,(3.46)$$

Since this scattering occurred in the equivalent intervalley, based on the Eq. (3.40), $W_{fi} = \frac{3}{2W}$; and as mentioned in 3D scattering, $\Delta E_{fi} = 0$. The Eq. (3.46) can be rewritten as

$$\mu_{op2D1} = -\frac{e}{m^*}\cdot\frac{2}{2k_BT}\cdot\left(\left(\frac{\pi Z_f D_{if}{}^2}{2\rho\omega_{if}}\frac{3}{2W}\right)\left(n_\omega+\frac{1}{2}\mp\frac{1}{2}\right)g_{2Df}(E_1)\right)^{-1}\cdot\frac{\int_0^\infty(\varepsilon)\cdot\frac{e^{\frac{\varepsilon-E_F}{k_BT}}}{\left(e^{\frac{\varepsilon-E_F}{k_BT}}+1\right)^2}d\varepsilon}{\int_0^\infty\frac{1}{e^{\frac{\varepsilon-E_F}{k_BT}}+1}d\varepsilon}, \quad (3.47)$$

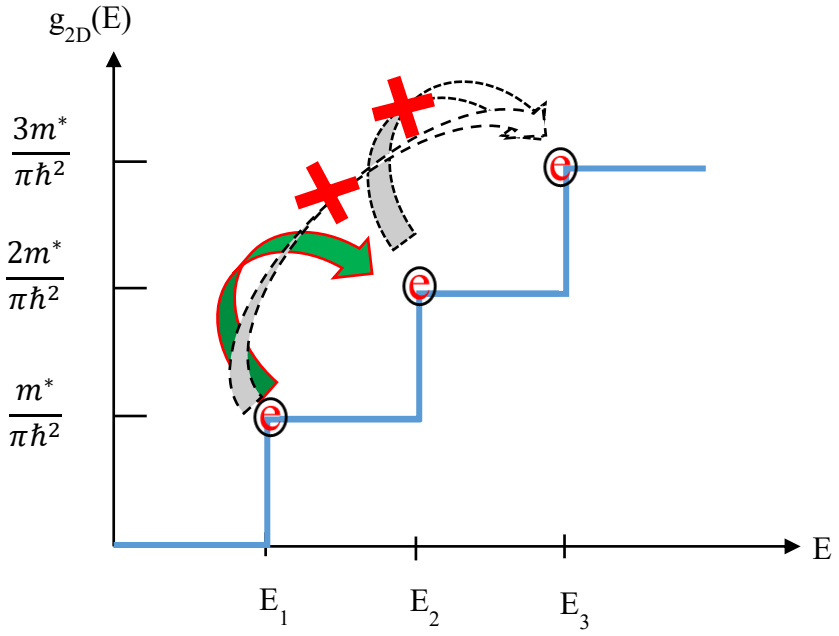

Figure 3.15 Subband energy levels that allow scattering to occur and their corresponding density of states in the 2D model

Then, we discuss the optical phonon scattering in the inter-subband case. As mentioned earlier, when optical phonon scattering occurs in the inversion layer, electrons may be scattered into the one higher-order or one lower-order energy subband. Therefore, we need to consider inter-subband scattering. According to calculations, the optical phonon energy is not enough to cause scattering with higher that one order energy differences, which shows in Figure 3.15. Thus, in our estimates, we neglect the inter-subband scattering processes, such as from E_1 to E_3 or from E_2 to E_3. Based on the Eqs. (3.43) and (3.44), phonon -limited electron mobility μ_{op2D2} of the optical phonon scattered in the inter-subband in the 2D model can be given as

$$\mu_{op2D2} = -\frac{e}{m^*}\cdot\frac{2}{2k_BT}\cdot\left(\left(\frac{\pi Z_f D_{if}{}^2}{2\rho\omega_{if}}\frac{1}{W}\right)\left(n_\omega+\frac{1}{2}\mp\frac{1}{2}\right)g_{2Df}\left(\mathrm{E}\pm\hbar\omega_{if}-\Delta E_{fi}\right)\right)^{-1}\cdot\frac{\int_0^\infty(\varepsilon)\cdot\frac{e^{\frac{\varepsilon-E_F}{k_BT}}}{\left(e^{\frac{\varepsilon-E_F}{k_BT}}+1\right)^2}d\varepsilon}{\int_0^\infty\frac{1}{e^{\frac{\varepsilon-E_F}{k_BT}}+1}d\varepsilon}, \quad (3.48)$$

Here, $W_{fi} = \frac{1}{W}$; and $\Delta E_{fi} \neq 0$. The energy change is not enough to cause scattering with higher that one order energy differences, thus, the 2D density of states $g_{2Df}\left(\mathrm{E}\pm\hbar\omega_{if}-\Delta E_{fi}\right)$ can be replaced by $g_{2Df}(\mathrm{E}_2)$. Moreover, when the carrier concentration is low since the energy of the electrons is too small to emit a phonon, at this time, only the absorption process occurs. The mobility can be represented as

$$\mu_{op2D2} = -\frac{e}{m^*}\cdot\frac{2}{2k_BT}\cdot\left(\left(\frac{\pi {Z_f}{D_{if}}^2}{2\rho\omega_{if}}\frac{1}{W}\right)(n_\omega - 1)g_{2Df}(\mathrm{E}_2)\right)^{-1}\cdot\frac{\int_0^\infty(\varepsilon)\cdot\frac{e^{\frac{\varepsilon-E_F}{k_BT}}}{(e^{\frac{\varepsilon-E_F}{k_BT}}+1)^2}d\varepsilon}{\int_0^\infty\frac{1}{e^{\frac{\varepsilon-E_F}{k_BT}}+1}d\varepsilon} \quad (3.49)$$

3.4.4 Result and Conclusion for 2D carriers

The electron mobilities of relaxed SiC was calculated. The mobility as a function of temperature, based on 2D acoustic phonon scattering models is shown in Figure 3.16 (a), the intervalley optical phonon scattering in the equivalent subband limited electron mobility is shown in Figure 3.16 (b), and the intervalley optical phonon scattering in the inter-subband limited electron mobility is shown in Figure 3.16 (c).To combine acoustic and optical phonon scattering influences on electron mobility using Matthiessen's Rule, the total optical phonon-limited, and the total phonon-limited electron mobility is shown in Figure 3.16 (d) and (e). By comparing Figures 3.16 (a) and (d), we found that compared with the 3D model, the phenomenon that intravalley acoustic phonon scattering plays a leading role in the overall electron mobility in the low-temperature range is more prominent. While at high temperatures, optical phonon scattering dominates the entire phonon-limited electron mobility. In addition, it can be seen from Figures 3.16 (b) and (c) that the contribution of the optical phonon scattering from subband-to-subband on the total phonon-limited electron mobility is significantly greater than that from optical phonon scattering in the equivalent subband. The above trends are more in line with general electron transmission characteristics[40]. Therefore, we believe that the electron mobility under the interface stress calculated based on the 2D model can more accurately reflect the influence of the interface stress on the electron transport characteristics.

Then, the electron mobility was calculated in the strained 4H-SiC using a strain value as $\Delta a/a$= 0.1, 0.3, 0.5, and 1.0%. Based on the strain-induced effective mass change of in-plane, we calculated the phonon-limited electron mobility in 2D mode, then compared the electron transport properties under strain and relaxed conditions based on acoustic phonon scattering and intervalley optical phonon scattering models, respectively.

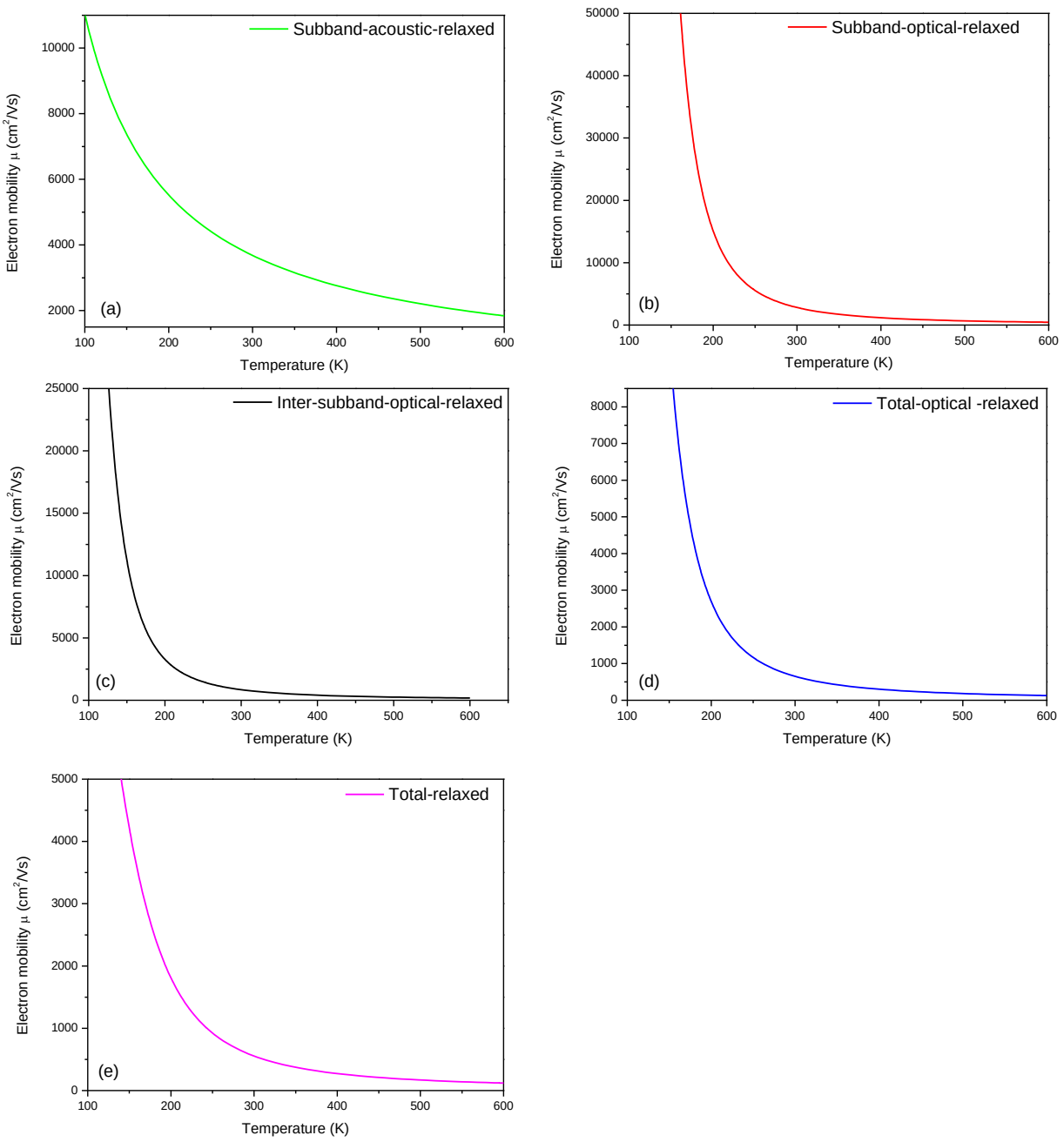

Figure. 3.16. (a) Electron mobilities of relaxed SiC as a function of temperature calculated using the acoustic phonon scattering models. (b) Electron mobilities calculated using the intervalley optical phonon scattering models in the equivalent subband. (c) Electron mobilities calculated using the intervalley optical phonon scattering models in the inter-subband. (d) The total intervalley optical phonon-limited mobility. (e) The total phonon-limited mobility.

Table 3.5 Summarized the three components of the effective mass (***M→Γ***, ***M→K***, and ***M→Γ***) under 0.1, 0.3, 0.5, and 1.0% strain, and calculated values of density of states mass and conduction mass of in-plane.

Strain (%)	$m_{M\Gamma}$	m_{MK}	m_{ML}	$m_d^* = \sqrt{m_{M\Gamma}^* \cdot m_{MK}^*}$ in-plane	$m_c^* = 2(\frac{1}{m_{M\Gamma}^*} + \frac{1}{m_{MK}^*})^{-1}$ in-plane
0.000	0.540	0.280	0.305	0.3888	0.369
0.150	0.548	0.275	0.307	0.3882	0.367
0.300	0.556	0.273	0.309	0.3896	0.366
0.500	0.564	0.270	0.312	0.3902	0.365
1.000	0.628	0.267	0.319	0.4095	0.374

The electron mobilities of relaxed and strained SiC as a function of temperature, based on acoustic phonon scattering models is shown in Figure 3.17 (a). The intervalley optical phonon scattering in the equivalent subband limited electron mobility is shown in Figure 3.17 (b), and intervalley optical phonon scattering in the inter-subband limited electron mobility is shown in Figure 3.17 (c). The total optical phonon-limited and the total phonon-limited electron mobility is shown in Figure 3.17 (d) and (e). For strained 4H-SiC, although the value of the electron mobility calculated based on the phonon scattering mechanism is different between the 2D model and the 3D model. However, we observe the same tendency of the electron mobility to have more stress changes, that is, when the strain is more significant than 0.5%, the strain significantly reduces the electron mobility. On the other hand, when the strain is less than 0.5%, the strain does not substantially affect the electron mobility.

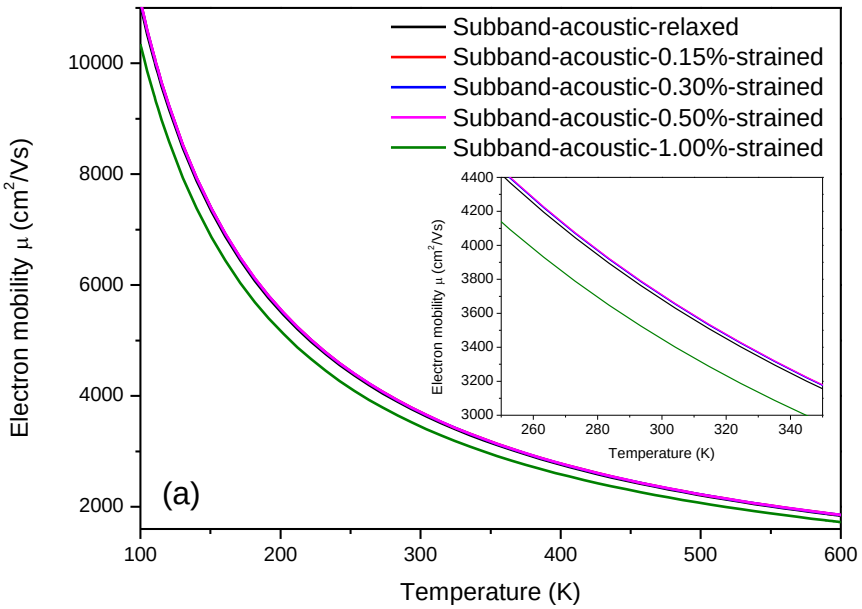

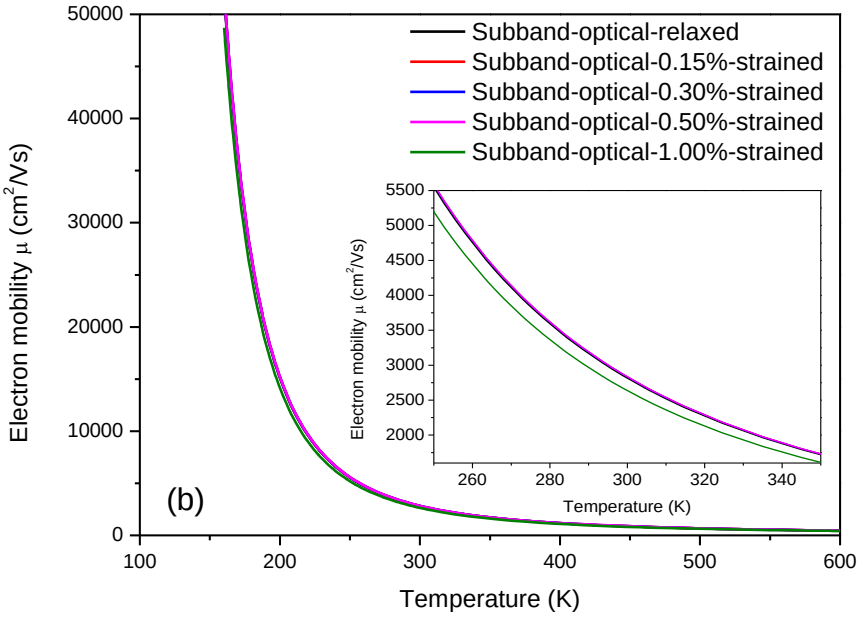
Subband-optical-relaxed
Subband-optical-0.15%-strained
Subband-optical-0.30%-strained
Subband-optical-0.50%-strained
Subband-optical-1.00%-strained
Electron mobility μ (cm²/Vs)
Temperature (K)
(b)

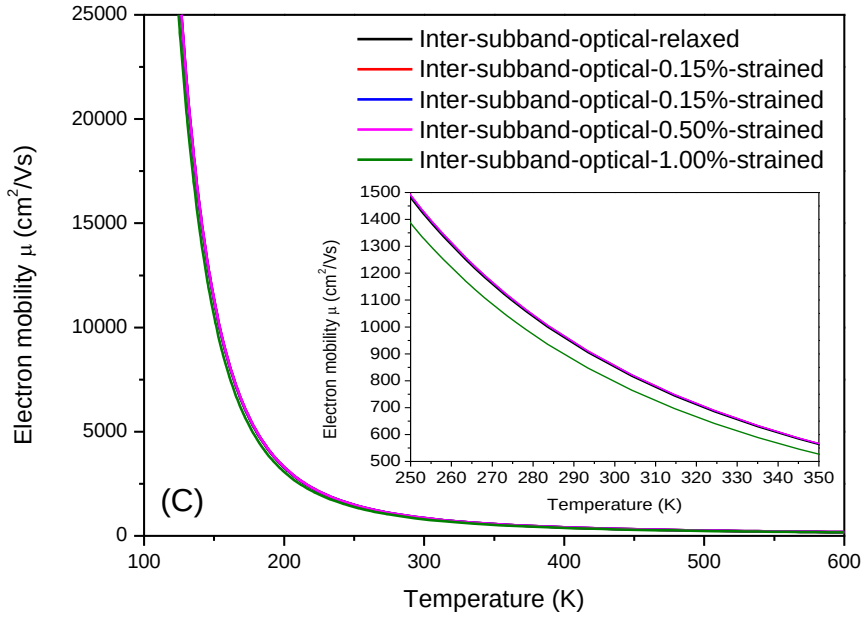
Inter-subband-optical-relaxed
Inter-subband-optical-0.15%-strained
Inter-subband-optical-0.15%-strained
Inter-subband-optical-0.50%-strained
Inter-subband-optical-1.00%-strained
Electron mobility μ (cm²/Vs)
Temperature (K)
(C)

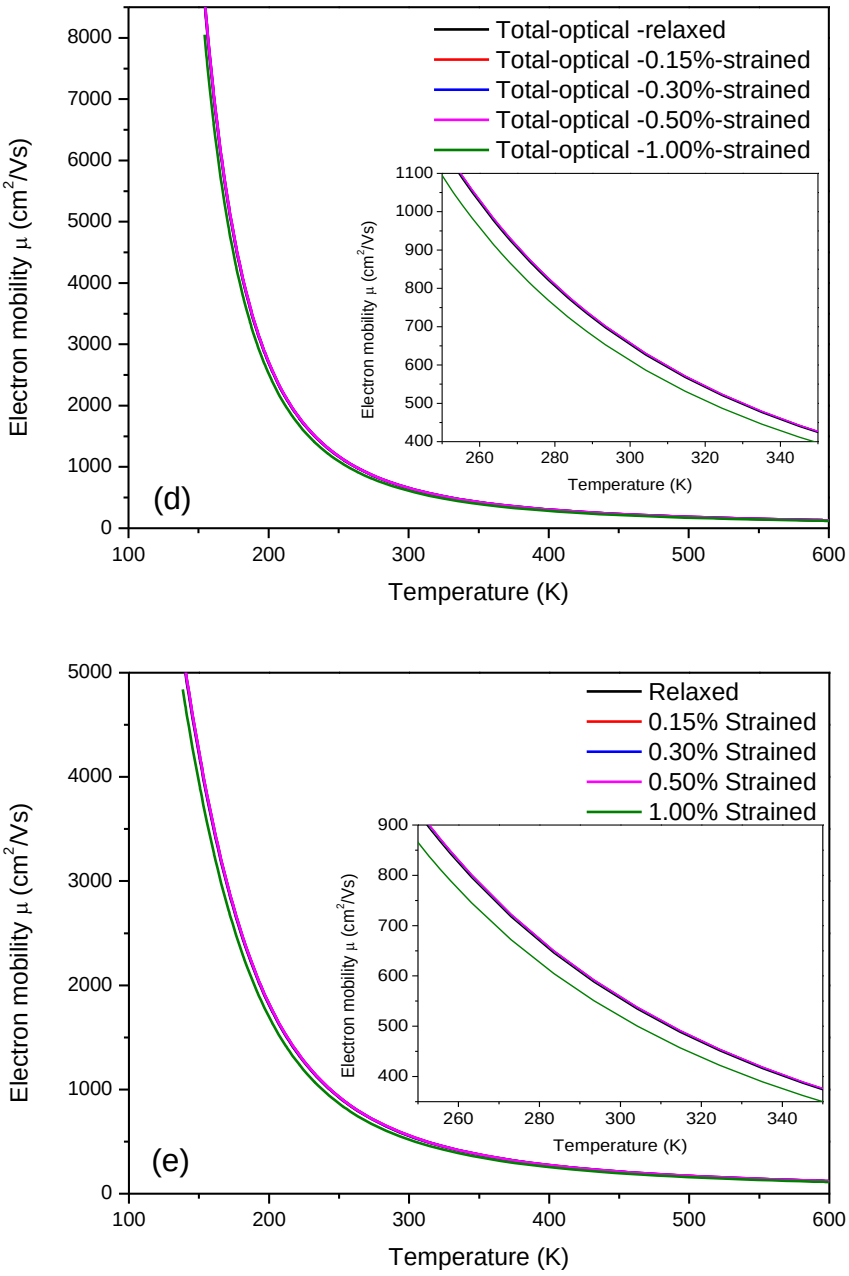

Fig. 3.17. (a) Electron mobilities of strained SiC as a function of temperature calculated using the acoustic phonon scattering models. (b) Electron mobilities calculated using the intervalley optical phonon scattering models in the equivalent subband. (c) Electron mobilities calculated using the intervalley optical phonon scattering models in the inter-subband. (d) The total intervalley optical phonon-limited mobility. (e) The total phonon-limited mobility.

We extracted the electron mobility of each scattering component corresponding to different interface stress values at a temperature of 300 K and a carrier concentration of $2.5 \times 10^{12}\ cm^{-2}$. We extracted the electron mobility corresponding to different values for each interface stress component scattering. According to Matthiessen's rule, each component having

a reciprocal relationship with the total electron mobility. Thus, in Figure 3.18, the vertical axis shows the inverse of the electron mobility corresponding to each component. In other words, the higher the inverse of the electron mobility, the more significant its contribution to the total mobility. We can see that at 300K, intervalley optical phonon scattering, especially subband-to-subband optical scattering, is the main factor affecting the phonon-limited electron mobility. At this temperature, the effect of equivalent subband optical phonon scattering on electron mobility is almost the same magnitude as that of intravalley acoustic scattering.

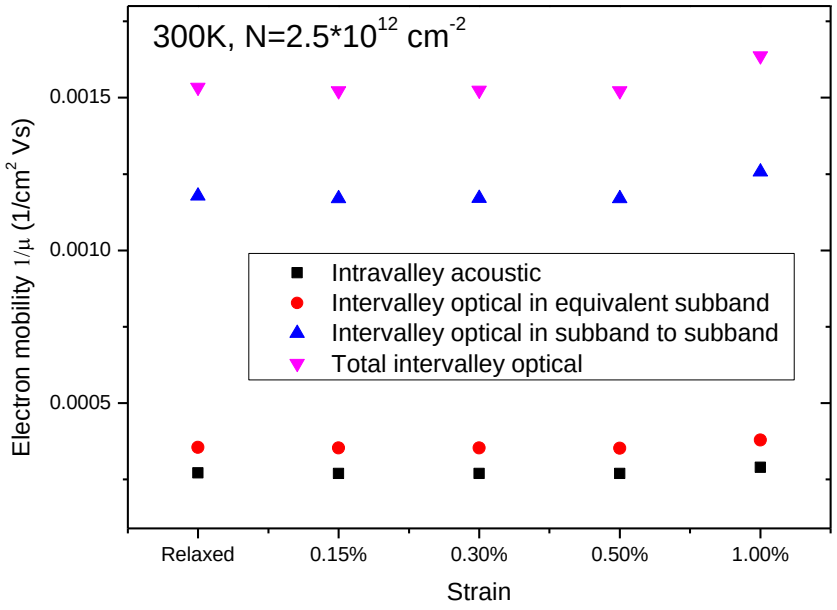

Fig. 3.18. Electron mobility of each scattering component corresponding to different interface stress values at a temperature of 300K and a carrier concentration of $2.5 \times 10^{12}\ cm^{-2}$.

In addition, since in the actual MOSFET device, the application of the gate voltage will change the carrier concentration in the channel and affect the electron mobility of the inversion layer, we evaluated the concentration dependences of the low-field phonon-limited mobility in the 2D model. Based on equation (4.47), electron mobility can be related to the 2D carrier concentration. The electron mobilities of SiC with different carrier concentrations as a function of strain, based on acoustic phonon scattering models, are shown in Figure 3.19. We can easily observe from the figure that as the carrier concentration decreases, the electron mobility increases. This trend agrees well with the previous studies[41, 42], and it can be explained as low electron concentration causes the Fermi energy level to shift upward, thereby increasing the average carrier lifetime. More importantly, although we get different electron mobility under different carrier concentration conditions, they have the same trend, that is, the effect of interface stress on the electron mobility is independent of the carrier concentration.

$$N_{2D} = \int g_{2D}(E) f_0(E)\, dE = \int g_{2D}(E) \cdot (1 + Exp(\tfrac{\varepsilon - E_F}{kT}))^{-1}\, dE, \quad (4.50)$$

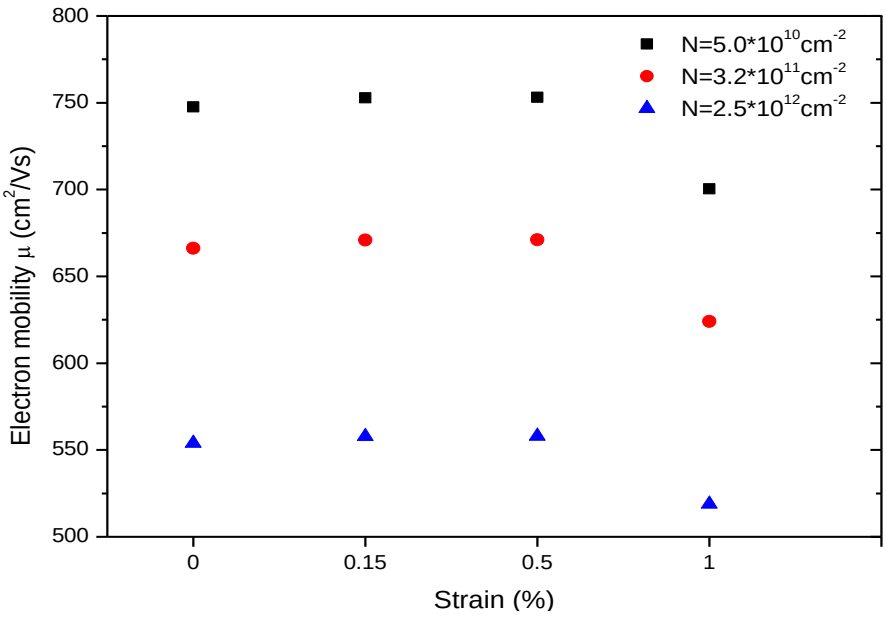

Fig. 3.19. Concentration dependences of low-field phonon-limited mobility in the 2D model.

3.5. Conclusions for the strain at the thermal oxidized SiO_2/SiC interface

3.5.1 Experimentally measured stress value at SiO_2/4H-SiC interface

Before discussing the relationship between stress and electron mobility, we first need to figure out the relationship between stress and strain. Here we use an example to illustrate how to determine the strain tensor from stress. A semiconductor layer pseudomorphically grow on a (001)-orientated lattice-mismatched substrate is schematically shown in Fig. 3.20. In this case, the bottom layer is biaxially strained, and the strain components e_{xx} and e_{yy} are

$$e_{xx} = e_{yy} = \frac{\alpha_0 - \alpha}{\alpha} \qquad (3.51)$$

The strain is tension in the x-y plane. In hexagonal crystal: the strain components e_{xx} and e_{yy} can be represented as

$$e_{xx} = e_{yy} = -\frac{T}{C_{11}+C_{12}-2\left(C_{13}^2/C_{33}\right)} = \frac{\alpha_0 - \alpha}{\alpha} \qquad (3.52)$$

Where T is the magnitude of the equivalent in-plant tension stress in kbar, the coefficients C_{ij} are called elastic stiffness constants.

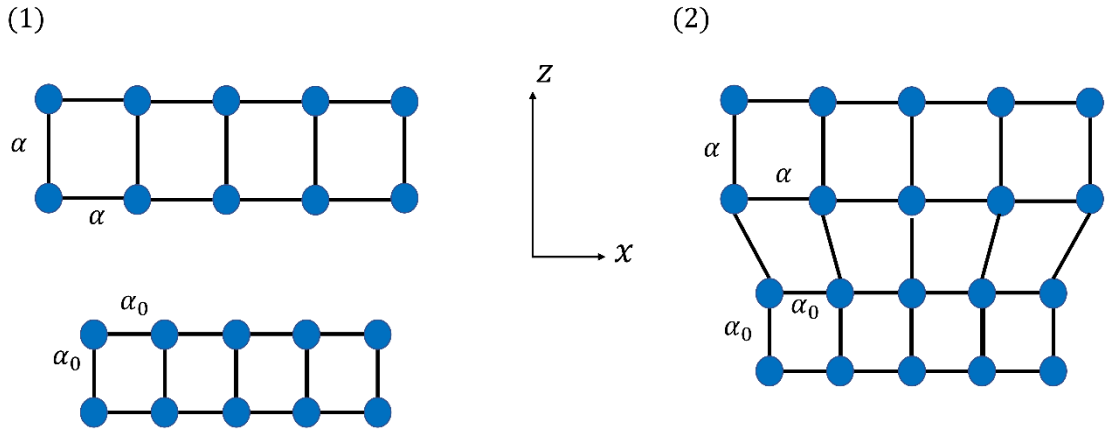

Figure. 3.20 Schematic diagram of biaxial stress (strain) generation process. (1) Prior to growth, two different material layers have different lattice constants. (2) After the formatting of the heterojunction, the lattice constant of the top layer conforms to that of the bottom layer, and biaxial stress (strain) generates at the interface.

In previous studies, we have calculated the specific values of interfacial stresses for four dry oxidation samples subjected to different annealing processes. Based on this, the realistic strain values at the interface of SiO_2/4H-SiC were calculated by using Eqs. (3.52), and elastic stiffness constants $\{C_{ij}\}$ values, given as C11 = 501 GPa, C12 = 111 GPa, C13 = 52 Gpa, C33 = 553 Gpa, C44 = 163 GPa.[43] Realistic strain values are shown in Table 3.3. Since the actual value of the strain at the thermal oxidized SiO_2/SiC interface is only around 0.1-0.16% < 0.5%. This may indicate that the generation of deformation potential due to interface stress induced by the thermal oxidation, does not affect the electron mobility at the SiO_2/SiC interface.

Table 3.3. Interface stress at SiO_2/4H-SiC measured in Ref. [9], and calculated strain value in this work.

	Sample 1	**Sample 2**	**Sample 3**	**Sample 4**
Stress σ (MPa) in Ref 35	94.12	51.89	84.30	80.54
Calculated Strain (%)	0.156	0.086	0.140	0.134

3.5.2 The relationship between the electron mobility and the actual value of the strain at the thermal oxidized SiO_2/SiC interface

Based on the phonon-limited electron mobility in the 3D and 2D model, we found that when the strain < 0.5%, the density of states effective mass and conduction effective mass of in-plane did not significantly change, indicating that the strain-induced effective mass change is too small to affect electron mobility, when the strain > 0.5%, due to the decrease in the scattering probability and increase in the conduction effective mass, the electron mobility is significantly reduced. However, the actual value of the strain at the thermal oxidized SiO_2/SiC interface is only around 0.1-0.16% < 0.5%. This may indicate that the generation of deformation potential due to interface stress induced by the thermal oxidation, does

not affect the electron mobility at the SiO_2/SiC interface.

3.6. Summary and Next step work

As mentioned before, the interface stress-induced lattice distortion may affect the electron mobility in two possible ways: (1) Generation of the deformation potential; (2) Formation of the interface defects. Based on our calculation results, the high-temperature thermal oxidation induced interface stress has so little effect on the effective mass that does not affect the electron mobility in the inversion layer of the SiC-MOS. Thus, we can consider that the interface stress-induced lattice distortion may mainly affect the electron mobility by the formation of the interface defects.

To suppress the interface stress generates at the interface of SiO_2/SiC, it is necessary to develop a low-temperature oxidation method for the fabrication of the SiC-MOS structures. The Nitric acid oxidation of SiC (NAOS) way was employed in our next step work.

3.7. Reference

[1] M. Dean, Semiconductor and conventional strain gauges, Academic Press, 1962.

[2] C.K. Maiti, S. Chattopadhyay, L. Bera, Strained-Si heterostructure field effect devices, CRC Press, 2007.

[3] K. Mistry, M. Armstrong, C. Auth, S. Cea, T. Coan, T. Ghani, T. Hoffmann, A. Murthy, J. Sandford, R. Shaheed, Delaying forever: Uniaxial strained silicon transistors in a 90nm CMOS technology, in: Digest of Technical Papers. 2004 Symposium on VLSI Technology, 2004., IEEE, 2004, pp. 50-51.

[4] M.L. Lee, E.A. Fitzgerald, M.T. Bulsara, M.T. Currie, A. Lochtefeld, Strained Si, SiGe, and Ge channels for high-mobility metal-oxide-semiconductor field-effect transistors, Journal of Applied Physics, 97 (2005) 1.

[5] S.E. Thompson, G.Y. Sun, Y.S. Choi, T. Nishida, Uniaxial-process-induced strained-Si: Extending the CMOS roadmap, Ieee Transactions on Electron Devices, 53 (2006) 1010-1020.

[6] K. Shiraishi, K. Chokawa, H. Shirakawa, K. Endo, M. Araidai, K. Kamiya, H. Watanabe, First principles study of SiC/SiO 2 interfaces towards future power devices, in: 2014 IEEE International Electron Devices Meeting, IEEE, 2014, pp. 21.23. 21-21.23. 24.

[7] C.J. Kirkham, T. Ono, First-Principles Study on Interlayer States at the 4H-SiC/SiO2Interface and the Effect of Oxygen-Related Defects, Journal of the Physical Society of Japan, 85 (2016) 024701.

[8] X.Y. Li, A. Ermakov, V. Amarasinghe, E. Garfunkel, T. Gustafsson, L.C. Feldman, Oxidation induced stress in SiO2/SiC structures, Applied Physics Letters, 110 (2017) 141604.

[9] W. Fu, A. Kobayashi, H. Yano, A. Ueda, S. Harada, T. Sakurai, Investigation of stress at SiO2/4H-SiC interface induced by thermal oxidation by confocal Raman microscopy, Japanese Journal of Applied Physics, 58 (2019) SBBD03.

[10] Y. Sun, S.E. Thompson, T. Nishida, Strain effect in semiconductors: theory and device applications, Springer Science & Business Media, 2009.

[11] J. Singh, Electronic and optoelectronic properties of semiconductor structures, Cambridge University Press, 2007.

[12] Z. Shuai, L. Wang, C. Song, Deformation Potential Theory, in: Theory of Charge Transport in Carbon Electronic Materials, Springer Berlin Heidelberg, Berlin, Heidelberg, 2012, pp. 67-88.

[13] P.A.M. Dirac, The quantum theory of the emission and absorption of radiation, P R Soc Lond a-Conta, 114 (1927) 243-265.

[14] M. Lundstrom, Fundamentals of carrier transport, Cambridge university press, 2009.

[15] H. Tanaka, S. Asada, T. Kimoto, J. Suda, Theoretical analysis of Hall factor and hole mobility in p-type 4H-SiC considering anisotropic valence band structure, Journal of Applied Physics, 123 (2018) 245704.

[16] J. Pernot, S. Contreras, J. Camassel, J.L. Robert, W. Zawadzki, E. Neyret, L. Di Cioccio, Free electron density and mobility in high-quality 4H–SiC, Applied Physics Letters, 77 (2000) 4359-4361.

[17] J. Zhao, V. Gruzinskis, Y. Luo, M. Weiner, M. Pan, P. Shiktorov, E.J.S.s. Starikov, technology, Monte Carlo simulation of 4H-SiC IMPATT diodes, Semiconductor Science and Technology, 15 (2000) 1093.

[18] R. Mickevicius, J.H. Zhao, Monte Carlo study of electron transport in SiC, Journal of Applied Physics, 83 (1998) 3161-3167.

[19] D.J.T.P. Rode, Semiconductors and semimetals, 1975.

[20] W.A. Harrison, Scattering of Electrons by Lattice Vibrations in Nonpolar Crystals, Physical Review, 104 (1956) 1281-1290.

[21] P.N. Butcher, N.H. March, M.P. Tosi, Crystalline semiconducting materials and devices, Springer Science & Business Media, 2013.

[22] W.R. Lambrecht, B. Segall, Band-structure analysis of the conduction-band mass anisotropy in 6H and 4H SiC, Phys Rev B Condens Matter, 52 (1995) R2249-R2252.

[23] D. Volm, B.K. Meyer, D.M. Hofmann, W.M. Chen, N.T. Son, C. Persson, U. Lindefelt, O. Kordina, E. Sörman, A.O. Konstantinov, B. Monemar, E. Janzén, Determination of the electron effective-mass tensor in 4H SiC, Physical Review B, 53 (1996) 15409-15412.

[24] N.T. Son, W.M. Chen, O. Kordina, A.O. Konstantinov, B. Monemar, E. Janzen, D.M. Hofman, D. Volm, M. Drechsler, B.K. Meyer, Electron Effective Masses in 4h Sic, Applied Physics Letters, 66 (1995) 1074-1076.

[25] B.K. Ridley, Quantum processes in semiconductors, Oxford University Press, 2013.

[26] D.K. Ferry, First-order optical and intervalley scattering in semiconductors, Physical Review B, 14 (1976) 1605-1609.

[27] H. Iwata, K.M. Itoh, G. Pensl, Theory of the anisotropy of the electron Hall mobility in n-type 4H– and 6H–SiC, Journal of Applied Physics, 88 (2000) 1956-1961.

[28] B.J.C.U. Van Zeghbroeck, Principles of semiconductor devices, 2004.

[29] J. Singh, Modern physics for engineers, Wiley Online Library, 1999.

[30] A. Pérez-Tomás, P. Brosselard, P. Godignon, J. Millán, N. Mestres, M.R. Jennings, J.A. Covington, P.A. Mawby, Field-effect mobility temperature modeling of 4H-SiC metal-oxide-semiconductor transistors, Journal of Applied Physics, 100 (2006) 114508.

[31] G. Harris, H. Henry, A.J.I.o.E.E. Jackson, INSPEC, London, Properties of Silicon Carbide, edited by GL Harris, 1995.

[32] Y. Kuroiwa, Y. Matsushita, K. Harada, F. Oba, Theoretical prediction of strain-induced carrier effective mass modulation in 4H-SiC and GaN, Applied Physics Letters, 115 (2019) 112102.

[33] T.H. Ning, Y. Taur, Fundamentals of modern VLSI devices, (1998).

[34] Y. Peter, M. Cardona, Fundamentals of semiconductors: physics and materials properties, Springer Science & Business Media, 2010.

[35] Y. Takeda, A. Sasaki, Calculated Electron-Mobility of Two-Dimensional Electrons in Alinas/Ingaas and Inp/Ingaas Single Heterostructures, Jpn J Appl Phys 1, 24 (1985) 1307-1311.

[36] Y. Takeda, A.J.J.j.o.a.p. Sasaki, Calculated electron mobility of two-dimensional electrons in AlInAs/InGaAs and InP/InGaAs single heterostructures, 24 (1985) 1307.

[37] C.J.J. Herring, Bell Syst. Tech. J, 34 (1955) 237.

[38] M. Hofmann, A. Zywietz, K. Karch, F. Bechstedt, Lattice-Dynamics of Sic Polytypes within the Bond-Charge Model, Physical Review B, 50 (1994) 13401-13411.

[39] D.W. Feldman, J.H. Parker, W.J. Choyke, L. Patrick, Phonon Dispersion Curves by Raman Scattering in SiC, Polytypes3C,4H,6H,15R, and21R, Physical Review, 173 (1968) 787-793.

[40] S.B. Lisesivdin, A. Yildiz, N. Balkan, M. Kasap, S. Ozcelik, E. Ozbay, Scattering analysis of two-dimensional electrons in AlGaN/GaN with bulk related parameters extracted by simple parallel conduction extraction method,

Journal of Applied Physics, 108 (2010) 013712.

[41] M. Noguchi, T. Iwamatsu, H. Amishiro, H. Watanabe, K. Kita, S. Yamakawa, Determination of intrinsic phonon-limited mobility and carrier transport property extraction of 4H-SiC MOSFETs, in: 2017 IEEE International Electron Devices Meeting (IEDM), IEEE, 2017, pp. 9.3. 1-9.3. 4.

[42] S. Dhar, S. Haney, L. Cheng, S.R. Ryu, A.K. Agarwal, L.C. Yu, K.P. Cheung, Inversion layer carrier concentration and mobility in 4H–SiC metal-oxide-semiconductor field-effect transistors, Journal of Applied Physics, 108 (2010) 054509.

[43] K. Kamitani, M. Grimsditch, J.C. Nipko, C.K. Loong, M. Okada, I. Kimura, The elastic constants of silicon carbide: A Brillouin-scattering study of 4H and 6H SiC single crystals, Journal of Applied Physics, 82 (1997) 3152-3154.

Chapter 4 Influence of the NAOS buffer layer on ALD-Al_2O_3/NAOS/SiC (Si: as a reference) MOS interface properties

4.1. Introduction

High-temperature thermal oxidation is currently the most widely used method for fabricating SiC-MOS structures. For the ultra-high interface defect density caused by the high-temperature thermal oxidation process[1], researchers have tried many ways, for example, currently, the interfacial nitridation by NO gas post oxidation annealing (POA) treatment is the most effective interface passivation method[2, 3]. However, after the NO POA treatment, the interface defect density is still higher than 10^{13} cm^{-2} eV^{-1}, indicating it is unable to eliminate the interface traps completely. The surface passivation method using an ultrathin SiO_2 layer formed by nitric acid oxidation of Si (NAOS) has attracted considerable attention in the field of solar cells and semiconductor devices [4]. The use of the NAOS as an oxide layer to improve interface properties has been maturely applied to Si solar cells since the NAOS layer was found to effectively passivate the SiO_2/Si interface by decreasing the interface states density to increase the carrier lifetime[4-6]. In addition, NAOS is a low-temperature oxidation process. Thus, it can effectively eliminate the generation of interfacial stress caused by high temperatures. Therefore, we expect to apply the passivation effect of the NAOS layer at the SiO_2/Si interface to the SiO_2/SiC interface. However, the problem for the NAOS is that the dielectric breakdown strength is as low as 1 MV/cm. For a power device, it needs a breakdown strength of 6 MV/cm or more. Al_2O_3 exhibits a high dielectric breakdown strength of ~ 10 MV/cm[7, 8]. In addition, the band offsets are suitable (ΔEc = 1.5-1.7 eV and ΔEv = 1.2 eV, respectively, for 4*H*-SiC)[9, 10] as SiC-MOS dielectric layer material compared to ZrO_2 or HfO_2.[11] However, during the ALD process, the generation of suboxide layer with low density have been found at the interface of the Al_2O_3 and Si substrate, as shown in Figure 4.1, leads to a higher interface traps density (D_{it}) compared to that of SiO_2/Si interface.[12] Comparing the characteristic between NAOS and ALD-Al_2O_3, we found that NAOS can provide a low-stress interface and low interface traps density, but not a high dielectric breakdown strength, while ALD- Al_2O_3 can provide a high dielectric strength but not a low interface trap density. Thus, we used the NAOS layer as a buffer layer between the ALD- Al_2O_3 oxide layer and SiC substrate, expecting to fabricate a SiC-MOS structure with low interface stress, low interface traps density, and high dielectric breakdown strength.

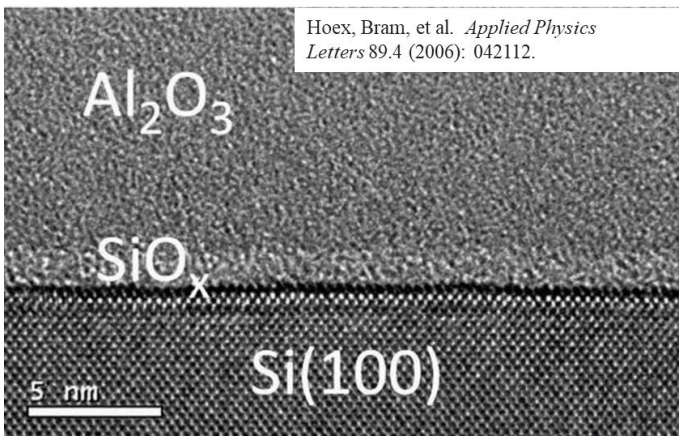

Figure 4.1 TEM image showing the generation of suboxide layer at the interface of Al_2O_3 and Si substrate [12]

In this chapter, we first fabricated the SiO_2/SiC structure using nitric acid oxidation of SiC at a low temperature. Then, an atomic layer deposition (ALD) Al_2O_3 layer is deposited on the NAOS layer to form a double oxide layer to improve the electrical properties of the SiC-MOS structure further. After that, we evaluated the interface passivation effect of the NAOS buffer layer by different annealing temperatures.

4.2. Experiment

4.2.1 The manufacturing method of the oxide film

4.2.1.1 Nitric acid oxidation of SiC (NAOS)

The formation of ultrathin SiO_2 by nitric acid (HNO_3) oxidation of the SiC method at 120 ℃ has been reported by Kobayashi et al. [13]. Chemical oxide films have been used in the semiconductor industry. In chemical solutions widely used in semiconductor factories, SiO_2 films formed using nitric acid (especially azeotropic nitric acid) show excellent electrical characteristics[14]. Azeotropic nitric acid is nitric acid with the same gas and liquid composition at the highest boiling point, as shown in the phase diagram in Figure 4.2[15, 16]. We can see that when 68 wt% HNO_3 is boiling at 120 ℃, the liquid and gas phases have the same concentration, which means we can have stable oxidation at the azeotropic states of the HNO_3 solution. In the azeotropic state of HNO_3 solution, nitric acid reacts with H_2O in the mixed solution and ionizes as follows to produce NO_3^-:

$$HNO_3 + H_2O \rightarrow NO_3^- + H_3O^+, \quad (4.1)$$

This NO_3^- ion decomposes on the SiC surface and produces O^- ion, which acts as a powerful oxidizing species, causing oxidation at low temperatures.

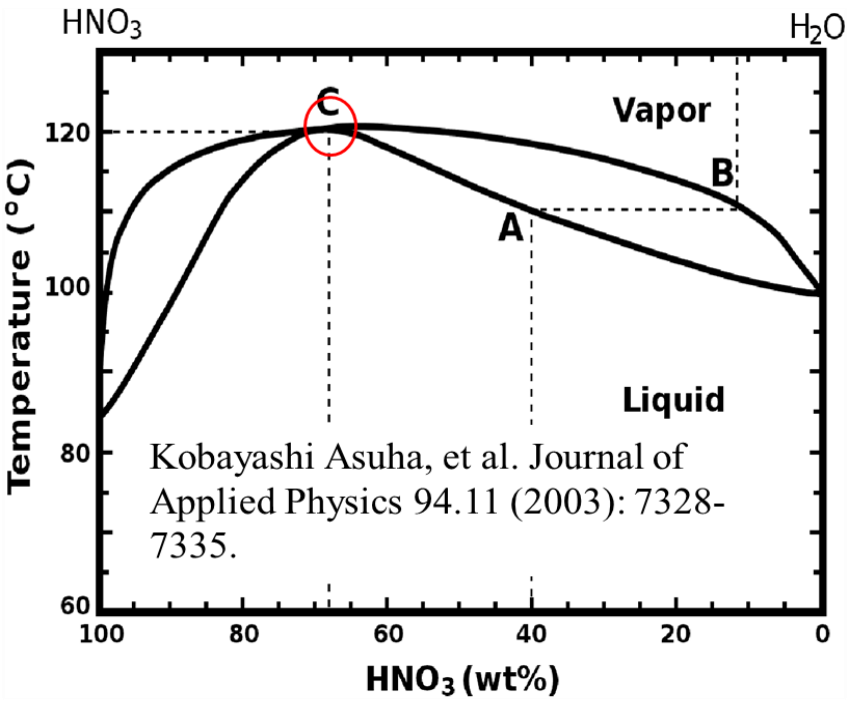

Figure 4.2 Phase diagram of HNO_3 and water system [13]

$Si^{2+} + 2O^{-} \rightarrow SiO_2$, (4.2)

4.2.1.2 Atomic layer deposition (ALD)[17, 18]

In the air, a hydroxyl group is formed: Si-O-H since H_2O vapor is adsorbed on the SiC surface. After setting the substrate in the reactor, trimethylaluminum (TMA) was jetted into the reaction chamber (Figure 4.3 (a)). TMA reacts with adsorbed hydroxyl groups until the surface is passivated. Since TMA does not react with itself, this stops the reaction in one layer, ensuring a perfect uniformity of ALD. The excess TMA and the methane reaction products are pumped away (Figure 4.3 (b)). After that, water vapor (H_2O) is jetted into the reaction chamber and reacts with the methyl groups suspended on the new surface to form aluminum-oxygen (Al-O) bridges and hydroxyl surface groups. The chemical reaction is shown in the expression (4.3), waiting for a new TMA pulse (Figure 4.3 (c)). Again, methane is a reaction product and will be pumped away. Since the excess H_2O vapor does not react with the hydroxyl surface groups, perfect passivation of an atomic layer is still produced. (Figure 4.3 (d)). One TMA and one H_2O vapor pulse form one cycle, two reaction steps in each cycle are given by expression (4.4) and (4.5). Using the setting parameters in Table 4.1, we obtain the deposition rate with approximately 1 Angstrom per cycle in our experiment.

$2H_2O + :\mathrm{Si} - \mathrm{O} - \mathrm{Al}(CH_3)_2 \rightarrow :\mathrm{Si} - \mathrm{O} - \mathrm{Al(OH)}_2 + 2CH_4$, (4.3)

$\mathrm{Al}(CH_3)_3 + :Al - O - H \rightarrow :\mathrm{Al} - \mathrm{O} - \mathrm{Al}(CH_3)_2 + CH_4$, (4.4)

$2H_2O + :\mathrm{O} - \mathrm{Al}(CH_3)_2 \rightarrow :\mathrm{Al} - \mathrm{O} - \mathrm{Al(OH)}_2 + 2CH_4$, (4.5)

Table 4.1 Setting parameters of ALD

Setting parameters			
TMA Pulse time	0.1 sec	H_2O Pulse time	0.3 sec
TMA Purge time	4.0 sec	H_2O Pulse time	6.0 sec
TMA Line flow	150 sccm	H_2O Line flow	150 sccm

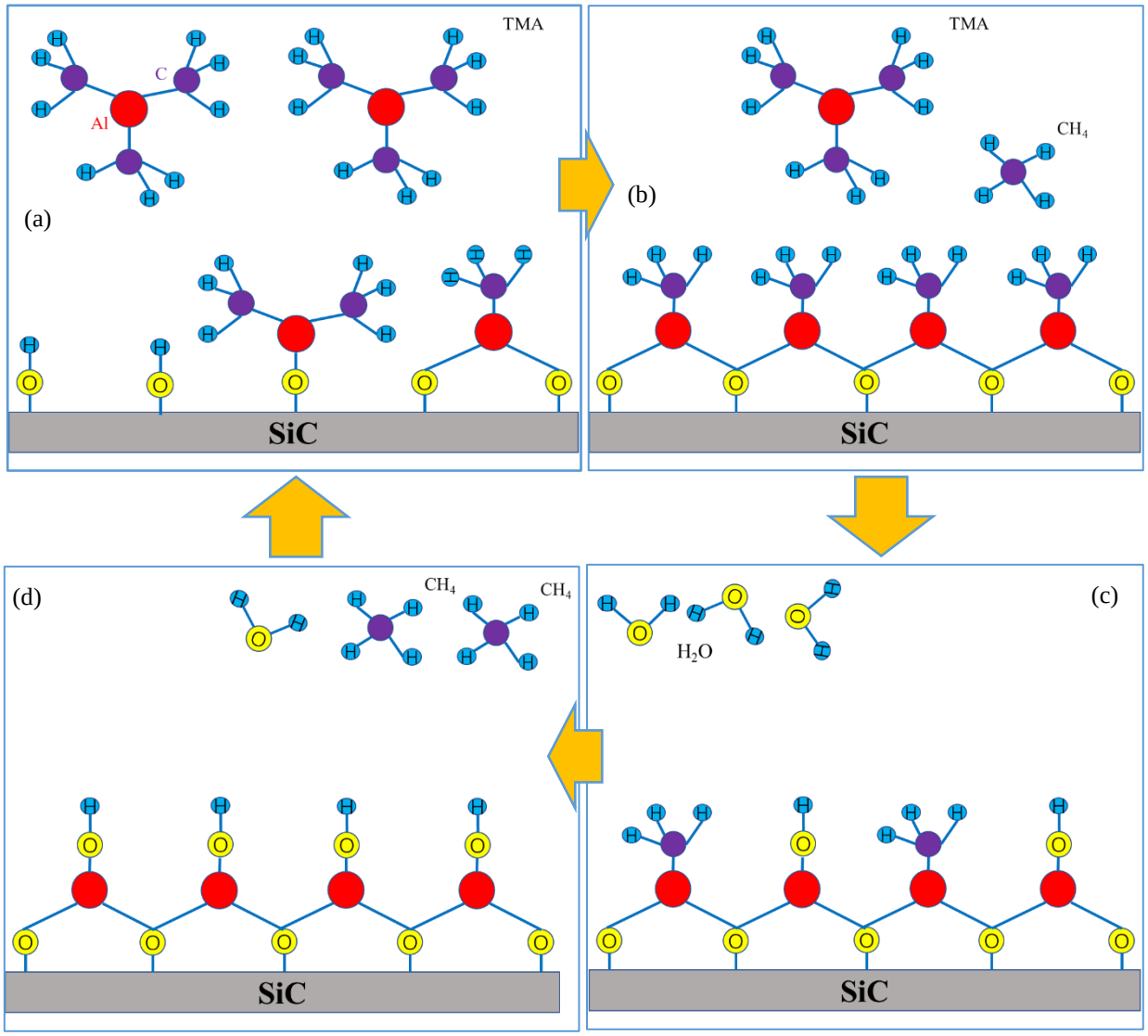

Figure 4.3 Principle of ALD (atomic layer deposition) method. (a) TMA supply, (b) excess TMA and methane purge, (c) H_2O supply, and (d) excess H_2O and methane purge

4.2.2 Fabrication details

For the experiment, n-type 4H-SiC (0001) wafers with a thickness of 350 μm were used. The n-type SiC wafers have an epitaxial layer with a thickness of 11.2 μm, dopant concentration of $6.2 \times 10^{15} cm^{-3}$ and resistivity of 0.017 Ω·cm. Before the growth of the NAOS layer, the wafers were cleaned using the RCA method to assure a hydrophobic surface, followed by etching with a 5 % hydrofluoric acid (HF) solution to remove the chemical oxide layer. Then, the samples were then divided into two groups: (a) The cleaned wafers were immersed in 68 wt % HNO_3 solutions at 115 ± 5 ℃ for 1_20 min. The thickness of the NAOS SiO_2 layer was estimated to be 2-2.5 nm by ellipsometry. The samples were then annealed at 400 and 800 ℃ for 120 min in an N_2 atmosphere. Next, a 50 nm-thick film of Al_2O_3 was deposited by thermal atomic layer deposition (ALD) on the NAOS layer. As a control group, the samples in the group (b) were directly deposited in an ALD layer with the same thickness as the samples in the group (a) without growing a NAOS layer. The triethylaluminium (TMA) and water (H_2O) were used as reactants in the ALD process. The substrate temperature during deposition was set to 300 ℃. After being coated with Al_2O_3, both groups, the samples were annealed at 450, 500, 550, 600, and 650 ℃ for 30 min in an N_2 atmosphere.

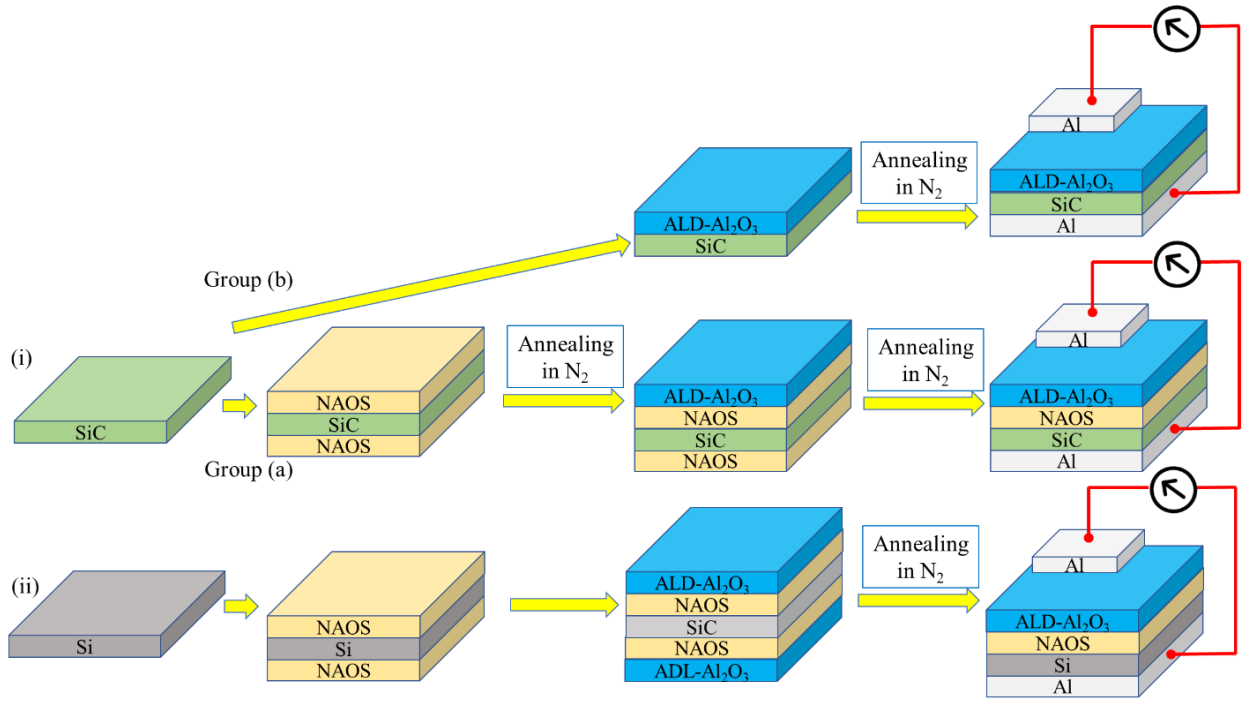

Figure 4.4 Fabrication procedure of (i) the 4H-SiC substrate samples, (ii) Si-substrate samples

Before experimenting on 4H-SiC, we conducted a pilot experiment on Si wafer. Magnetic-field applied CZ (MCZ) p-type Si (100) wafers have a resistivity of 8~10 Ω·cm with a thickness of 500 μm were used. After cleaning the Si wafers using the same method with SiC wafer, the wafers were immersed in 68 wt% HNO3 solutions at 80 ℃ for 30 min to grow a NAOS layer with a thickness of 1-1.5 nm. Next, a 50 nm-thick film of Al_2O_3 was deposited by ALD on both sides of the Si substrate with the NAOS layer. After being deposited with Al_2O_3, the samples were annealed in an N_2 atmosphere. The sample fabrication procedure was shown in Figure 4.4. MOS capacitors have also been fabricated using 4H-SiC and Si substrates to carry out the C-V measurement on the samples. Al was used for the backside ohmic contact and the gate

electrode with diameters of 100, 300, and 500 μm. The sample information was summarized, as shown in Table 4.2 (1) and (2).

Table 4.2 (1) Samples information in our experiment

4H-SiC	NAOS			Annealing after NAOS			ALD	Annealing after ALD		
	HNO_3 (wt%)	Temperature (℃)	Immersed time(min)	N/A	400 ℃	800 ℃		300 ℃	450 ℃	600 ℃
Group a	68	115 ± 5	120	○	○	○	○	○	○	○
Group b	**X**			**X**	**X**	**X**	○	○	○	○

Table 4.2 (2) Samples information in our experiment

	NAOS			Annealing after NAOS	ALD	Annealing after ALD process				
Substrate	HNO_3 (wt%)	Temperature (℃)	Immersed time (min)			450	500	550	600	650
Si	68	80	30	**X**	○	○	○	○	○	○

4.2.3 Characterization methods

The minority carrier lifetime (τ_{eff}) was characterized by using Quasi-Steady-State Photoconductance (QSSPC). In addition, the capacitance-voltage (C-V) measurements were carried out, and a metal-oxide-semiconductor (MOS) model was used to determine the density of fixed charge (Q_f) and the density of interface trap (D_{it}) at the Al_2O_3/NAOS/Si interface. Thus, we could distinguish the contributions of the field-effect and chemical passivation of the Al_2O_3/NAOS films. In addition, since we cannot use the method of measuring the carrier lifetime by the QSSPC method to evaluate the passivation effect of the SiC surface, Photoluminescence (PL) was employed in our experiment.

4.2.3.1 Quasi-steady state photoconductance (QSSPC)

Quasi-steady state photoconductance method, a lifetime is calculated by detecting the time dependence of the photoconductivity of a sample while emitting a flash lamp onto the sample (the sample is always in a pseudo-steady state). The general expression for the quasi-state photoconductance measurements of effective carrier lifetime is given as[19]

$$\tau_{eff} = \frac{\Delta n_{ave}}{G_{ave}(t) - \frac{\partial \Delta n_{ave}(t)}{\partial t}}, \quad (4.6)$$

Here, $n_{ave}$is the average excess carrier density and G_{ave} is the average generation rate. Both are calculated over the entire thickness of the wafer. Therefore, to determine the effective lifetime, we must confirm the time dependence of the excess carrier density and generation rate in the test sample. Excess carrier density can be monitored directly by photoconductivity. QSSPC is a technology used explicitly for inductively coupled quasi-steady-state photoconductive life detection. [20]

$$\Delta n_{ave}(t) = \frac{\Delta\sigma(t)}{q(\mu_n+\mu_p)D}, \quad (4.8)$$

Where $\Delta\sigma(t)$ the excess photoconductivity of the test sample, which is time-dependent, μ_n and μ_p are the electron and hole mobilities, and D is the sample thickness. I_{ave} is the illumination intensity measured from the calibrated reference sample, and It is used to measure the number of photons incident on the surface of the sample. Since any real sample can only partially absorb these available photons, the absorption portion can be expressed as f_{abs}. Thus, the generation rate within the sample can be identified as

$$G_{ave}(t) = \frac{I_{ave}(t) f_{abs} N_{ph}^{1sun}}{D}, \quad (4.9)$$

Where N_{ph}^{1sun} is the luminous flux of a photon in sunlight when the irradiance is one sun, which generates an electron-hole pair in the sample. Therefore, to sum up, if those required quantities in Equation (4.6) can be measured experimentally, the effective carrier lifetime is likely to be determined.

The measured minority carrier lifetime is an effective lifetime under multiple independent composite mechanisms. The actual measurement obtained is the minority carrier lifetime of the interaction of bulk recombination and surface recombination. If the carrier concentration is uniformly distributed in the semiconductor. We can obtain the expression of the effective minority carrier lifetime, τ_{eff} as

$$\frac{1}{\tau_{eff}} = \frac{1}{\tau_{intrinsic}} + \frac{1}{\tau_{SRH}} + \frac{1}{\tau_{surface}} = \frac{1}{\tau_{SRH}} + \frac{1}{\tau_{Auger}} + \frac{1}{\tau_{rad}} + \frac{1}{\tau_{surface}} = \frac{1}{\tau_{bulk}} + \frac{1}{\tau_{surface}}, \quad (4.10)$$

where, $\tau_{intrinsic}$ is the intrinsic lifetime of the semiconductor, including Auger and Radiative recombination life, and τ_{SRH} is the minority carrier lifetime caused by defect recombination centers in the material according to the Shockley-Read-Hall model[21]. Because in this work, we focus on the surface repair process, we can think that the nature of the material body has not been changed. Therefore, as in Equation (4.10), the effective carrier lifetime measured by QSSPC can be considered as a change in the surface state of the SiC.

4.2.3.2 Capacitance-Voltage characteristics (*C-V*)

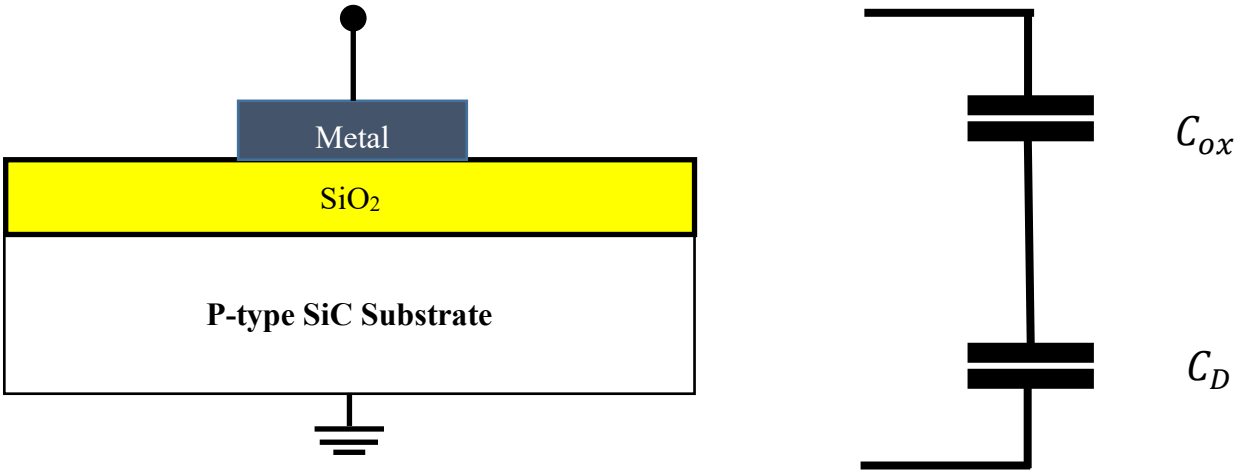

Figure 4.5 Schematic of the MOS structure used in *C-V* measurement, and high frequency equivalent circuits of the MOS capacitor

The method, comparison of the measured high-frequency capacitance with a theoretical capacitance with no interface traps, developed by Terman[22] improved by Brews[23], was used to extracting interface trap level density from the *C-V* measurement results of 4H-SiC MOS diodes in this work. As shown in Figure 4.5, at high frequencies, interface states are unable to follow variations in the Fermi level, thus, the high-frequency capacitance C_{HF} of the MOS capacitor is given by

$$C_{HF} = \frac{C_{ox}C_D}{C_{ox}+C_D}, \quad (4.11)$$

since interface traps do not respond to ac gate voltage in a high-frequency *C-V* measurement, interface traps contribute no capacitance to the high-frequency *C-V* curve. In theory, the ideal and actual high-frequency *C-V* curve should be identical, the change of total charge in the metal electrode induced by applying gate voltage should equal to the change of total charge in the semiconductor, $\Delta Q_G = -\Delta Q_s$. However, since interface trap occupancy must be changed in addition to evolving depletion layer charge, when interface traps do follow with the changes in the gate bias, the evolution of total charge in the metal electrode should equal to the change of total charge in the semiconductor plus the change of charge due to the interface traps, $\Delta Q_G = -(\Delta Q_s + \Delta Q_{it})$. In this case, to obtain the MOS capacitor requires a broader range of gate charge variation for the case with interface traps, than for that without interface traps, $\Delta V_G = \Delta Q_G / C$, which causes

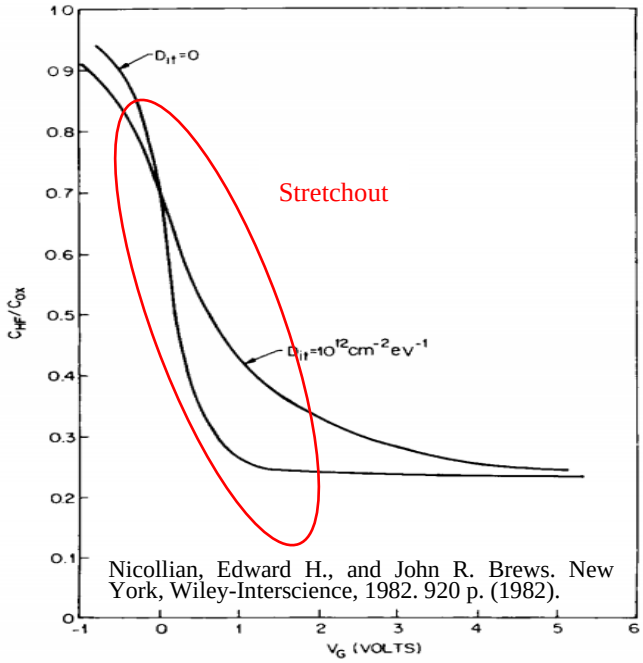

Figure 4.6 Theoretical high frequency *C-V* curve with interface trap stretchout compared to a theoretical C-V curve, with no interface traps. Parameters: $N_D = 10^{15}cm^3, d_o = 100nm, and\ D_{it} = 10^{12}cm^{-2}eV^{-1}$

the high-frequency *C-V* curve to stretch out along the gate bias axis, as shown in Figure 4.6. thus, the interface trap density D_{it} can be extracted by comparing the measured high-frequency *C-V* curve with a theoretical ideal curve. The specific extraction method is shown below:

(1) The relationship between C_{it} and D_{it} is derived as follows. Based on the interface trap density distribution, $dQ_{it} = qD_{it}\,dE$, and $dE = qd\Psi_s$, we obtain

$$C_{it} = \frac{dQ_{it}}{d\Psi_s} = q^2 * D_{it}, \quad (4.12)$$

(2) The circuit in Figure 4.7 (right) does not include a trap capacitor. Therefore, regardless of the density of the interface trap, the high-frequency capacitance of the MOS capacitor will be the same as the ideal capacitor without the interface trap, that is, the same as Cs. However, Cs changes with the band bending Ψ_s. Therefore, if the band bending is not the same, the measured C_{HF} will be different from the ideal value, as shown in Figure 4.7 (left). If we know the $\Psi_s$corresponding to a given C_{HF} in an ideal MOS capacitor and measure the V_G corresponding to the same C_{HF} in an actual MOS capacitor, we can construct a relationship curve between Ψ_s and V_G for a MOS capacitor with an interface trap. As shown in figure 4.8, The surface potential Ψ_s corresponding to each gate voltage V_G is obtained from the experimental capacitance value, and the V_G - ($d\Psi_s/dV_G$) characteristic is derived from the V_G-Ψ_s characteristic.

(3) Based on the relationship between V_G and Ψ_s, the derivative $\frac{d\Psi_s}{dV}$ is found. Then the interface traps capacitor C_{it} can be obtained as

$$C_{it}(\Psi_s) = C_{ox}\left[\left(\frac{d\Psi_s}{dV}\right)^{-1} - 1\right] - C_s, \text{ (4.13)}$$

We can obtain the D_{it} form Eqs. (4.12) and (4.13)

$$D_{it} = \frac{C_{ox}}{q^2}\left[\left(\frac{d\Psi_s}{dV}\right)^{-1} - 1\right] - \frac{C_s}{q^2}, \text{ (4.14)}$$

In actual calculations, the derivative term was expressed as $\left(\frac{d\Psi_s}{dV}\right)^{-1} = \frac{\Delta V_{measured} - \Delta V_{theory}}{\Delta\Psi_s}$, V_{theory} is the theoretical voltage which is corresponding to the ideal gate-source bias, $V_{measure}$ is the applied gate voltage which corresponds to the applied gate-source bias for the same value of capacitance, and Ψ_s is the surface potential. Using the Eq. (4.14), we can plot interface trap density as a function of energy levels.

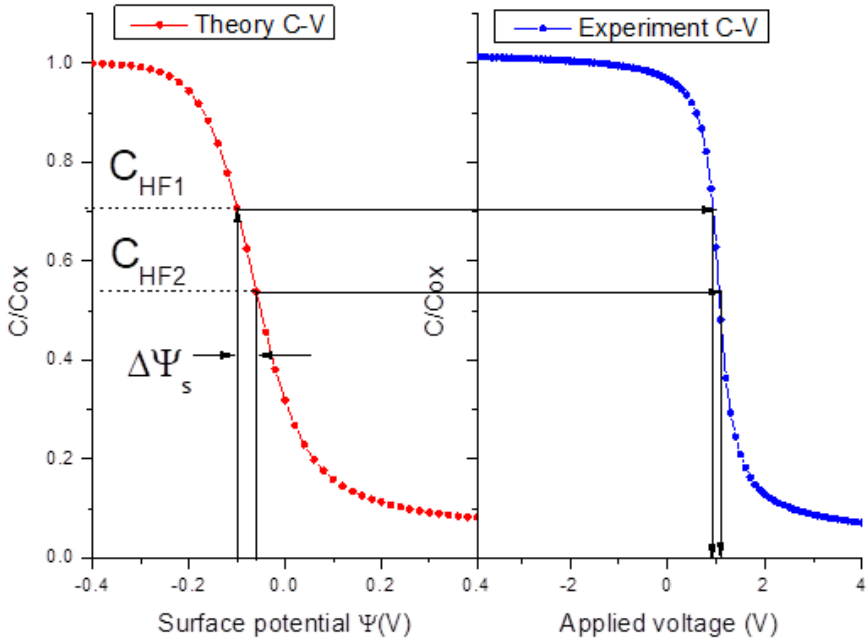

Figure 4.7 Theoretical C_{HF} versus Ψ_s plot compared with a hypothetical C_{HF} versus V_G plot for an MOS capacitor with interface trap

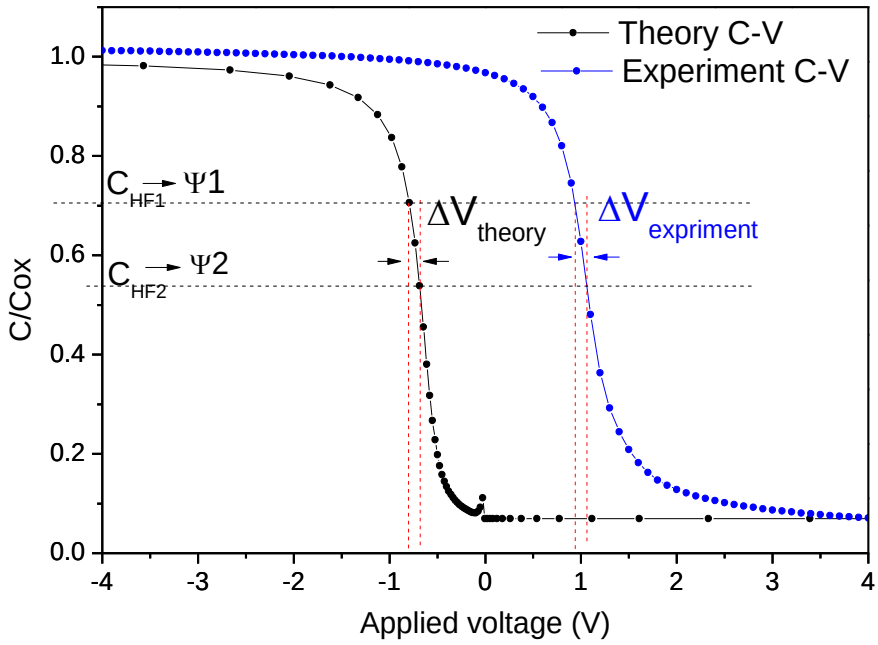

Figure 4.8 Theoretical *C-V* curve compared with a hypothetical *C-V* curve for an MOS capacitor with interface trap

4.2.3.3 Photoluminescence (PL)

The surface passivation effect at the ALD-Al_2O_3/NAOS/SiC interface was evaluated by photoluminescence (PL) in this work. Photoluminescence (PL) spectroscopy is a non-destructive technique used to study material properties, including bandgap energy, electronic defects, recombination properties, and the general optical quality of materials. When the photon energy of the incident light is higher than the bandgap of the material, the photons will be absorbed, and create electronic excitations. These electronic excitations will eventually relax and return to the ground state. During this process, if radiation relaxation occurs, the light emitted is called photoluminescence (PL).

For 4H-SiC, Photoluminescence (PL) is not a commonly used method for surface or interface property evaluation. Since 4H-SiC has a wide forbidden bandgap of about 3.26 eV, a higher energy incident light source is required. However, since the absorption coefficient of 4H-SiC is very low, when an incident light with short-wavelength incidents in the surface of 4H-SiC, resulting in considerable penetration depth. Therefore, it is difficult to distinguish between bulk and surface recombination. On the other hand, 4H-SiC is an indirect bandgap semiconductor, so the PL signal of SiC is weak. Therefore, in many cases, we cannot detect the PL signal of SiC. However, in this work, the PL intensity can be used to evaluate the surface passivation effect of SiC samples. The reasons are as follows,

The recombination processes are measured as the recombination lifetime τ, which is defined by

$$\tau \equiv \frac{\Delta n}{U}, \quad (4.15)$$

where Δn is the excess carrier concentration, and U is the recombination rate per volume.

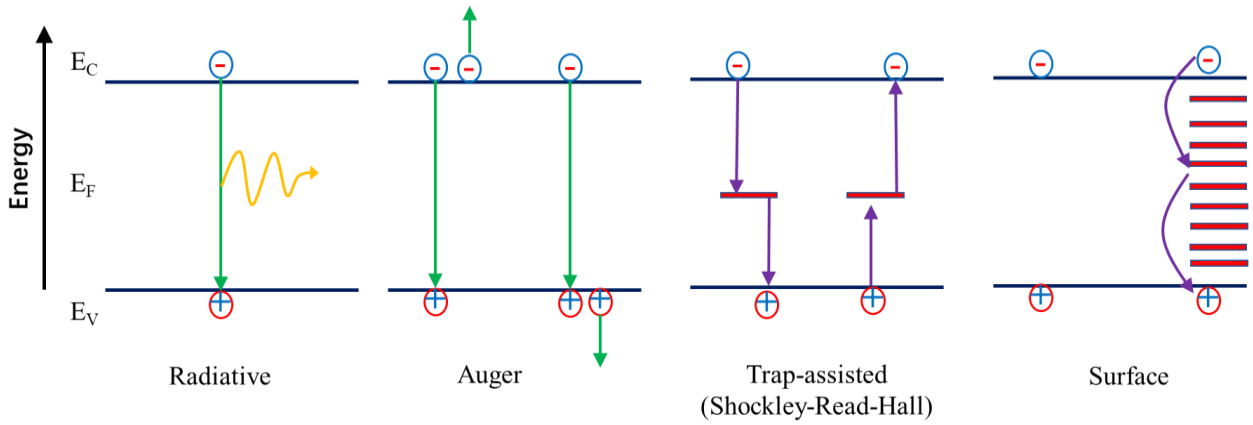

Figure 4.9 Schematic of the recombination mechanisms in semiconductors.

Auger and Radiative recombination are two kinds of intrinsic recombination mechanisms. They are independent of the material quality. Thus, in this work, their contribution to the total effective lifetime can be regarded as constants. The dynamics of the recombination process through defect states in the bandgap, as shown in figure 4.9, was called Shockley-Read-Hall (SRH) recombination. Based on the SRH theory, we can obtain the recombination rate caused by a defect with concentration N_t with a single energy level E_t by

$$U_{SRH} = \frac{np - n_i^2}{\tau_{p0}(n+n_1)+\tau_{n0}(p+p_1)}, \quad (4.16)$$

where τ_{n0} and τ_{p0} are the electron and hole capture time constant, defined as

$$\tau_{n0} = \frac{1}{\sigma_n N_t v_{th}}, \quad \tau_{p0} = \frac{1}{\sigma_p N_t v_{th}} \quad (4.17)$$

here, σ_n and σ_p are the capture cross-section for electrons and holes, respectively, and v_{th} is the carrier thermal velocity. n_1 and p_1 are statistical factors. An extended SRH formalism described the surface recombination rate. Using the interface state density per energy interval $D_{it}(\varepsilon)$ to replace the single energy level E_t. The total surface recombination rate is given by integrating the SRH recombination rate over the bandgap:

$$U_{surface} = (n_s p_s - n_i^2) v_{th} \int_{E_v}^{E_c} \frac{D_{it}(\varepsilon)}{\frac{n_s+n_1(\varepsilon)}{\sigma_p(\varepsilon)}+\frac{p_s+p_1(\varepsilon)}{\sigma_n(\varepsilon)}} d\varepsilon, \quad (4.18)$$

where n_s and p_s are the electron and hole concentrations at the surface.

The total recombination rate can be presented as

$$U_{total} = U_{bulk} + U_{surface}, \quad (4.19)$$

as mentioned before, the $U_{bulk} = U_{rad} + U_{Aug} + U_{SRH}$, in addition, based on the equation (4.18), the total recombination rate be represented as

$$U_{total} = U_{rad} + U_{Aug} + U_{SRH} + (n_s p_s - n_i^2) v_{th} \int_{E_v}^{E_c} \frac{D_{it}(\varepsilon)}{\frac{n_s + n_1(\varepsilon)}{\sigma_p(\varepsilon)} + \frac{p_s + p_1(\varepsilon)}{\sigma_n(\varepsilon)}} d\varepsilon, \quad (4.20)$$

As we knew, Surface passivation is the act of reducing the SRH at the wafer surface. From equation (4.20), it is clear that the recombination rate U_{SRH} is the main factor for the total recombination. The photoluminescence (PL) signal results from the radiative recombination process in the optically excited semiconductor. Based on Eqs. (4.18), (4.19), and (4.20). We can see that the D_{it} enhances nonradiative recombination, which results in the reduction of PL intensity. Thus, we can consider that the density of the interface traps is proportional to the recombination rate, which also corresponds to the PL intensity. Therefore, when we only treat the surface of the sample, we can consider that the change in the recombination rate of the surface is the most critical factor affecting the PL intensity change. Therefore, in this work, PL intensity can be considered as an effective method for evaluating the surface characteristics of the SiC substrate. So, we tried to evaluate the interface properties by using the PL measurement.

In this work, the PL experiments were carried out at Wide Bandgap Semiconductor Group Lab., in National Institute for Materials Science (NIMS), Japan. Using a LabRamHR-PL NF(UV-NIR) microscopy-PL measurement system with an excitation laser wavelength of 325 nm. The SiC-MOS samples are the same as those used in the confocal Raman test in Chapter 2. They were annealed in a NO ambient at 1250 ° C for 0, 10, 60, and 120 min after dry oxidation. Figure 4.10 shows the interface trap density distribution of the samples annealed at different temperatures[24] and the PL spectra of those samples obtained by our PL measurement. We observed that the PL intensity basically reflects the trend of the density of interface traps change.

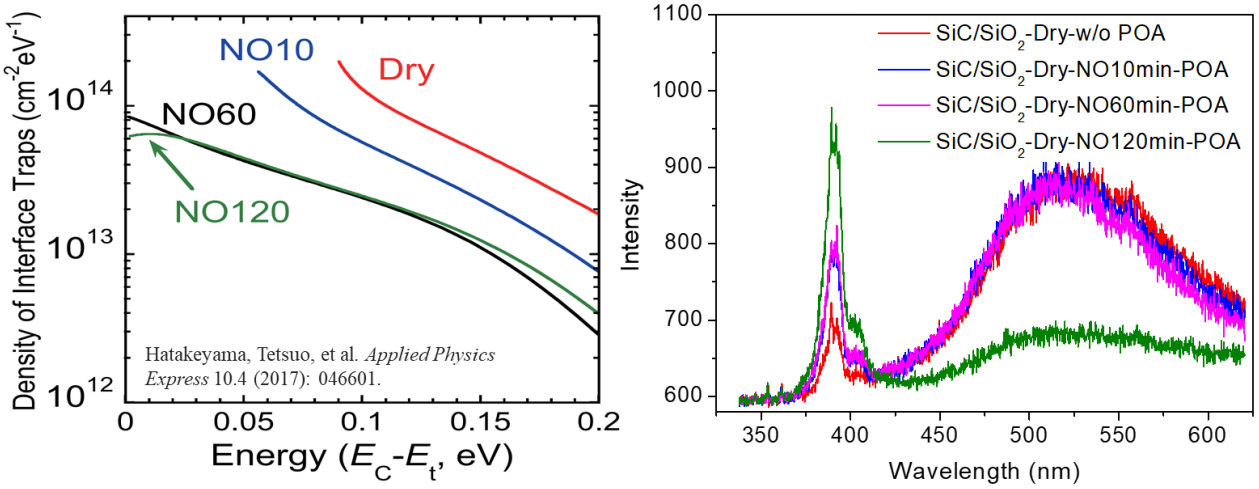

Figure 4.10 Interface trap density distribution of the samples annealed at different temperatures (left), PL spectra measured on those samples (right).

4.3. Discussion and Conclusion

4.3.1 The effect of the NAOS buffer layer on ALD-Al_2O_3/NAOS/Si MOS interfaces

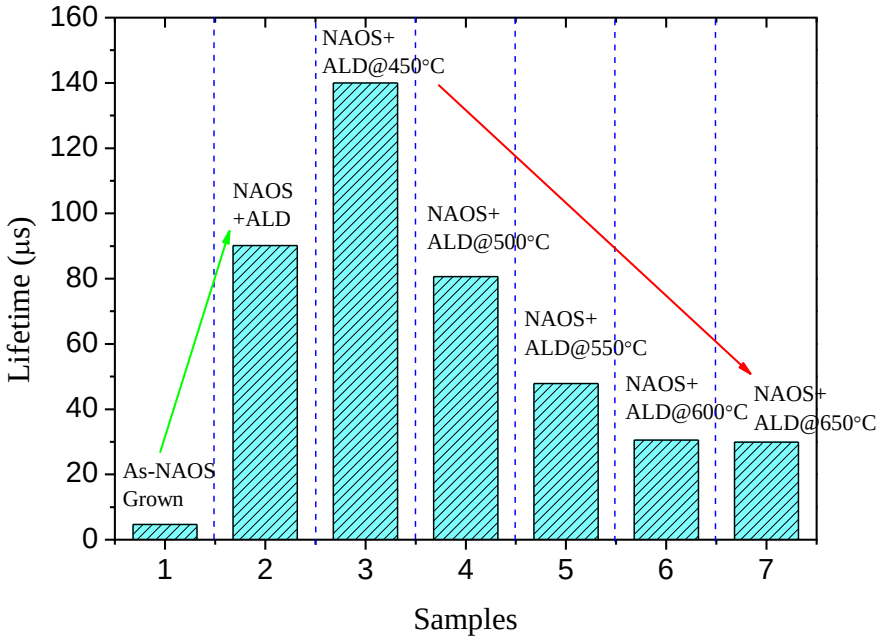

Figure 4.11 Comparison of minority carrier lifetime of <Al_2O_3/NAOS/Si/Al_2O_3> structure, after the NAOS layer growth, after the deposition of ALD Al_2O_3, and after annealing at different temperatures.

To investigate the effect of the NAOS buffer layer on <ALD-Al_2O_3/NAOS/SiC> MOS interface properties, we first evaluated that on the <Al_2O_3/NAOS/Si> MOS structure. Figure 4.11 shows the effective minority carrier lifetimes of Al_2O_3/NAOS/Si samples after the NAOS layer growth, after the deposition of ALD Al_2O_3, and after annealing at different temperatures. We observed that the effective minority carrier lifetimes of all samples were increased to around 90 μs after the deposition of ALD layers. A further improvement of carrier lifetime to 140 μs after the sample was annealed at 450 ℃

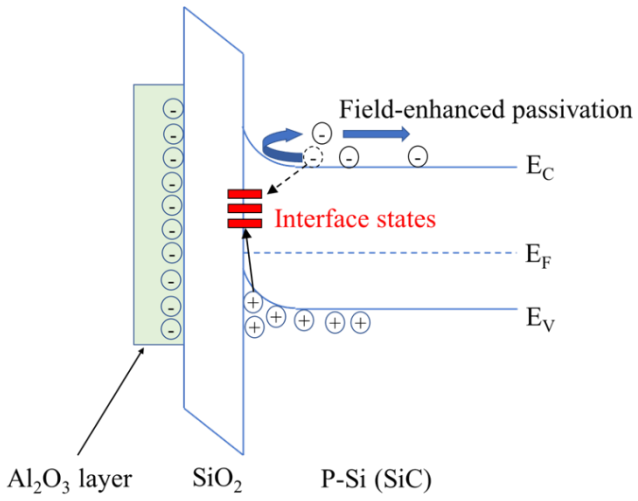

Figure 4.12 Field-enhanced passivation induced by the band bending under influence of fixed charge Q_f.

is noticed. These results can be explained from the reduction in the recombination at the interface due to the field-enhanced passivation, as shown in Figure 4.12. After annealing treatment, as the density of the fixed negative charges at the interface increases, the electric field strength formed at the Al_2O_3 / NAOS / Si interface increase, thereby further reducing the electron density near the interface and reducing the interface recombination rate.[25, 26].

However, for annealing temperature higher than 500 ℃, the minority carrier lifetime decreases sharply with an increment of temperature. In order to understand the reason for this reduced life, the samples annealed at 450, 500 and 650 ℃ were selected to be fabricated into MOS capacitors and carried out C-V measurement to evaluate the electrical properties of their interfaces. Figure 4.13 shows a comparison between experimentally measured and ideal C-V curves after annealing at different temperatures. Based on the flat band voltage offset (V_{BF}), we calculated the corresponding fixed charge density in the oxide layer. We observed that as the annealing temperature increases, the negative fixed charge density of the oxide layer increases. Previous studies have shown that the negative fixed charge in the oxide layer will have an electric-enhanced effect on the p-type substrate, resulting in a reduced probability of carrier recombination, thereby enhancing carrier lifetime. Moreover, the higher the fixed charge density, the stronger the interface passivation effect.[27]. However, comparing fixed charge density and carrier lifetime in Table 4.1, we observed that the carrier

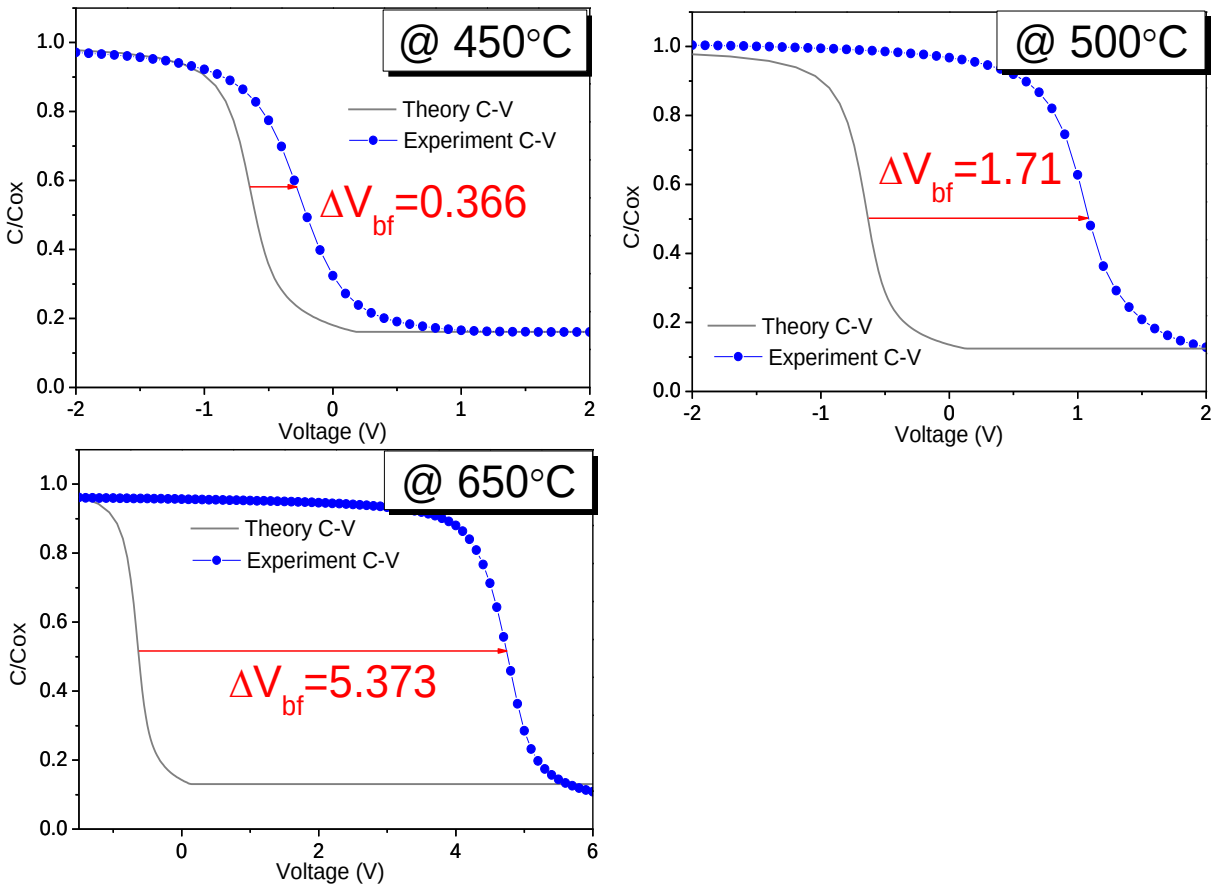

Figure 4.13 Comparison between the experimentally measured CV curve and the ideal CV curve after annealing at different temperatures.

lifetime of the Al_2O_3/NAOS/Si films decreases with increasing density of fixed charge. Therefore, we believe that the

field-enhanced effect from the ALD-Al_2O_3 layer has little effect on the carrier lifetime.

Table 4.1 Minority carrier lifetime τ_{eff} , the flat band voltage shift V_{FB}, and density of fixed charges Q_f obtained from the annealed Al_2O_3/NAOS combination layer at indicated annealing temperatures.

Annealing temperature	V_{FB} (V)	Q_f 10^{12} (cm^{-2})	τ_{eff} (μs)
450 ℃	0.366	-1.2569	140
500 ℃	1.71	-6.1722	81
650 ℃	5.373	-18.666	30

For the real reason for the reduced carrier lifetime, we hypothesize that the reduction of the effective minority carrier lifetimes may be affected by the density of states at the interface. Thus, we extracted the distribution of interface trap density using the Termann method. The D_{it} values were estimated from the difference of the theoretical C-V curve of the ideal MOS and the experimental C-V curve at high frequency using equation (4.14). Based on the calculated D_{it}, as shown in figure 4.14. It is clear that annealing at high temperatures resulted in high D_{it} values at a deep energy level. S. Zaima et al. have discovered this strong dependence between deep defect density and oxidation.[28].So, the critical question now is what causes the high trap density at deep levels. Asuha et al.[29] have found that the high annealing temperature enhances the interface diffusion, Al ion may diffuse into the NAOS layer to react with the SiO_2, reducing the density of

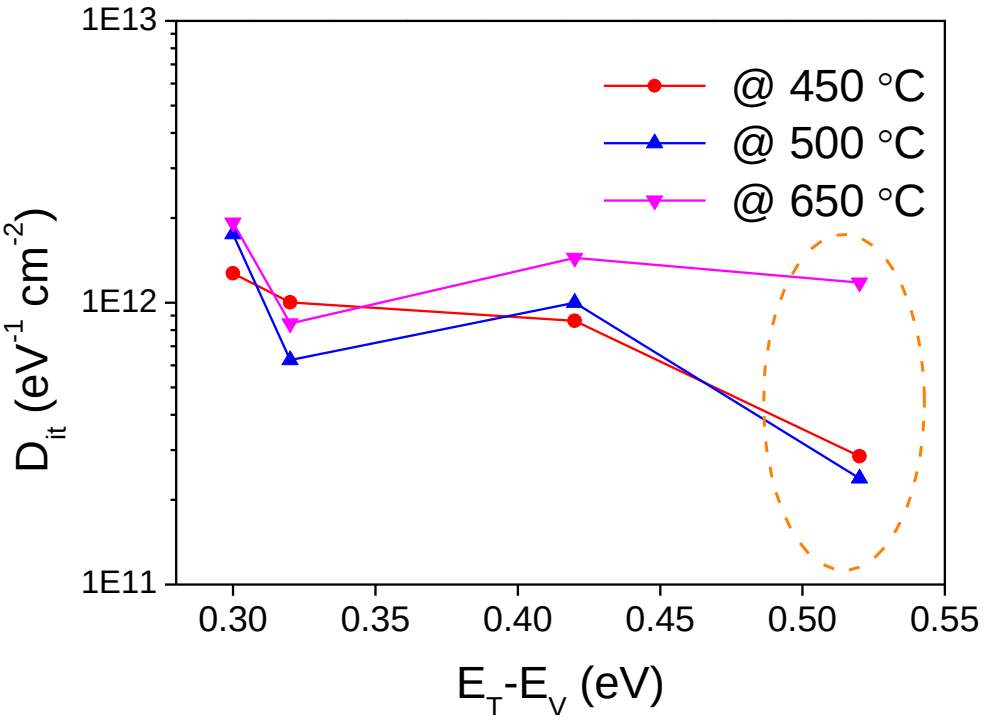

Figure 4.14 Interface state density D_{it} as a function of energy position in the silicon bandgap.

SiO_2 which leads to a high interface traps density. In addition, as shown in figure 4.15, the reaction induced the thickness change of NAOS has been found could enhance the effect of the the negative fixed charge density.[30] Fortunately, this interfacial diffusion process can be effectively reduced by proper annealing treatment.

In the case of the <Al_2O_3/NAOS/Si> MOS structure, the critical finding is that an annealing treatment is significant for the NAOS layer to improve its quality to reduce the inter-diffusion in the MOS structure. Based on the conclusion, for the <Al_2O_3/NAOS/SiC> MOS structure, we focused on the interface passivation effect of the NAOS buffer layer by different annealing temperatures.

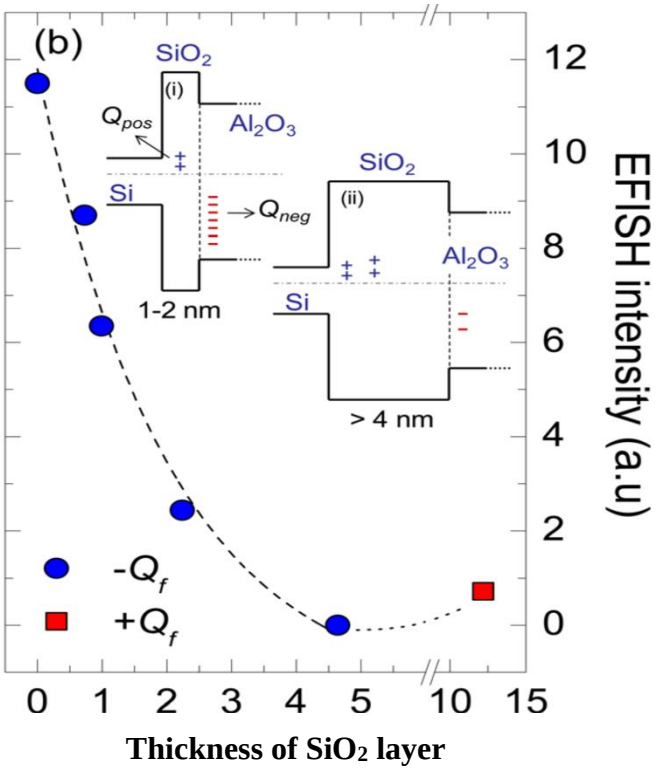

Figure 4.15 Measured EFISH intensity as a function of SiO_2 interlayer thickness.[30]

4.3.2 The effect of the NAOS buffer layer on ALD-Al_2O_3/NAOS/SiC MOS interfaces

NAOS layer shows a good interface defect passivation effect on the Si solar cells. Therefore, we hope to use its features on SiC power devices. However, as we know, 4H-SiC has high chemical stability, compared to Si substrate, SiC is very difficult to oxidize. Figure 4.16 shows the relationship between the NAOS thickness and the oxidation conditions on Si and SiC substrate, to obtain an around 2 nm thickness of the NAOS layer on Si, we only need to carry out the NAOS process at 80 ℃ for 30 min. in contrast, could not obtain any NAOS layer on the SiC at the same oxidation conditions. Thus, we carried out the NAOS process on SiC substrate at 120 ℃ for 120 min to obtain the same thickness of the SiO_2 layer (the SiO_2 layer was confirmed using XPS, as shown in figure 4.17). However, according to previous studies, higher oxidation temperatures cause more impurities, which reduces the quality of the oxide film[28, 31]. Therefore, corresponding to the NAOS layer grown on SiC, post-annealing treatment becomes a critical factor for the ALD-Al_2O_3/NAOS/SiC MOS structure[32].

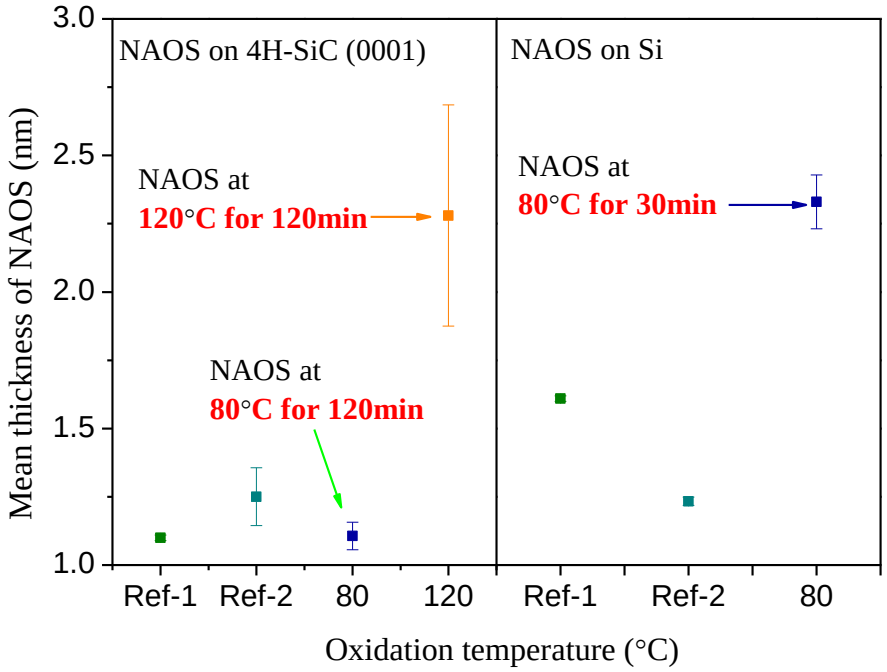

Figure 4.16 Comparison of the oxidation conditions required to obtain the same thickness of NAOS layer on Si and SiC substrates

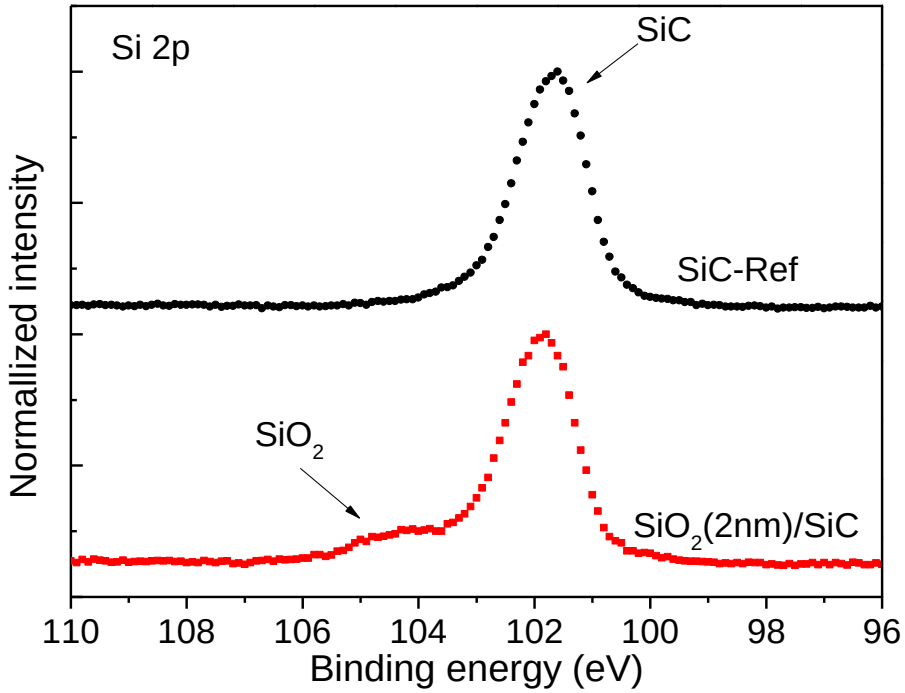

Figure 4.17 XPS spectra taken from the cleaned and nitric acid oxidized 4H-SiC (0001) surface.

4.3.2.1 Strain at the interface of ALD-Al_2O_3/NAOS/SiC

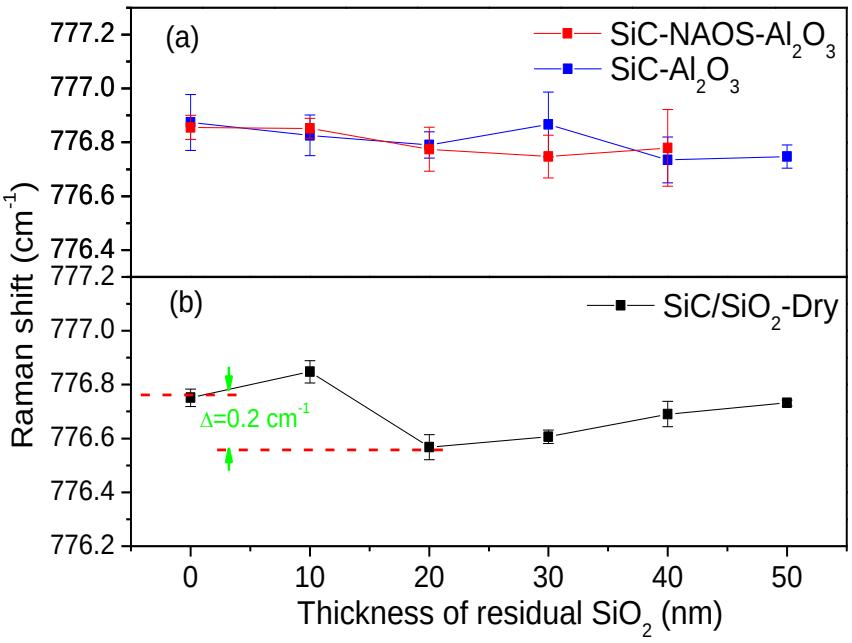

Figure 4.18 Raman peak shift on the surface of a SiC substrate as a function of residual SiO_2 thickness. (a) the oxide layer fabricated by NAOS and ALD, and (b) the oxide layer fabricated by dry thermal oxidation. Raman peak positions were gathered from a 120 min annealed sample with NA = 0.95 objective lenses.

After fabricating the ALD-Al_2O_3/NAOS/SiC structure by growing a 2 nm thickness NAOS layer on the 4H-SiC (0001) surface, and then depositing a 50 nm thickness Al_2O_3 layer on the NAOS layer by ALD. We first evaluated the interface strain using the confocal Raman microscopy system, as we used in chapter 2. The thermal stress σ_T can be defined as

$\Delta\sigma_T = A \cdot \Delta T$, (4.10)

where T is the oxidation temperature, A is a constant composed of Thermal expansion α , Young`s modulus $E_F$, and Poisson`s ratio V_F. Compared with dry thermal oxidation (~1250 ℃), the temperature changes ΔT in the NAOS (~115 ℃) and ALD (~300 ℃) process is much lower. Therefore, the interface stress at the interface of ALD-Al_2O3/NAOS/SiC should be smaller than that of dry thermal oxidation. As we expected, there is no Raman peak shift as shown in the dry oxidation samples at the NAOS/SiC and ALD-Al_2O_3/NAOS/SiC interface can be observed from the figure 4.18, which indicated that the stress of ALD-Al_2O_3/NAOS/SiC interface is too small to be detected using our measurement system.

4.3.2.2 Interface properties w/o NAOS layer

To evaluate the Interface electrical properties, we carried out the C-V measurement on <Al_2O_3/SiC> MOS structure,

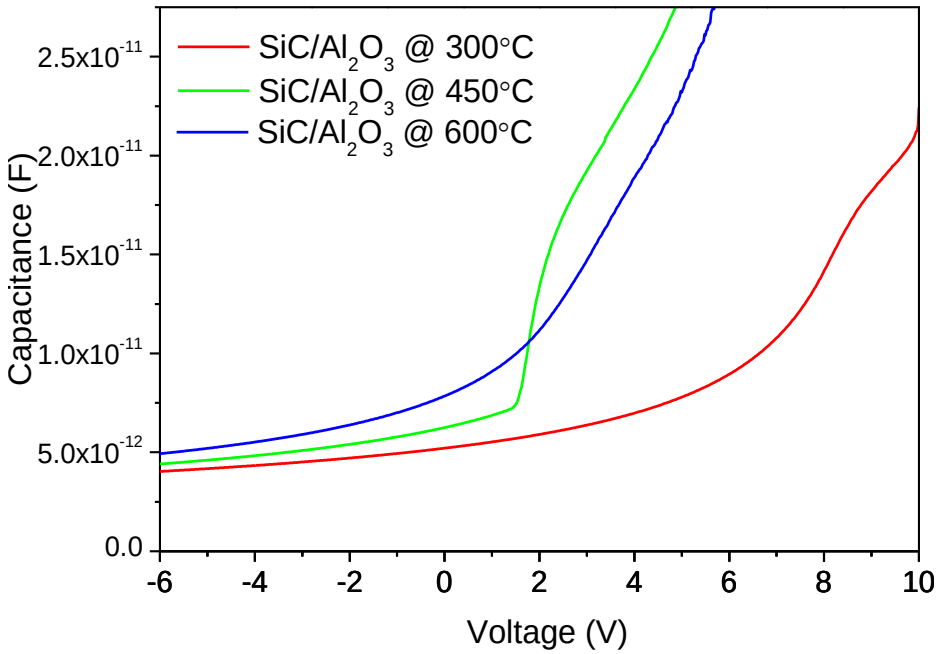

Figure 4.19 C-V curves of the SiC / Al_2O_3 samples with a post annealing at 300, 450, and 600 ℃ for 30 min.

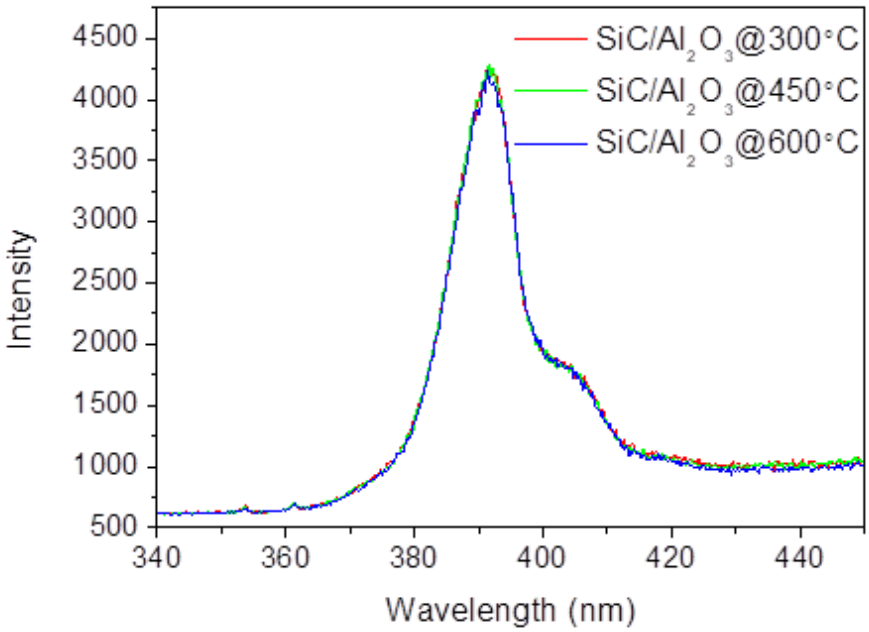

Figure 4.20 PL spectra of SiC/Al_2O_3 structure samples with a post annealing at 300, 450, and 600 ℃ for 30 min.

the samples which were deposited the Al_2O_3 layer on the 4H-SiC (0001) surface directly. The experimental results on the

Si substrate indicated that the field-enhance effect of the ALD layer does not affect the interface characteristics of the Si / NAOS structure. Therefore, we chose n-type SiC as the substrate for the SiC-MOS structure. Thus, the passivation effect of the ALD / NAOS combination layer on the SiC surface in this experiment can be considered to avoid the field-enhance effect of the ALD altogether. Figure 4.19 shows the C-V curves of SiC/Al_2O_3 samples after annealing at different temperatures. We observed that the V_{BF} of all samples moved to the left, which indicates that the deposition of the Al_2O_3 layer caused the accumulation of negative fixed charges at the interface. As mentioned before, the density of surface states is proportional to the surface recombination velocity, which also corresponds to the photoluminescence (PL) intensity. So, we tried to evaluate the interface properties using PL. Figure 4.20 shows the PL spectra of SiC/Al_2O_3 structure annealed at 300, 450, and 600 ℃. Although the different annealing temperatures caused the V_{BF} shift, the annealing process at various temperatures did not affect the PL intensity. This indicated that there is no surface passivation effect from the ALD-Al_2O_3 deposition without a NAOS layer.

4.3.2.3 Interface properties with NAOS layer

We carried out the same experiment on the <Al_2O_3/NAOS/SiC> MOS structure as we did on the <Al_2O_3/SiC> MOS structure. The C-V curves of Al_2O_3/NAOS/SiC samples in which the NAOS layer was annealed at different temperatures. As shown in Figure 4.21, as the annealing temperature increases, the forward V_{fb} shift decreases. Since, as mentioned before, the atomic density of NAOS-SiO_2 increases after POA treatment, which makes the SiO_2 layer treated with POA has a dense structure,[33] thereby suppressing the diffusion of Al. Thus, we can consider that the NAOS layer thickness changes due to the reaction caused by interface diffusion were reduced since we have known that the negative fixed charge density is inverse to the thickness of the SiO_2 layer. This is indicated that a stable NAOS layer was obtained by high-temperature annealing treatment.[34] To evaluate the interface states of the <Al_2O_3/NAOS/SiC> MOS structure, we

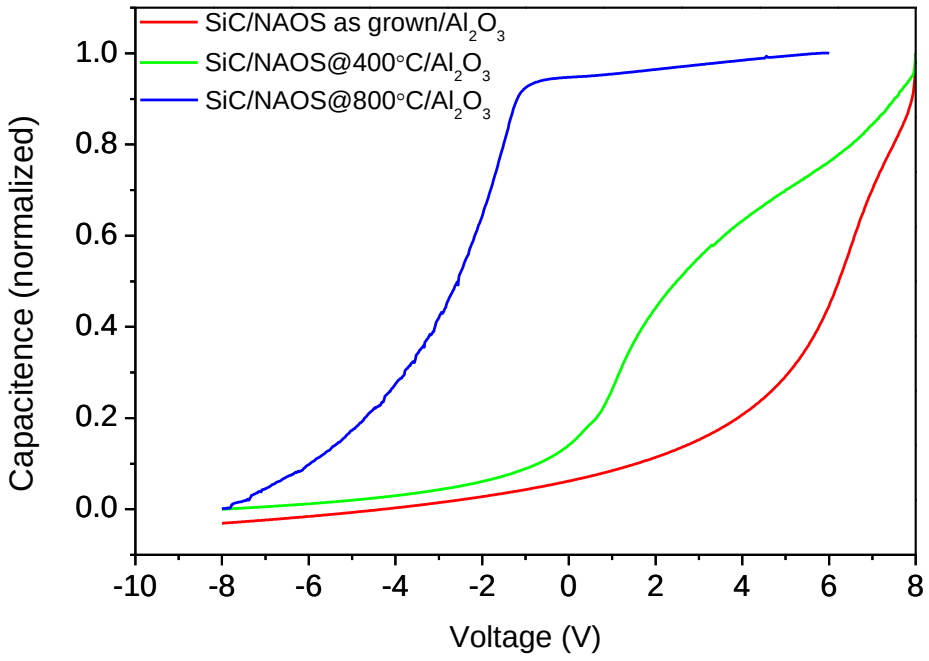

Figure 4.21 C-V curves of SiC/NAOS/Al_2O_3 structure samples, which NAOS layer without annealing and annealing at 400, and 800 ℃ for 2 hours.

carried out the PL measurement on the above samples. We found that the PL intensity of the annealed samples was stronger than that of the samples without annealing treatment of the NAOS layer. The sample POA at 800℃, which corresponding to the most significant V_{fb} shift, shows the most vigorous PL intensity, as shown in Figure 4.22. It indicated that the high-temperature post-annealing treatment improves the quality of the NAOS layer, thereby enhancing this interface passivation effect. Thus, compared to the 400 ° C annealing treatment, the NAOS layer annealed at 800 ℃ has a higher dense structure, resulting in the induction in the interface defect density. As a result, the PL intensity of the 800 °

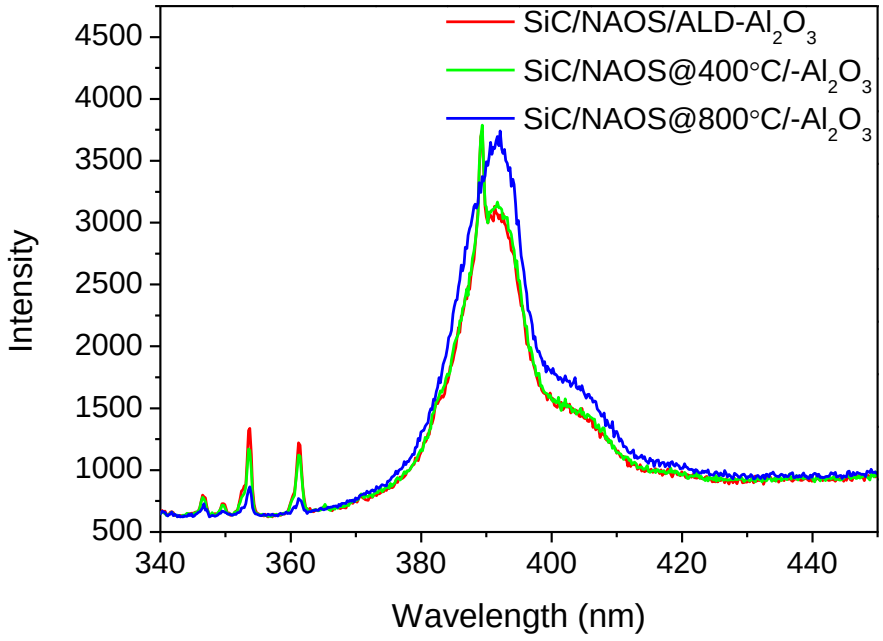

Figure 4.22 PL spectra of SiC/NAOS/Al_2O_3 structure samples, which NAOS layer without annealing and annealing at 400, and 800 ℃ for 2 hours.

C annealing sample is significantly stronger, which indicates that the 800 ° annealing has a better interface passivation effect. It is indicated that the NAOS/ALD-Al_2O_3 combination layer may offer a surface passivation effect on SiC, and the annealing temperature may control this kind of passivation effect. Furthermore, previous research have shown that the addition of the NAOS buffer layer, on the one hand, compared to the sample where the Al_2O_3 layer is deposited directly on the SiC substrate, NAOS relieves the interface stress between SiC and Al_2O_3 due to lattice mismatch[35] and eliminates the generation of an incomplete suboxide layer with low density during the ALD process[36-38], thereby suppressing the generation of interface defects due to the interface stress. On the other hand, due to the vigorous oxidizing activity of the chemical solutions, and the oxidation in HNO_3 makes SiC/SiO_2 interfaces smooth [39]. As a result, the density of defect states at the interface of NAOS/SiC was reduced. Although the addition of the NAOS layer did not show all the advantages mentioned above in this work, we have observed the positive effect of the NAOS layer on surface passivation, and this effect is controllable. Therefore, we can expect that after further improving the theoretical research and the manufacturing process, this low-temperature oxidation method can be used as an effective method to reduce the interface state density of SiC-MOS structures.

In addition, to confirm the effect of the NAOS layer, we carried out the same experiment on the p-type SiC substrate,

however, since the electron excitation of p-type SiC is relatively tricky, as shown in figure 4.23, we could not be able to detect the peak of PL.

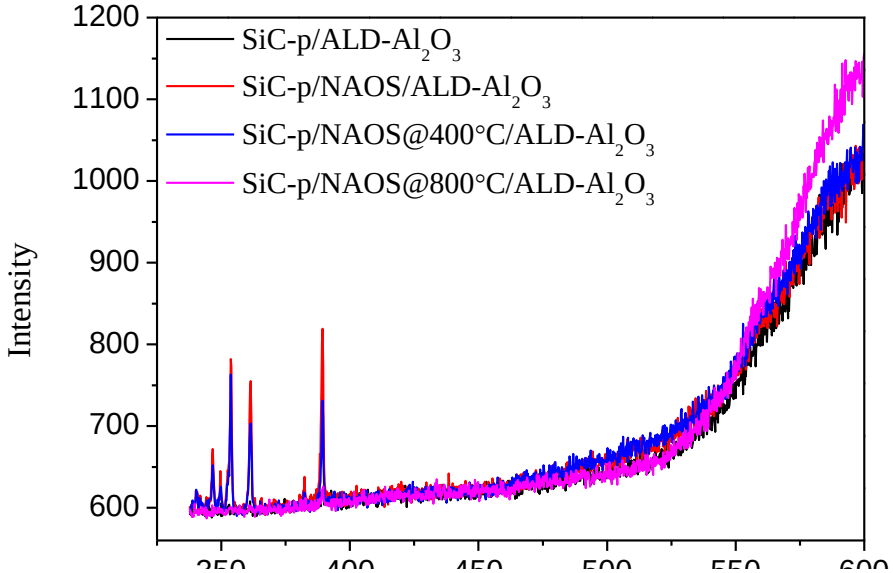

Figure 4.23 PL spectra of p-type SiC/NAOS/Al_2O_3 structure samples, which NAOS layer without annealing and annealing at 400, and 800 ℃ for 2 hours.

4.3.2.4 Compared the interface properties of SiC-MOS fabricated by our low-temperature oxidation and dry thermal oxidation.

The passivation effect of the NAOS / ALD combination is from the NAOS layer. The most significant difference between NAOS-SiO_2 and high-temperature thermal oxidation SiO_2 is the temperature change during the oxidation process, and the temperature change is the direct cause of the interface stress. Therefore, low-temperature oxidation should be able to avoid some defects caused by interfacial stress. We compared the interface properties between low-temperature oxidation samples and the high-temperature oxidation samples based on the PL measurement. As shown in figure 4.24, we observed that the samples fabricated by our low-temperature oxidation method have stronger PL intensity than that of the high-temperature thermal oxidation sample with 120-minute NO annealing treatment, and it is much stronger than the thermal oxidation samples without annealing treatment. In other words, the SiC/SiO_2 structure fabricated by our low-temperature oxidation process has a lower interface state density than the thermal oxidation sample with NO POA. According to the conclusion in Chapter 2, the NO POA cannot completely passivate all the surface defects. Therefore, we can consider that the low-temperature oxidation treatment may eliminate the generation of some defects that NO POA failed to passivate, and these defects are likely to be caused by interfacial stress. This is the reason that the low-temperature oxidation samples show the strongest PL intensity. Thus, we infer that Our low-temperature oxidation method not only avoids the occurrence of interface defects that can be eliminated by NO annealing treatment but also reduces the

generation of interface defects caused by interface stress during the high-temperature oxidation.

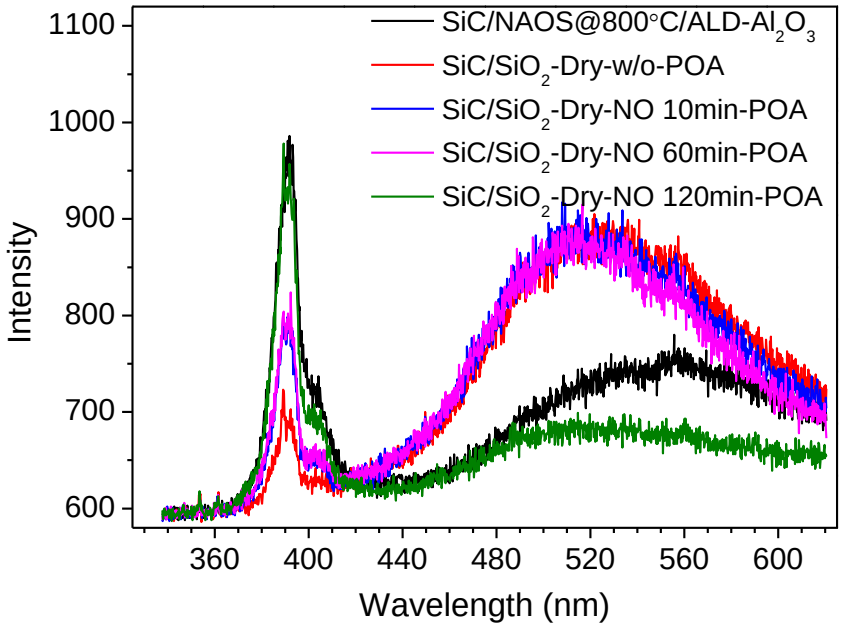

Figure 4.24 Comparison of PL spectra of SiC/oxide structure samples fabricated by our low temperature oxidation method and samples fabricated by high temperature thermal oxidation.

4.4. Summary

In this section, we first studied the structure of the SiO_2 layer grown on the Si substrate by the NAOS method, and then the Al_2O_3 layer was deposited on the NAOS layer by the ALD method, fabricated the Al_2O_3/NAOS/Si structure. The key finding in this part is that an annealing treatment is significant for the NAOS layer to improve its quality to reduce the inter-diffusion in the MOS structure. Then, based on the above findings, we evaluated the effect of the annealing temperature of the NAOS layer on the Al_2O_3/NAOS/SiC MOS interface properties. From the PL intensity data, we found that the treatment of annealing at 800 ° C for 2 hours on the NAOS layer has a significant passivation effect on the SiC surface, which dramatically reduces surface recombination. Moreover, by comparing the samples fabricated by our developed low-temperature oxidation method with traditional high-temperature thermal oxidation samples, the low-temperature oxidation samples show better interface characteristics.

4.5. Reference

[1] T. Kimoto, Material science and device physics in SiC technology for high-voltage power devices, Japanese Journal of Applied Physics, 54 (2015) 040103.

[2] J. Rozen, S. Dhar, S.K. Dixit, V.V. Afanas'ev, F.O. Roberts, H.L. Dang, S. Wang, S.T. Pantelides, J.R. Williams, L.C. Feldman, Increase in oxide hole trap density associated with nitrogen incorporation at the SiO(2)/SiC interface, Journal of Applied Physics, 103 (2008) 124513.

[3] Y. Katsu, T. Hosoi, Y. Nanen, T. Kimoto, T. Shimura, H. Watanabe, Impact of NO annealing on flatband voltage instability due to charge trapping in SiC MOS devices, in: Materials Science Forum, Trans Tech Publ, 2016, pp. 599-602.

[4] T. Matsumoto, H. Nakajima, D. Irishika, T. Nonaka, K. Imamura, H. Kobayashi, Ultrathin SiO2 layer formed by the nitric acid oxidation of Si (NAOS) method to improve the thermal-SiO2/Si interface for crystalline Si solar cells, Applied Surface Science, 395 (2017) 56-60.

[5] V.D. Mihailetchi, Y. Komatsu, L.J. Geerligs, Nitric acid pretreatment for the passivation of boron emitters for n-type base silicon solar cells, Applied Physics Letters, 92 (2008) 063510.

[6] Asuha, S. Imai, M. Takahashi, H. Kobayashi, Nitric acid oxidation of silicon at ∼120°C to form 3.5-nm SiO2/Si structure with good electrical characteristics, Applied Physics Letters, 85 (2004) 3783-3785.

[7] Y.Q. Wu, H.C. Lin, P.D. Ye, G.D. Wilk, Current transport and maximum dielectric strength of atomic-layer-deposited ultrathin Al2O3 on GaAs, Applied Physics Letters, 90 (2007) 072105.

[8] R.Y. Khosa, E.B. Thorsteinsson, M. Winters, N. Rorsman, R. Karhu, J. Hassan, E.O. Sveinbjornsson, Electrical characterization of amorphous Al2O3 dielectric films on n-type 4H-SiC, Aip Advances, 8 (2018) 025304.

[9] C.M. Tanner, Y.-C. Perng, C. Frewin, S.E. Saddow, J.P. Chang, Electrical performance of Al2O3 gate dielectric films deposited by atomic layer deposition on 4H-SiC, Applied Physics Letters, 91 (2007) 203510.

[10] M. Nawaz, On the Evaluation of Gate Dielectrics for 4H-SiC Based Power MOSFETs, Act Passiv Electron, 2015 (2015).

[11] J. Robertson, B. Falabretti, Band offsets of high K gate oxides on III-V semiconductors, Journal of Applied Physics, 100 (2006) 014111.

[12] B. Hoex, S. Heil, E. Langereis, M. Van de Sanden, W.J.A.P.L. Kessels, Ultralow surface recombination of c-Si substrates passivated by plasma-assisted atomic layer deposited Al 2 O 3, 89 (2006) 042112.

[13] S. Imai, M. Fujimoto, Asuha, M. Takahashi, H. Kobayashi, Formation of atomically smooth SiO2/SiC interfaces at ∼120°C by use of nitric acid oxidation method, Surface Science, 600 (2006) 547-550.

[14] Asuha, T. Kobayashi, O. Maida, M. Inoue, M. Takahashi, Y. Todokoro, H. Kobayashi, Ultrathin silicon dioxide layers with a low leakage current density formed by chemical oxidation of Si, Applied Physics Letters, 81 (2002) 3410-3412.

[15] H. Kobayashi, K. Imamura, W.B. Kim, S.S. Im, Asuha, Nitric acid oxidation of Si (NAOS) method for low temperature fabrication of SiO2/Si and SiO2/SiC structures, Applied Surface Science, 256 (2010) 5744-5756.

[16] H. Kobayashi Asuha, O. Maida, M. Takahashi, H. Iwasa, Nitric acid oxidation of Si to form ultrathin silicon dioxide layers with a low leakage current density, Journal of Applied Physics, 94 (2003) 7328-7335.

[17] R.L. Puurunen, A Short History of Atomic Layer Deposition: Tuomo Suntola's Atomic Layer Epitaxy, Chem

Vapor Depos, 20 (2014) 332-344.

[18] A. Pakkala, M. Putkonen, Chapter 8 - Atomic Layer Deposition, in: P.M. Martin (Ed.) Handbook of Deposition Technologies for Films and Coatings (Third Edition), William Andrew Publishing, Boston, 2010, pp. 364-391.

[19] H. Nagel, C. Berge, A.G. Aberle, Generalized analysis of quasi-steady-state and quasi-transient measurements of carrier lifetimes in semiconductors, Journal of Applied Physics, 86 (1999) 6218-6221.

[20] S. Rein, Lifetime spectroscopy: a method of defect characterization in silicon for photovoltaic applications, Springer Science & Business Media, 2006.

[21] W. Shockley, W.J.P.r. Read Jr, Statistics of the recombinations of holes and electrons, 87 (1952) 835.

[22] L.M. Terman, An Investigation of Surface States at a Silicon Silicon Oxide Interface Employing Metal Oxide Silicon Diodes, Solid-State Electronics, 5 (1962) 285-299.

[23] J.R. Brews, An improved high-frequency MOS capacitance formula, Journal of Applied Physics, 45 (1974) 1276-1279.

[24] T. Hatakeyama, Y. Kiuchi, M. Sometani, S. Harada, D. Okamoto, H. Yano, Y. Yonezawa, H. Okumura, Characterization of traps at nitrided SiO2/SiC interfaces near the conduction band edge by using Hall effect measurements, Applied Physics Express, 10 (2017) 046601.

[25] B. Hoex, S.B.S. Heil, E. Langereis, M.C.M. van de Sanden, W.M.M. Kessels, Ultralow surface recombination of c-Si substrates passivated by plasma-assisted atomic layer deposited Al2O3, Applied Physics Letters, 89 (2006) 042112.

[26] A. Abere, S. Glunz, W. Warta, Field effect passivation of high efficiency silicon solar cells, Solar Energy Materials and Solar Cells, 29 (1993) 175-182.

[27] F. Kersten, A. Schmid, S. Bordihn, J.W. Muller, J. Heitmann, Role of annealing conditions on surface passivation properties of ALD Al2O3 films, Proceedings of the 3rd International Conference on Crystalline Silicon Photovoltaics (Siliconpv 2013), 38 (2013) 843-848.

[28] S. Zaima, K. Onoda, Y. Koide, Y. Yasuda, Effects of oxidation conditions on electrical properties of SiC-SiO2interfaces, Journal of Applied Physics, 68 (1990) 6304-6308.

[29] Asuha, T. Yuasa, O. Maida, H. Kobayashi, Effects of postmetallization annealing on ultrathin SiO2 layer properties, Applied Physics Letters, 80 (2002) 4175-4177.

[30] G. Dingemans, N. Terlinden, M. Verheijen, M. Van de Sanden, W.J.J.o.A.P. Kessels, Controlling the fixed charge and passivation properties of Si (100)/Al2O3 interfaces using ultrathin SiO2 interlayers synthesized by atomic layer deposition, 110 (2011) 093715.

[31] T. Sakurai, M. Nishiyama, Y. Nishioka, H. Kobayashi, Low interface state density of SiC-based metal–oxide–semiconductor structure formed with perchloric acid at 203 °C, Applied Physics Letters, 81 (2002) 271-273.

[32] W.K. Choi, T.Y. Ong, L.S. Tan, F.C. Loh, K.L. Tan, Infrared and x-ray photoelectron spectroscopy studies of as-prepared and furnace-annealed radio-frequency sputtered amorphous silicon carbide films, Journal of Applied Physics, 83 (1998) 4968-4973.

[33] G. Dingemans, W.M.M. Kessels, Status and prospects of Al2O3-based surface passivation schemes for silicon solar cells, 30 (2012) 040802.

[34] Asuha, T. Yuasa, O. Maida, H.J.A.P.L. Kobayashi, Effects of postmetallization annealing on ultrathin SiO 2 layer properties, 80 (2002) 4175-4177.

[35] J.B. Kim, D.R. Kwon, K. Chakrabarti, C. Lee, K.Y. Oh, J.H. Lee, Improvement in Al2O3 dielectric behavior by using ozone as an oxidant for the atomic layer deposition technique, Journal of Applied Physics, 92 (2002) 6739-6742.

[36] G.D. Wilk, R.M. Wallace, J.M. Anthony, High-κ gate dielectrics: Current status and materials properties considerations, Journal of Applied Physics, 89 (2001) 5243-5275.

[37] P.M. Tirmali, A.G. Khairnar, B.N. Joshi, A.M. Mahajan, Structural and electrical characteristics of RF-sputtered HfO2 high-k based MOS capacitors, Solid-State Electronics, 62 (2011) 44-47.

[38] V. Naumann, M. Otto, R.B. Wehrspohn, M. Werner, C. Hagendorf, Interface and material characterization of thin ALD-Al2O3 layers on crystalline silicon, Enrgy Proced, 27 (2012) 312-318.

[39] S. Imai, M. Fujimoto, M. Takahashi, H.J.S.s. Kobayashi, Formation of atomically smooth SiO2/SiC interfaces at∼ 120° C by use of nitric acid oxidation method, 600 (2006) 547-550.

Chapter 5 Conclusions

- Main results

The effect of biaxial stress on electronic properties at the 4H-SiC-MOS interface was systematically studied. First, we used a confocal Raman spectroscopic test system to evaluate the stress at the SiO_2 / SiC interface. The residual strain corresponding to Raman peak shifts were found in the HF etched samples with residual SiO_2 layer thicknesses above 10 nm. This suggests that stress exists at the SiO_2/4H-SiC interface. We then used this measuring method to evaluate the effect of NO annealing treatment on the interfacial strain and calculated the stress values based on the measured strains. Since the calculated stresses have similar values (94.12, 51.89, 84.30, and 80.54 MPa) in four types of nitric oxide (NO) treated samples, the result implies that NO post-annealing is not effective in passivation of the defects due to the strain generation at SiO_2/4H-SiC interface.

After quantifying the interface stress of thermally oxidized SiO_2 / SiC interface stress, we used theoretical calculations to analyze the relationship between interface stress and electron mobility. Based on using the deformation potential theory in the phonon scattering model and Boltzmann transport, we calculated the phonon-limited electron mobility in 3D and 2D models under different stresses. We found that when the interface strain <0.5%, the density of states effective mass and conduction mass of in-plane did not significantly change, indicating that the strain-induced effective mass change is too small to affect electron mobility. Based on the strain values obtained in chapter 2, we calculated the strain values. Since the actual value of the strain at the thermal oxidized SiO_2/SiC interface is only around 0.1-0.16% < 0.5%. This may indicate that the generation of deformation potential due to interface stress induced by the thermal oxidation, does not affect the electron mobility at the SiO_2/SiC interface. We have confirmed that the high-temperature thermal oxidation induced interface stress has so little effect on the effective mass that does not affect the electron mobility. Therefore, we have concluded that the interface stress-induced lattice distortion may mainly affect the electron mobility in the formation of the interface defects. To suppress the stress generation of the interface, it is necessary to develop a low-temperature oxidation method for the fabrication of the MOS structures.

We developed the Al_2O_3/NAOS/Si structure fabricated at a low temperature. In the case of the <Al_2O_3/NAOS/Si> MOS structure, the critical finding is that an annealing treatment is essential for the NAOS layer to improve its quality to reduce the inter-diffusion in the MOS structure. Then, based on these findings, we evaluated the effect of the annealing temperature of the NAOS layer on the Al_2O_3/NAOS/SiC MOS interface properties. PL results indicated that our low-temperature oxidation method not only eliminates the occurrence of interface defects that can be eliminated by NO annealing treatment but also reduces the generation of interface defects caused by interface stress during the high-temperature oxidation.

- Future task

One main future task is to evaluate the density of interface traps distribution by extracting the Dit using C-V measurement on <Al2O3/NAOS/SiC> MOS, to confirm the interface properties variation. In addition, to confirm the effect of the NAOS layer, we performed the same experiment on a p-type SiC substrate. However, because the electron excitation of p-type SiC is very difficult, we cannot detect the peak of PL. Therefore, we need to find effective alternative testing methods.

Acknowledgments

I would like to take the opportunity to offer my thanks and gratitude to those people whose help and friendship were valuable beyond measure during my studies.

First of all, I would like to express my most sincere appreciation to my supervisor, Associate Professor Takeaki Sakurai, for his trust in me and for allowing me to pursue my dream. He not only gives me valuable and constructive academic guidance in my research but also provides me with support in all aspects. In the past three years, He has offered me many excellent opportunities to participate in research conferences to communicate with other researchers, and I was fortunate to have the opportunity to conduct joint research with companies. In addition, he gave me great freedom in work and life, which allowed me to focus on my research while taking care of my family. In my mind, he is not only a wise scientist but also a respectable educator. The rigorous work attitude, openness, and tolerance I learned from him will be the wealth of my life forever.

I would also like to thank Prof. Katsuhiro Akimoto. He is so gentle and patient that whenever I encounter difficulties in research and life, he always gives me useful advice and encouragement.

And I would like to thank Associate Professor Hiroshi Yano. He provided me with precious experiment samples and taught me how to fabricate samples and operate C-V measurement in his Lab. Additionally, thanks would be given to Assistant Professor Akiko Ueda. Under her guidance, I performed a theoretical calculation to evaluate the relationship between interface strain and electron mobility. The theoretical calculation is a field I have never encountered before, and I would not be able to complete this study without her patient guidance.

I also thank Dr. Yuji Komatsu from Corporate R&D, Power Electronics (DIJR) ZF Japan Co., Ltd., who gave me experimental suggestions and financial support. Thanks, Chief Researcher Sumiya Masatomo from Wide Bandgap Semiconductors Group of NIMS, who supports my PL measurement.

And I would like to thank all the members of Sakurai & Islam Lab., especially Asst. Prof. MD. Monirul Islam, Asst. Prof. Aboulaye Traore, Dr. Alban, Dr. Alexandre, Imane san, and Mariana san, who gave me help for the experiment. Also, I would like to thank all the members in our lab, and they accompanied me to live a full and exciting life in a diverse laboratory. This is a valuable life experience for me.

Finally, I am most grateful to my parents and wife. Without their so much support and love, I would never be able to arrive where I am today.

Publication list

Fu, W., Kobayashi, A., Yano, H., Ueda, A., Harada, S., & Sakurai, T. (2019). Investigation of stress at SiO_2/4H-SiC interface induced by thermal oxidation by confocal Raman microscopy. Japanese Journal of Applied Physics, 58(SB), SBBD03.

Conference contributions

1. Fu Wei, Ai Kobayashi, Hiroshi Yano, Shinsuke Harada, Takeaki Sakurai. Residual strains at SiO_2/4H-SiC interface measured by Confocal Raman Microscopy. 2018 Joint Symposium on Energy Materials Science and Technology, March 8-9, 2018, Tsukuba, Japan.
2. Fu Wei, Ai Kobayashi, Hiroshi Yano, Shinsuke Harada, Takeaki Sakurai. Stress distribution at SiO_2/4H-SiC interface studied by Confocal Raman Microscopy. The 65th JSAP Spring Meeting, 2018, March 17 – 20, 2018, Nishiwaseda Campus, Waseda University, Tokyo, Japan.
3. Fu Wei, Ai Kobayashi, Hiroshi Yano, Shinsuke Harada, Takeaki Sakurai. Stress at the interface of SiO_2/4H-SiC studied by Confocal Raman Microscopy. 2018 International Conference on Solid Devices and Materials, September 13, 2018, The University of Tokyo, Tokyo, Japan.
4. Fu Wei, Akiko Ueda, Hiroshi Yano, Shinsuke Harada, Takeaki Sakurai. Influence of biaxial stress on the electron transport properties at SiO_2/4H-SiC interfaces. The 66th JSAP Spring Meeting, March 9 – 12, 2019, Ookuyama Campus, Tokyo Institute of Technology, Tokyo, Japan.
5. Fu Wei, Akiko Ueda, Hiroshi Yano, Shinsuke Harada, and Takeaki Sakurai. The effect of biaxial stress on the carrier-transport properties at SiO_2/4H-SiC interfaces. 2019 International Conference on Solid Devices and Materials, September 2-5, 2019, The Nagoya University, Nagoya, Japan.
6. Wei Fu, Xufang Zhang, Hiroshi Umishio, Aboulaye Traore, Hiroshi Yano, Takeaki Sakurai. Effect of annealing temperature on Al_2O_3/NAOS/Si MOS interface properties. The 80th JSAP Autumn Meeting, September 18-21, 2019, Sapporo Campus, Hokkaido University, Sapporo, Japan.
7. Wei Fu, Xufang Zhang, Hiroshi Umishio, Aboulaye Traore, Hiroshi Yano, Takeaki Sakurai. Influence of the annealing temperature on ALD-Al_2O_3/NAOS/Si MOS interface properties. 29th International Photovoltaic Science and Engineering Conference. November 4-8, 2019, Qujiang International Conference Center, Xi`an, Shaanxi, China.